Discrete Material Optimisation of Laminated Composite Structures using EAS and MITC Stabilised 4-Node Shell Element

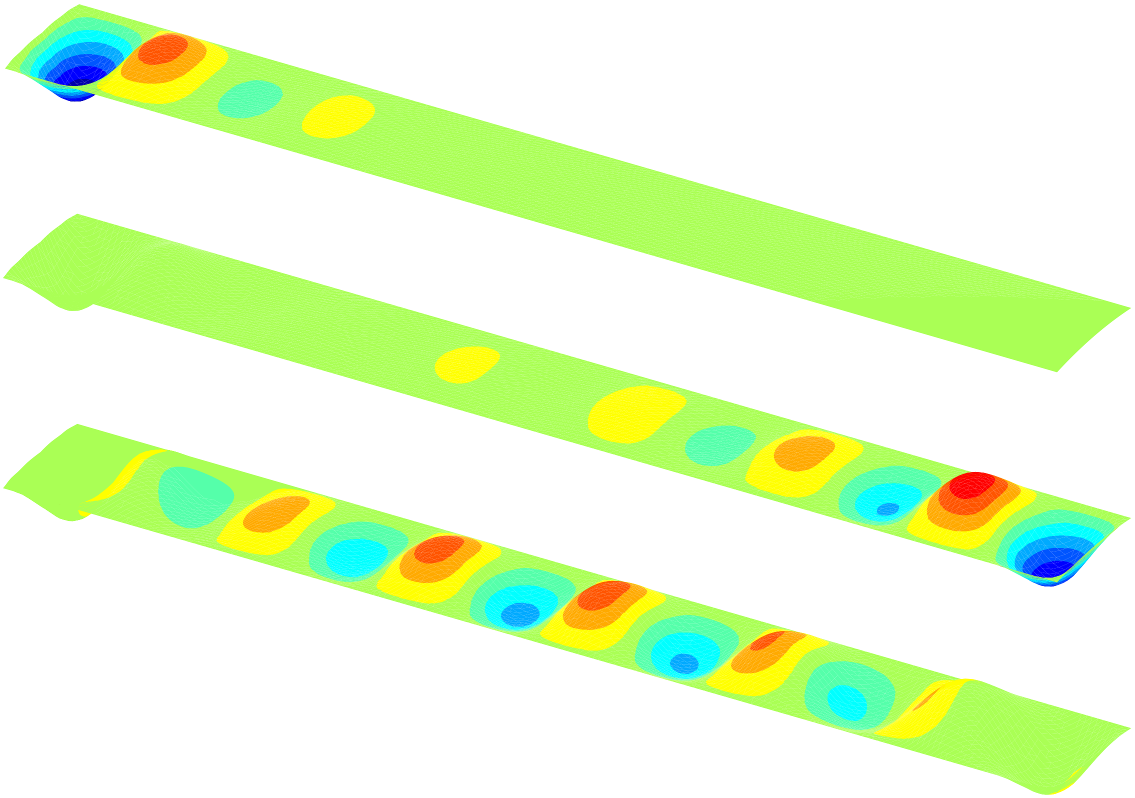

Master's Thesis
Rasmus Kaalund Schøn
Design of Mechanical Systems
Aalborg University
31/05/2022

AALBORG UNIVERSITY
STUDENT REPORT

The Faculty of Engineering and Science
Mechanical and Manufacturing Engineering
Fibigerstræde 16
9220 Aalborg Øst
http://www.mp.aau.dk

Title:

Discrete Material Optimisation of Laminated Composite Structures using EAS and MITC Stabilised Shell Element

Semester:

4^{th} Semester

Semester theme:

Master's Thesis

ECTS:

30

Project period:

02/02/2024 – 31/05/2024

Participants:

Rasmus Kaalund Schøn

Supervisors:

Erik Lund, *Professor, Aalborg University*
Sebastian Malte Hermansen, *Industrial PostDoc, Gurit*

Pages in the report: 62
Total pages: 93
Date of submission: 31/05/2024

Abstract:

Simulation and optimisation methods are crucial in the development process for various industries, such as wind energy and aerospace. Computationally efficient optimisation techniques are crucial to design complex laminated composite structures with the required functionalities, avoiding prototyping, reducing costs, and minimising time to market.

This thesis uses gradient-based optimisation and the Discrete Material Optimisation (DMO) parameterisation to enhance the structural integrity of laminated composite structures. To improve the computational efficiency, analytical sensitivities of a 4-node shell element with Enhanced Assumed Strain (EAS) formulation and Mixed Interpolation of Tensorial Components (MITC) are implemented into the MUltidisciplinary Synthesis Tool (MUST). Analytical sensitivities for buckling load factors are derived and implemented to address buckling-induced failure. Benchmark examples maximise the buckling load factors using the bound formulation and show a significant reduction in computation time compared to a 9-node isoparametric shell formulation.

Given the absence of a universally accepted failure criterion for laminated composites, analytical sensitivity analyses are implemented for the maximum stress, maximum strain, and Tsai-Wu failure criteria. A benchmark example minimises the aggregate function for each of the failure criteria.

Resume

Følgende kandidatafhandling omhandler implementering af gradienter til beregningseffektiv optimering af laminerede kompositstrukturer, som er modelleret med et stabiliseret 4-knuders skalelement.

Laminerede kompositter gør det muligt at designe strukturer til at have specifikke materialeegenskaber i forskellige områder og retninger. Dette kan medføre konkurrencemæssige fordele ved f.eks. at reducerer produktets masse, materialeforbrug eller øge produktets styrke og stivhed. Derfor anvendes laminerede kompositter særligt indenfor fly-, rum- og vindmølleindustrien, hvor masse, styrke og stivhed har stor indflydelse på produktets konkurrencedygtighed på markedet.

I vindmølleindustrien øges længden af vindmøllevingerne, da rotorarealet har en betydelig indflydelse på det elektriske udbytte fra en vindmølle. Dette vanskeliggør design-processen yderligere, da simulereringstiden derved øges og det er derfor særligt attraktivt, at anvende optimeringsmetoder til at designe vindmøllevinger.

Kapitel 2 introducerer elementformuleringen, da den er særligt vigtig for at kunne udlede og implementere analytiske beregninger af gradienter. Der anvendes en række koordinatsystemer til at formulerer elementstivhedsmatricen, der slutteligt transformeres til det globale kartesiske koordinatsystem. Ligeledes defineres de rotationelle frihedsgrader ud fra de respektive knudes director koordinatsystem og transformeres slutteligt til det globale kartesiske koordinatsystem. Elementgeometrien degenereres fra et 8-knuders kontinuumelemet til et 4-knuders skalelement, der mappes til et naturligt kurvelineæret koordinatsystem. Efterfølgende beskrives flytningsfeltet ligeledes i det koordinatsystem. Det er væsentligt at bemærke at en tensor i et kurvelineæret koordinatsystem kan beskrives ved hjælp af de kovariante- og kontravariante komponenter. Derfor præsenteres beregningerne for de kontravariante spændingskomponenter samt kovariante komponenter af det kompatible-og uafhængige tøjningsfelt, som anvendes i elementformuleringen af det stabiliserede 4-knuders skalelement.

Der anvendes i denne afhandling diskret materiale optimering, som er en densitetsbaseret metode, der er særligt anvendeligt til optimering af vindmøllevinger. Denne metode indfører en række lineær bi betingelser, som medfører at sekventiel lineær programmering er særligt god til at løse denne type optimeringsproblemer.

For beregningseffektivt at sikre den strukturelle integritet ved hjælp af gradient baseret optimering implementeres analytiske beregninger af gradienter for lineær bulningsanalyse, maksimum tøjning-, maksimum spænding- og Tsai-Wu brudkriterierne. De strukturelle kriterier kan indføres i optimeringsproblemet som enten objektfunktion eller bi betingelser.

Det lineære bulningsproblem løses iterativt, og det vises under valideringsprocessen af gradienterne, at den absolutte fejl mellem finite difference approksimationerne og de analytiske gradienter kan reduceres drastisk ved at reducere konvergenstolerances. Bound formuleringen anvendes til at maksimere bulningslastfaktorerne af 3 test eksempler. Det demonstreres at beregningstiden reduceres betydeligt ved at anvende et stabiliseret 4-knuders skalelement i stedet for et 9 knuders isoparametrisk skalelement. Yderligere vises det at beregningstiden af gradienterne for lineær bulnings objekt funktion er meget sammenlignelige med en tilsvarende model der anvender et stabiliseret 8-knuders solid-skalelement.

Brudkriterierne anvender et statisk brudindeks, der konverteres til et globalt kriterie med en P-norm aggregatfunktion. Det statisk brudindeks penaliseres ved hjælp af vægtfunktioner for, at gøre det uattraktivt at have densiteter som ikke er 0 eller 1. Der anvendes ved maksimum spænding og Tsai-Wu brudkriterierne yderligere en lineær vægtfunktion på spændingerne, hvor det også er muligt tilføje penalisering. Det demonstreres at brudkriterierne kan anvendes til at optimere laminerede kompositter mod statisk brud.

Contents

Preface

This master's thesis is the result of Rasmus Kaalund Schøn's work during the 4th semester at the MSc. programme Design of Mechanical Systems at the Faculty of Engineering and Science, Aalborg University. The author would like to extend his gratitude to Professor Erik Lund, AAU and industrial PostDoc Sebastian Malte Hermansen, Gurit, for their valuable guidance during the preparation of this thesis.

Formalities

This thesis uses the Harvard method for referencing the literature. Section references are indicated by (Last name, year), while in-text references are indicated by Last name (Year). A bibliography at the end of this thesis lists all references used.

Figures, tables and equations are numbered according to their respective chapters, where 'Figure 1.3' refers to the third figure in Chapter One.

Furthermore, a nomenclature consists of abbreviations, symbols, and mathematical notations. To differentiate between the same symbol, then subscripts and superscripts are used. A parenthesis is added to superscript(s) to distinguish between exponents and superscript notation. For the best reading experience, printing the thesis in a double-sided A4 format with colour is recommended.

Signature: Rasmus Kaalund Schøn

Nomenclature

Abbreviations

ANS	Assumed Natural Strain
BLAS	Basic Linear Algebra Subprograms
CLPT	Classic Laminated Plate Theory
DMDTO	Discrete Material and Direct Thickness Optimisation
DMO	Discrete Material Optimisation
DMTO	Discrete Material and Thickness Optimisation
DoF	Degree of Freedom
DSS	Direct Sparse Solver
EAS	Enhanced Assumed Strain
ESL	Equivalent Single Layer
etc.	et cetera
FSDT	First order Shear Deformation Theory
i.e.	id est
LCOE	Levelized Cost of Energy
MITC	Mixed Interpolation of Tensorial Components
MMA	Moving Methods of Asymptotes
MUST	MUltidisciplinary Synthesis Tool
NCF	Non-Crimp Fabric
RAMP	Rational Approximation of Material Properties
SIMP	Solid Isotropic Material and Penalisation
SLP	Sequential Linear Programming
SNOPT	Sparse Nonlinear OPTimizer

SQP	Sequential Quadratic Programming
TSDT	Third order Shear Deformation Theory
w.r.t.	With respect to

Notation

[ ]	Matrix
$\ddot{u}$	Second time derivative of a variable u
$\frac{\partial f(x)}{\partial x}$	Partial derivative of a function w.r.t a variable
$\frac{df(x)}{dx}$	Full or total derivative of a function w.r.t a variable
Symbol$^{()}$	Superscript notation for extra index
{ }	Vector

Symbols and Letters

$F_1, F_2, F_{11}, F_{12}, F_{22}, F_{66}$	Tsai-Wu Strength values	[N/m^2]
α_a, β_a, μ_a	Rotational DoF's of node a	[Rad]
β	Bound in the bound formulation	
κ	Structural objective function	
λ	Buckling load factor	[-]
$[\mathbf{C}]$	Constitutive matrix	[N/m^2]
$[\mathbf{N}]$	Shape function matrix	[-]
$[\mathbf{T}]$	Transformation matrix	[-]
$[\mathbf{E}_\pm]$	Extrapolation matrix	[-]
$[\mathbf{L_e}]$	Bookkeeping matrix	[-]
$\left[\tilde{\mathbf{M}}\right]$	Covariant independent strain interpolation matrix in the Gauss points	[-]
$[\mathbf{B_L}]$,$[\mathbf{B_0}]$,$[\mathbf{B}]$	Nonlinear, linear and total strain displacement matrix	[-]
$[\mathbf{K}_{\boldsymbol{\sigma}}]$,$[\mathbf{K_T}]$,$[\mathbf{K_0}]$	Global stress stiffening, tangent and linear stiffness matrix	[N/m^2]
$[\mathbf{k}_{\boldsymbol{\sigma}}]$,$[\mathbf{k_T}]$,$[\mathbf{k_0}]$	Element stress stiffening, tangent and linear stiffness matrix	[N/m^2]
$[\mathbf{k_{uu}}]$,$[\mathbf{k}_{\boldsymbol{\alpha\alpha}}]$,$[\mathbf{k}_{\mathbf{u}\boldsymbol{\alpha}}]$,$[\mathbf{k}_{\boldsymbol{\alpha}\mathbf{u}}]$	Sub-matrices for element stiffness matrix	[N/m^2]
$[\mathbf{M}]$	Original independent strain interpolation matrix	[-]
$[\mathbf{S}]$	2$^{\text{nd}}$ Piola-Kirchhoff stress tensor	[N/m^2]
ν	Poisson's ratio	[-]

Π	Total elastic potential	[J]
ψ	Merit function	
ρ	Density	[kg/m^3]
θ	Angle	[Rad] or [°]
$\tilde{f}_{pm}$	Augmented Lagrangian P-norm aggregate function	
$\{\mathbf{\Lambda}\}$	Vector of Lagrangian multipliers	[-]
$\{\mathbf{1}\},\{\mathbf{2}\},\{\mathbf{3}\}$	Material coordinate system	[-]
$\{\boldsymbol{\alpha}\}$	Internal DoF	[m]
$\{\hat{\mathbf{e_1}}\},\{\hat{\mathbf{e_2}}\},\{\hat{\mathbf{e_3}}\}$	Cartesian basis vectors	[-]
$\{\mathbf{\Phi}\}$	Buckling mode shape vector	[m]
$\{\boldsymbol{\sigma}\}$	Stress	$[N/m^2]$
$\{\boldsymbol{\varepsilon}\}$	Strain	[-]
$\{\mathbf{d_1}\},\{\mathbf{d_2}\},\{\mathbf{d_3}\}$	Element coordinate system basis vector	[-]
$\{\mathbf{D}\}$	Global nodal displacement vector	[m]
$\{\mathbf{d}\}$	Element nodal displacement vector	[m]
$\{\mathbf{F_{ext}}\}$	Global external load vector	[N]
$\{\mathbf{f_{ext}}\}$,$\{\mathbf{f_{int}}\}$,$\{\mathbf{f_{eas}}\}$	External-, internal-and EAS load vector	[N]
$\{\mathbf{g^1}\},\{\mathbf{g^2}\},\{\mathbf{g^3}\}$	Contravariant basis vectors	[-]
$\{\mathbf{g_1}\},\{\mathbf{g_2}\},\{\mathbf{g_3}\}$	Covariant basis vectors	[-]
$\{\mathbf{R}\}$	Global residual vector	[N]
$\{\mathbf{r}\}$	Element residual vector	[N]
$\{\mathbf{u}\}$	Displacement vector	[m]
$\{\mathbf{V_1}\}$,$\{\mathbf{V_2}\}$,$\{\mathbf{V_3}\}$,$\{\mathbf{v_1}\}$,$\{\mathbf{v_2}\}$,$\{\mathbf{v_3}\}$	Node directors	[-]
$\{\mathbf{X}\}$	Position vector before deformation	[m]
$\{\mathbf{x}\}$,$\{\mathbf{x}\}$	Position vector after deformation and design variable vector	[m],[-]
ξ,η,ζ	Natural coordinate system	[-]
B_i	Volume forces	[N]
E,G	Modulus of elasticity and shear modulus	[N/m^2]
e_{12}, e_{13}, e_{23}	Shear failure strain in principal material coordinates	[-]

e_{1c}, e_{1t}	Failure strain in compression and tension in the material 1-direction	[-]
e_{2c}, e_{2t}	Failure strain in compression and tension in the material 2-direction	[-]
E_{ij}	Covariant Green-Lagrange strain tensor	[-]
f_{pm}	P-norm aggregate function	
h_l,h_{Lam}	Lamina and laminate height	[m]
M_{cnd}	Measure of candidate non-discreteness	[%]
N_c	Number of candidate materials	[-]
N_{EV}	Number of eigen vectors	[-]
N_e	Number of elements	[-]
N_{layer}	Number of layers	[-]
P	P-norm factor	[-]
p, q, c	Penalisation factors	[-]
r, s, t	Natural coordinate system	[-]
S^{ij}	Contravariant 2nd Piola-Kirchhoff stress tensor	[N/m^2]
S_{12},S_{13},S_{23}	Failure shear strain in principal material coordinates	$[N/m^2]$
T_i	Traction forces	[N]
V	Volume	[m^3]
$w()$	Weight functions	[-]
$w_\sigma()$	Stress field weight function	[-]
$w_c()$	Candidate weight function	[-]
$w_{FI}()$	Failure index weight function	[-]
x, y, z	Global coordinate system	[-]
X_t,X_c	Failure stress in compression and tension in the material 1-direction	$[N/m^2]$
x_{elc}	Design variable for element e in layer l for candidate c	[-]
x_{plc}	Design variable for patch p in layer l for candidate c	[-]
Y_t, Y_c	Failure stress in compression and tension in the material 2-direction	$[N/m^2]$
y_k	Slack variables	

1 Introduction

Simulation and optimisation methods have become an increasingly important strategic priority in several industries' product development, aiming to obtain faster time to market, reduced cost, zero prototyping, and improved performance.

Simulation-driven design and structural optimisation methods are crucial in developing wind turbine blades due to the large and complex structure comprising fibre-reinforced composite materials, core materials, varying thicknesses and curved surfaces. Fibre-reinforced composites offer the opportunity to tailor mechanical properties to achieve functionalities that cannot be obtained through traditional isotropic materials. Designing such a complex structure based on engineering intuition alone is challenging, and each design proposal must undergo computationally expensive simulations. Therefore, optimisation techniques are crucial to synthesise wind turbine blades with the required functionalities. Engineers can use simulation and optimisation to enhance aerodynamic performance, structural integrity, overall efficiency and costs.

However, computational limitations restrict the exploration of the entire design space. The challenge is observed in various industries, as highlighted in "Unveiling the next frontier of engineering simulation", published by McKinsey & Company (Ragani et al., 2023), which recognises efficiency as an important value driver for simulation tools.

The primary focus of this thesis is the specific challenges associated with the structural optimisation of wind turbine blades. This is particularly important due to the significant impact of wind turbine blade performance on the wind turbine's levelized cost of energy (LCOE). The wind turbine blades are responsible for converting kinetic energy into electrical energy and represent the most costly component of the turbine (Mishnaevsky et al., 2017). Structural optimisation of wind turbine blades may involve many design variables. In this thesis, the decision is not to reduce the number of design variables to make heuristic zero-order methods feasible. Therefore, this thesis is limited to gradient-based optimisation methods.

1.1 Objective

The master's thesis builds upon the 15 ECTS project by Schøn (2023). Here, analytical Design Sensitivity Analyses (DSA) were demonstrated for stress-based Discrete Material Optimisation (DMO) using a stabilised 4-node shell element on a simple plate model.

It has been demonstrated that this shell element is more computationally efficient than the 9-node isoparametric shell element. Therefore, efficient DSA for the 4-node shell element must be implemented into the MUltidisciplinary Synthesis Tool (MUST) to utilise the increased computational efficiency for gradient-based optimisation. The finite element-based research code is written in Fortran 90. It is a multi-physics and optimisation tool that has been continuously developed at Aalborg University's Department of Materials and Production since 1999. It enables users to specify different parameterisations, elements, boundary conditions, material models, and failure modes, among other choices to analyse and optimise structures.

This master's thesis aims to implement computationally efficient DSA and demonstrate the usage for optimisation of laminated composite structures using the stabilised 4-node shell element. By integrating efficient DSA for the stabilised 4-node shell element into MUST, engineers and researchers can optimise the design of wind turbine blades and other laminated composite structures more quickly, thereby reducing the time to market. Alternatively, they can increase the model's resolution, providing a level of detail and insight into previously unattainable problems with a coarser mesh. This can lead to advancements in synthesising wind turbine blades and other laminated composite structures, addressing common computational limitations.

1.2 Problem statement

How can the stabilised 4-node shell element be used to perform structural optimisation of laminated composite structures ?

Thesis outline

The structure of the thesis is outlined below:

- **Chapter 2) Modelling of Fibre-Reinforced Laminated Composites**
  This chapter serves as a foundation for the thesis. It presents an overview of various methods, highlighting their advantages and disadvantages. It also provides a comprehensive review of the stabilised 4-node shell element to help readers understand the important equations underlying the theory. This understanding is essential for deriving analytical and computationally efficient DSA.
- **Chapter 3) Discrete Material Optimisation of Laminated Composites**
  It introduces gradient-based optimisation methods and the DMO parameterisation.
- **Chapter 4) Linear Buckling Optimisation**
  The linear buckling analysis is formulated, and analytical sensitivities are derived and validated. Three benchmark examples are optimised, and the computational performance is compared to a 9-node isoparametric shell element and a stabilised 8-node solid shell formulation.
- **Chapter 5) Static Failure Optimisation**
  This chapter presents the derivation and validation of analytical sensitivities for one static failure criterion, while two other criteria are derived and validated in Appendix D and E. Additionally, a benchmark example demonstrates the optimisation of a laminated composite structure for each failure criterion.
- **Chapter 6) Conclusion**
  Presents the conclusions of the thesis and **Chapter 7)** identifies areas for further

research on structural optimisation of laminated composite structures using the stabilised 4-node shell element.

2 Modelling of Fibre-Reinforced Laminated Composites

The high stiffness- and strength-to-weight ratios of fibre-reinforced laminated composites make them well-suited for various structural applications where light weight is an essential value driver. Multiple laminae make these composites, each consisting of layers of fibres embedded in a matrix material, as illustrated in Figure 2.1.

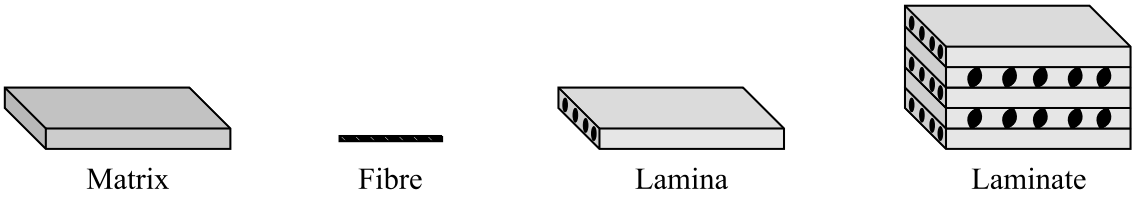

Figure 2.1. Definitions using a macroscopic perspective of fibre-reinforced laminated composites.

When integrated into a laminate, the orthotropic lamina exhibits anisotropic behaviour due to the coupling between various types of deformation, such as shear extension, bending extension, and bend twist. Designers can tailor these coupling terms to obtain the mechanical, thermal and acoustic properties on a macro scale by selecting fibre orientation, lamina thickness, stacking sequence, fibre architecture, fibre and matrix materials. However, accurately modelling the behaviour of these laminated composites presents some challenges. Therefore, various methods have been proposed to analyse fibre-reinforced laminated composite structures. (Jones, 1998)

The focus of the thesis lies in the optimisation of general laminated composite structures. As a result, the focus is placed on the Equivalent Single Layer (ESL) theories.

2.1 Equivalent Single Layer Theories

Shell elements are widely utilised in modern engineering simulations to model fibre-reinforced laminated composites, as they have proven to be an accurate and computationally efficient formulation to capture the complex mechanical behaviour of these materials. Specifically, mechanical behaviour exhibits characteristics similar to those described by ESL theories. Therefore, it is essential to have a comprehensive understanding of the mechanical behaviour described by the ESL theories to understand the limitations of shell elements.

The deformation obtained in ESL theories shown in Figure 2.2 is based on plate theories, which include Kirchhoff-Love plate theory, Reissner-Mindlin plate theory, and third-order plate theory. These theories exhibit several similarities to beam theories, as they are generalisations of Euler-Bernoulli's beam theory, Timoshenko beam theory, and third-order beam theory.

In the following subsections, an introduction to each theory is provided but will be limited to the linear version of the theory. (Lund, 2022)

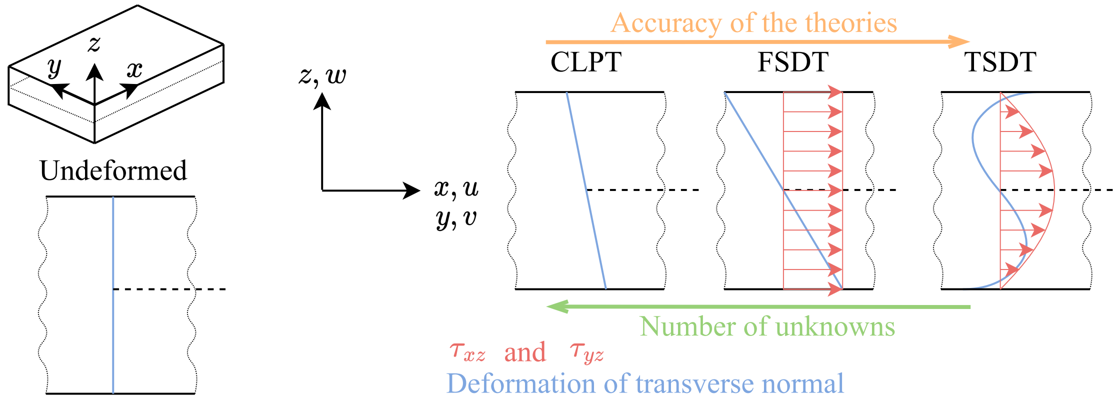

Figure 2.2. Deformation of the transverse normal and transverse shear strain distribution in different ESL-theories. The mid surface is marked with dashed lines

2.1.1 Classic Laminated Plate Theory

Classic Laminated Plate Theory (CLPT) is based on the Kirchhoff-Love plate theory, which is derived from the assumption that the transverse normals on the mid surface of the plate remain straight after deformation and are in-extensible. Due to the in-extensible normals, there is no transverse normal strain, using the notation shown in Figure 2.2, $\varepsilon_{zz} = 0$. Furthermore, transverse normals are assumed to remain perpendicular to the midsurface after deformation. Therefore, there is no transverse shear strain $\gamma_{xz} = \gamma_{yz} = 0$, and the deformation of the transverse normals is solely influenced by bending and in-plane normal strain. It is important to note that the CLPT has a significant drawback. It fails to satisfy laminate equilibrium because it cannot model transverse normal strain and transverse shear strain. These strain components are crucial in predicting failure due to delamination, as they produce interlaminar stresses to establish equilibrium. Interlaminar stresses cause delamination. CLPT is rarely used in the finite element method since it requires C^1 continuity. (Lund, 2022)

2.1.2 First order Shear Deformation Theory

The natural modification to CLPT is the first-order Shear Deformation Theory (FSDT). This theory is based on the Reissner-Mindlin plate theory and allows the rotation of transverse normals. When the transverse normals undergo rotation, it leads to constant transverse shear strain along the laminate thickness. Medwadowski (1958) extended the work to orthotropic plates before Whitney (1969) and Whitney and Pagano (1970) formulated the theory for laminated plates.

The FSDT provides a more accurate representation of the parabolic distribution, which is predicted for isotropic plates by the linear theory of elasticity and Third-order Shear Deformation Theory (TSDT). In FSDT, the equilibrium equations are not satisfied at the lamina interfaces due to the inaccurate shear strain distribution. This inaccurate shear strain distribution further requires a correction factor called the shear correction factor to ensure the shear strain energy is equivalent to what is obtained from the analytical solution. The shear correction factor is difficult to determine accurately. Therefore, the shear correction factor of an isotropic plate is often used as an approximation. The transverse normals exhibit similarities to CLPT, which is assumed to remain straight after deformation and inextensible. As a result, FSDT can not predict transverse normal strain.

Shell elements based on FSDT are widely used in the finite element method despite being prone to in-plane and transverse shear locking. Several techniques have been developed to address these locking issues, and section 2.2 will expand upon this topic. (Lund, 2022)

2.1.3 Third order Shear Deformation Theory

To obtain a more accurate theory, eliminate the need for a shear correction factor and eliminate shear locking, higher-order deformation theories were developed by Levinson (1980) and Murthy (1981). Later, Reddy (1984) made significant improvements to the initial theories, resulting in a higher-order deformation theory for linear orthotropic plates that accurately accounts for shear deformation. Additionally, Reddy (1986) refined the theory for laminated plates, making it a valuable tool for analysing and designing laminated composite structures. These advancements were obtained by representing the deformation of the transverse normal as a cubic function through the thickness to obtain the parabolic shear strain distribution.

The disadvantages of TSDT are the computational cost of extra unknowns and the equilibrium. When different layers are used, the shear correction factor is still needed. Similar to CLPT and FSDT, equilibrium at the laminae interface is not satisfied due to the discontinuous stress distribution through the thickness. Despite the potential benefits of achieving equilibrium at surfaces, more accurate shear stress distribution and mitigating shear locking, the associated computational expense often outweighs these advantages. (Lund, 2022)

2.2 Stabilised 4-Node Shell Element

This section presents the stabilised 4-node shell element derived and implemented into MUST by Stagsted and Bertelsen (2023).

In the finite element method, the numerical model can be obtained by studying variations denoted δ on an arbitrary mechanical system described by a functional to obtain the equilibrium configuration of the system. In contrast to the method proposed by Reissner, where variations on displacements u_i, strains ε_{ij} and stresses σ_{ij} on the Reissner functional are studied. The formulation is based on the Rayleigh-Ritz method, where these variations are studied on the total elastic potential Π in Eq. (2.1). The variables $T_i^{(n)}$ represent the traction forces, while B_i refers to the volume forces.

$$\Pi = \int_V \sigma_{ij}\varepsilon_{ij}\, dV - \int_V B_i u_i\, dV - \int_{S_1} T_i^{(n)} u_i\, dS - \int_V u_i \rho \ddot{u}_i\, dV \tag{2.1}$$

The objective of the current section is to obtain a discretised version of Eq. (2.1) because a stationary point of an arbitrary mechanical system can be obtained by finding the solution to $\delta\Pi = 0$.(Dym and Shames, 2013) Particular attention is paid to addressing the challenges associated with modelling fibre-reinforced laminated composites, and the formulation is restricted to considering static problems. Therefore, the inertia forces $\int_V u_i \rho \ddot{u}_i\, dV = 0$.

Frequently, the element formulation is carried out solely in Cartesian coordinate systems, as can be exemplified by the isoparametric shell element where the geometry is mapped to a natural coordinate system in Cartesian coordinates (ξ, η, ζ) as shown inFigure 2.3. However, when formulating the four node-stabilised shell elements, Cartesian and Curvilinear coordinates are utilised, requiring some particular attention. The displacements, strain and stresses are formulated in natural coordinates expressed using Curvilinear coordinate system (r, s, t) as illustrated in Figure 2.4. In (ξ, η, ζ) and (r, s, t) systems, the geometry is mapped into a coordinate system where the geometry can obtain values from -1 to 1.

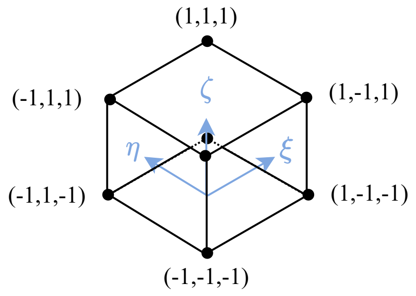

Mapping of isoparametric shell

Figure 2.3. Natural coordinates (ξ, η, ζ) when mapping isoparametric element types

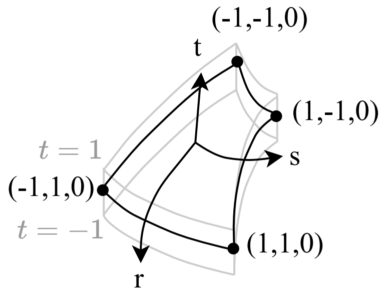

Mapping of 4-node shell

Figure 2.4. Natural coordinates (r, s, t) expressed in Curvilinear coordinates

According to the theory of elasticity, the constitutive properties are represented by a fourth-order tensor, whereas the stresses and strains are second-order tensors. Using curvilinear coordinates introduces certain complications due to a curvilinear coordinate system being a non-orthogonal coordinate system. This is illustrated for a first-order tensor, also a vector in Figure 2.5. Since the coordinate system is non-orthogonal, the perpendicular and parallel components of $\{\mathbf{A}\}$ do not coincide. Therefore $\{\mathbf{A}\}$ can be expressed using either covariant components A_1 and A_2, or contravariant components A^1 and A^2 as shown in Eq. (2.2).

$$\{\mathbf{A}\} = A^j\{\mathbf{g}_j\} = A_j\{\mathbf{g}^j\} \tag{2.2}$$

Subscripts are used according to a well-established convention in tensor analysis, where they indicate covariant representation, and superscripts indicate contravariant representation. Similar expressions as Eq. (2.2) can be obtained for second- and fourth-order tensors as described in Nielsen (2018).

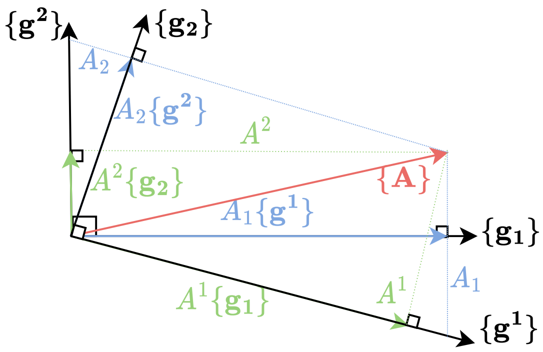

Figure 2.5. Contravariant and covariant projections of an arbitrary first-order tensor $\{\mathbf{A}\}$

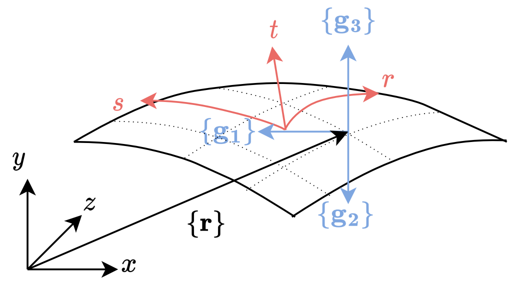

Figure 2.6. Covariant base vectors can be established from an arbitrary position vector $\{\mathbf{r}\}$

The covariant and contravariant base vectors $\{\mathbf{g}_j\}$ and $\{\mathbf{g}^j\}$, respectively, can be established from the geometry of a shell, as illustrated in Figure 2.6. As proposed by Vu-Quoc and Tan (2003), the covariant base vectors are obtained as the tangent vectors of the shell in the r, s, t-system, from a position vector $\{\mathbf{r}\}$ as shown in Eq. (2.3).

$$\{\mathbf{g}_j\} = \frac{\partial\{\mathbf{r}\}}{\partial x_j} \qquad x_j = r, s, t \qquad j = 1, 2, 3 \tag{2.3}$$

The contravariant base vectors can then be obtained as the inverse of the covariant base vectors.

2.2.1 Coordinate systems

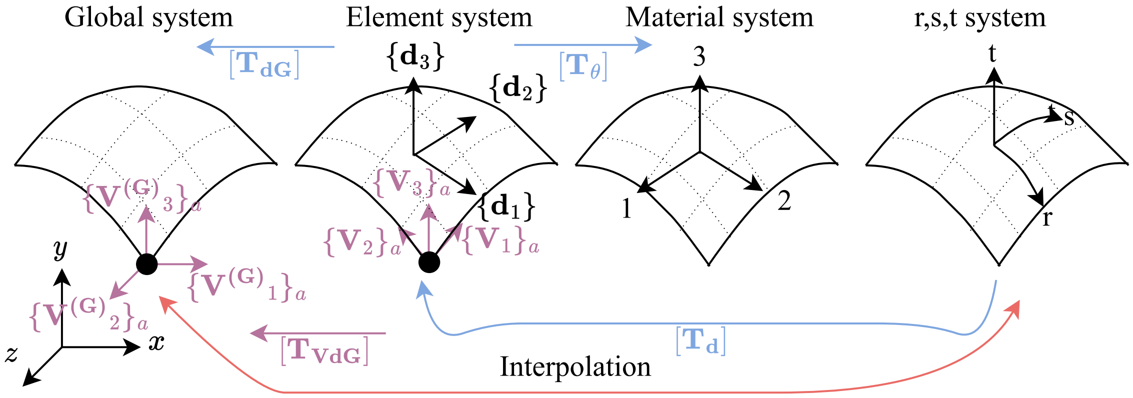

Figure 2.7. Overview of some coordinate systems used to formulate the stabilised 4-node shell element. All coordinate systems in the illustration are Cartesian coordinates except the r, s, t-system, which is Curvilinear. It should be noted that the covariant and contravariant coordinate systems have not been included in the illustration

The formulation of the stabilised 4-node element requires specific quantities to be defined in one or more coordinate systems in Figure 2.7. To differentiate between the various coordinate systems and the locations where the displacements, strain and stress are defined, the following notations are used:

- Global coordinate system $\{\mathbf{e}_1\}, \{\mathbf{e}_2\}, \{\mathbf{e}_3\}$ or x, y, z, notation G or capital letter
- Element coordinate system $\{\mathbf{d}_1\}, \{\mathbf{d}_2\}, \{\mathbf{d}_3\}$, notation d or lower case letters
- Material coordinate system $1, 2, 3$, notation 12
- Covariant coordinate system $\{\mathbf{g}_1\}, \{\mathbf{g}_2\}, \{\mathbf{g}_3\}$, notation Cov or subscripts
- Contravariant coordinate system $\{\mathbf{g}^1\}, \{\mathbf{g}^2\}, \{\mathbf{g}^3\}$, notation Con or superscripts
- Natural coordinate system r, s, t
- Director coordinate system of node a in the element coordinate system $\{\mathbf{V}_1\}_a, \{\mathbf{V}_2\}_a, \{\mathbf{V}_3\}_a$
- Director coordinate system of node a in the global coordinate system $\{\mathbf{V^{(G)}}_1\}_a, \{\mathbf{V^{(G)}}_2\}_a, \{\mathbf{V^{(G)}}_3\}_a$

The notations introduced are used in the report as either subscripts or superscripts to indicate where the quantities are defined.

Global coordinate system

To facilitate a streamlined modelling process, the geometry of the structure and boundary conditions are defined in the global coordinate system. This is preferred as defining the problem in global coordinates is more intuitive. As a result, it is crucial to accurately map the geometry and boundary conditions onto the natural coordinate system as elaborated in subsection 2.2.2. It is in the global coordinate system that the solution to the global equilibrium equation is obtained.

Material coordinate system

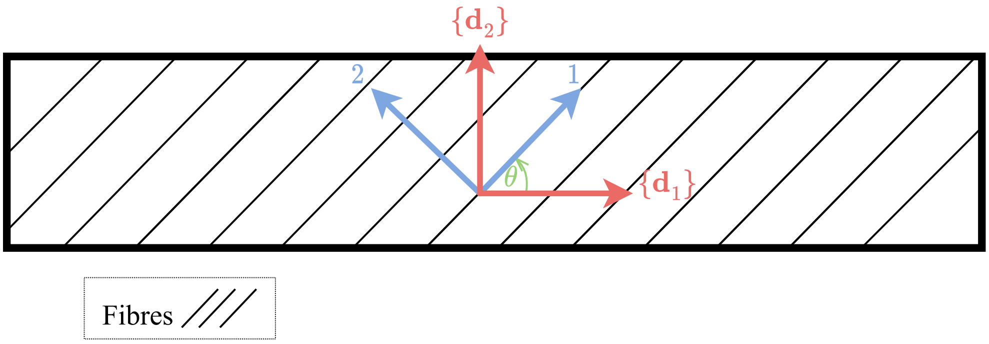

Figure 2.8. In-plane transformation from the material coordinate system (12-system)

Often, the material properties of a laminae are expressed using a coordinate system along the fibres. Thus, an in-plane rotation introduces an orthotropic material into the problem as illustrated in Figure 2.8.

Element coordinate system

An element coordinate system is utilised to express the stiffness matrix before it is transformed into global coordinates. In this system, the orthotropic materials can be formulated and transformed to the natural coordinates, r, s, t, via the covariant or contravariant projection. As the transformation from the material coordinate system to the element coordinate system involves an in-plane rotation, the third base vector of the element coordinate system ($\{\mathbf{d}_3\}$) is derived from the Covariant coordinate system. This choice is made because it ensures that the material and element coordinate systems are perpendicular to the surface. This alignment is desirable because the constitutive properties of the laminae will be more precise when the material coordinate system aligns with the principal directions of the orthotropic material.

2.2.2 Mapping to natural coordinates

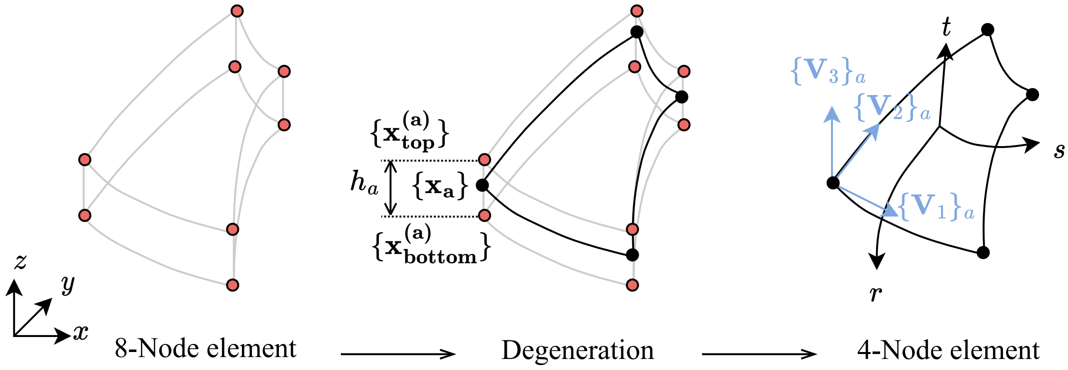

Figure 2.9. 8-node continuum element degenerated into a 4-shell element represented in the Curvilinear r, s, t coordinate system

The geometry and displacement of the 4-node element are formulated as proposed by Ahmad et al. (1970) using a degenerated 8-node element. Here, the geometry has a 2-dimensional surface description where the dimensions out of the surface plane can be calculated using a unit vector called node director $\{\mathbf{V}^{(\mathbf{a})}_{\mathbf{3}}\}$ in each node a as shown in Figure 2.9.

Interpolation of the geometry

The nodes of the 4-node shell are introduced into the middle of the 8-node continuum element as shown in Figure 2.9 and Eq. (2.4).

$$\{\mathbf{x_a}\} = \frac{\{\mathbf{x}^{(\mathbf{a})}_{\mathbf{top}}\} + \{\mathbf{x}^{(\mathbf{a})}_{\mathbf{bottom}}\}}{2}, \qquad a = 1, \cdots, 4 \tag{2.4}$$

$\{\mathbf{x}\}$ indicates the nodal position expressed in global coordinates. To represent the geometry out of the surface plane, it is necessary to introduce the node director $\{\mathbf{V}^{(\mathbf{a})}_{\mathbf{3}}\}$ at each node a. The node director can be obtained using Eq. (2.5), where h_a is the thickness of the element at node a as shown in Figure 2.9.

$$\{\mathbf{V}^{(\mathbf{a})}_{\mathbf{3}}\} = \frac{\{\mathbf{x}^{(\mathbf{a})}_{\mathbf{top}}\} - \{\mathbf{x}^{(\mathbf{a})}_{\mathbf{bottom}}\}}{h_a}, \qquad a = 1, \cdots, 4 \tag{2.5}$$

The eight nodes of the continuum element can be mapped to the natural coordinates as shown in Eq. (2.6).

$$N_a(r,s,t) = \frac{1}{8}(1 \pm r)(1 \pm s)(1 \pm t), \qquad a = 1, \cdots, 4 \tag{2.6}$$

The 3-dimensional shape functions in Eq. (2.6), can be reformulated into through-the-thickness shape functions, $N_t^{(a)}(t)$ in Eq. (2.7) and in-plane shape functions $N_{2D}^{(a)}(r,s)$ in Eq. (2.8).

$$N_t^{(a)}(t) = \frac{1}{2}(1 \pm t), \qquad a = 1, \cdots, 4 \tag{2.7}$$

$$N_{2D}^{(a)}(r,s) = \frac{1}{4}(1 \pm r)(1 \pm s), \qquad a = 1, \cdots, 4 \tag{2.8}$$

The geometry in the r, s, t-system can be calculated using Eq. (2.9)

$$\{\mathbf{x_{rst}}\} = [\mathbf{N}]\{\mathbf{x_a}\} = \sum_{a=1}^{4} \frac{1}{2}(1+t) N_{2D}^{(a)} \{\mathbf{x_{top}^{(a)}}\} + \sum_{a=1}^{4} \frac{1}{2}(1-t) N_{2D}^{(a)} \{\mathbf{x_{bottom}^{(a)}}\} \tag{2.9}$$

Reformulating Eq. (2.9) using factorisation of $N_{2D}^{(a)}$ results in Eq. (2.10).

$$\{\mathbf{x_{rst}}\} = \sum_{a=1}^{4} N_{2D}^{(a)} \left(\frac{1}{2}\{\mathbf{x_{top}^{(a)}}\} + \frac{1}{2}\{\mathbf{x_{bottom}^{(a)}}\}\right) + \sum_{a=1}^{4} \frac{t}{2} N_{2D}^{(a)} \left(\{\mathbf{x_{top}^{(a)}}\} - \{\mathbf{x_{bottom}^{(a)}}\}\right) \tag{2.10}$$

It can be observed that the initial parenthesis in Eq. (2.10) is equal to the nodal values in Eq. (2.4) and Figure 2.9. The product of h_a and the node director from Eq. (2.5) can be identified in the second parenthesis Eq. (2.10). Hence, the reformulation of Eq. (2.10) enables the interpolation of the geometry by a surface description in Eq. (2.11).(Lund, 2022)

$$\{\mathbf{x_{rst}}\} = \sum_{a=1}^{4} N_{2D}^{(a)} \{\mathbf{x_a}\} + \sum_{a=1}^{4} \frac{t}{2} N_{2D}^{(a)} h_a \{\mathbf{V_3^{(a)}}\} \tag{2.11}$$

Interpolation of the displacements

Following Eq. (2.1), it is necessary to derive an expression for the displacements $\{\mathbf{u}\}$ in the r, s, t-coordinate system. This can be achieved by utilising the nodal position before deformation $\{\mathbf{X}\}$ and the nodal position after deformation $\{\mathbf{x}\}$ as shown in Eq. (2.12).

$$\{\mathbf{u}\} = \{\mathbf{x}\} - \{\mathbf{X}\} \tag{2.12}$$

There is no significant difference in the geometry interpolation, whether performed in the initial or deformed configuration. Eq. (2.11) is used with the initial or deformed configuration values. By substitution of Eq. (2.11) in the initial and deformed configuration, the displacements can be calculated as shown in Eq. (2.13).

$$\{\mathbf{u_{rst}}\} = \sum_{a=1}^{4} N_{2D}^{(a)} \{\mathbf{u_a}\} + \sum_{a=1}^{4} \frac{t}{2} N_{2D}^{(a)} h_a \left(\{\mathbf{v_3^{(a)}}\} - \{\mathbf{V_3^{(a)}}\}\right) \tag{2.13}$$

Here, $\{\mathbf{u_a}\}$ is the nodal mid-surface displacement vector and $\{\mathbf{v_3^{(a)}}\} - \{\mathbf{V_3^{(a)}}\}$ in the parenthesis in Eq. (2.13) $\{\mathbf{v_3^{(a)}}\} - \{\mathbf{V_3^{(a)}}\}$ is the change in the node director coordinates systems. $\{\mathbf{v_3^{(a)}}\}$ and $\{\mathbf{V_3^{(a)}}\}$ are, respectively, the node director before deformation and at the initial configuration. The deformed configuration can be obtained by subjecting the node director coordinate system to in-plane rotations around $\{\mathbf{V_2^{(a)}}\}$ and $\{\mathbf{V_1^{(a)}}\}$, as illustrated in Figure 2.10. This results in the displacement of the node director over an arc length.

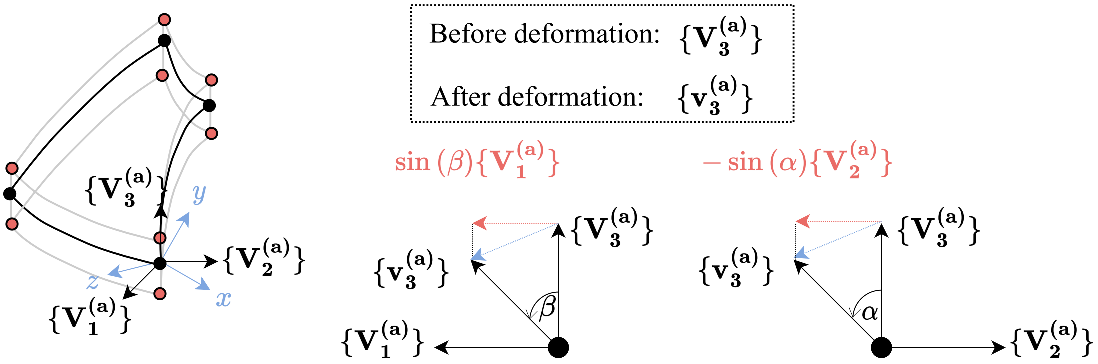

Figure 2.10. Deformation by in-plane rotations around $\{\mathbf{V_2^{(a)}}\}$ and $\{\mathbf{V_1^{(a)}}\}$

An approximation to the arc length can be achieved by assuming small rotations, which lead to the following two statements:

- The arc length produced by rotation of $\{\mathbf{V_3^{(a)}}\}$ can be approximated by the displacement vector in the $\{\mathbf{V_1^{(a)}}\}$ and $\{\mathbf{V_2^{(a)}}\}$ directions. This is illustrated with red in Figure 2.10
- The displacement vector in the $\{\mathbf{V_1^{(a)}}\}$ and $\{\mathbf{V_2^{(a)}}\}$ directions can be approximated using $\sin(\beta)\{\mathbf{V_1^{(a)}}\} \approx \beta\{\mathbf{V_1^{(a)}}\}$

This approximation works well for small rotations and can be substituted into Eq. (2.13) to obtain the displacements using Eq. (2.14).

$$\{\mathbf{u_{rst}}\} = \sum_{a=1}^{4} N_{2D}^{(a)}\{\mathbf{u_a}\} + \sum_{a=1}^{4} \frac{t}{2} N_{2D}^{(a)} h_a \left(\beta\{\mathbf{V_1^{(a)}}\} - \alpha\{\mathbf{V_2^{(a)}}\}\right) = [\mathbf{N}]\{\mathbf{d}\} \tag{2.14}$$

Eq. (2.14) reveal one of the disadvantage of the 4-shell element since $\{\mathbf{d}\} = \{x, y, z, \alpha, \beta\}^T$ and therefor only has 5 DOF. The DoF that does not exist for the 4-shell element is called the drilling DoF. This disadvantage is because moments cannot be applied around the drilling DoF. Therefore, commercial software and the stabilised element by Stagsted and Bertelsen (2023) uses artificial penalty stiffness to address this issue.

To calculate the displacement in Eq. (2.14) it is necessary to establish $\{\mathbf{V_1^{(a)}}\}$ and $\{\mathbf{V_2^{(a)}}\}$. These node directors can be calculated using Eq. (2.15) and (2.16).

$$\{\mathbf{V_1^{(a)}}\} = \frac{\{\hat{\mathbf{e}}_\mathbf{2}\} \times \{\mathbf{V_3^{(a)}}\}}{|\{\hat{\mathbf{e}}_\mathbf{2}\} \times \{\mathbf{V_3^{(a)}}\}|} \tag{2.15}$$

Here $\{\hat{\mathbf{e}}_\mathbf{2}\}$ is the second Cartesian basis vector and the orientation of $\{\mathbf{V_1^{(a)}}\}$ is scaled with the magnitude to ensure $\{\mathbf{V_1^{(a)}}\}$ is a unit vector. As both $\{\mathbf{V_1^{(a)}}\}$ and $\{\mathbf{V_3^{(a)}}\}$ are unit vectors, the cross product is used to calculate $\{\mathbf{V_2^{(a)}}\}$. Lund (2022)

$$\{\mathbf{V_2^{(a)}}\} = \{\mathbf{V_3^{(a)}}\} \times \{\mathbf{V_1^{(a)}}\} \tag{2.16}$$

2.2.3 Displacement-Strain Equations

Choosing appropriate definitions of strain and stress is crucial to ensure work consistency, as it makes the strain energy in Eq. (2.1) independent of the definitions (Lund and Lindgaard, 2022). In linear problems, the linear strain tensor with the Cauchy stress tensor is work consistent. However, laminated composites are susceptible to failure caused by buckling, which is inherently a geometrical non-linear problem. Therefore, the Green-Lagrange strain tensor is used, which is often formulated in global coordinates. To calculate the Green-Lagrange strain tensor using the covariant components Appendix A derives Eq. (2.17) using the approach by Vu-Quoc and Tan (2003).

$$E_{ij} = \frac{1}{2}\left(\underbrace{\{\mathbf{G}_i\}\frac{\partial\{\mathbf{u_{rst}}\}}{r^j} + \frac{\partial\{\mathbf{u_{rst}}\}}{r^i}\{\mathbf{G}_j\}}_{\text{Linear term}} + \underbrace{\frac{\partial\{\mathbf{u_{rst}}\}}{r^i}\frac{\partial\{\mathbf{u_{rst}}\}}{r^j}}_{\text{Nonlinear term}} \right) \tag{2.17}$$

The notation used in the previous sections has been adapted to denote $\{\mathbf{G}_i\}$ and $\{\mathbf{G}_j\}$ as the covariant base vectors before deformation. The expression for the Green-Lagrange strain tensor in Eq. (2.17) can be represented in FE-form by using Eq. (2.18), where $[\mathbf{B}]$ is the strain displacement matrix. $[\mathbf{B}]$ consists of a linear component $[\mathbf{B_0}]$ and a nonlinear strain displacement matrix $[\mathbf{B_L}]$.

$$\{\varepsilon_{\mathbf{Cov}}\} = [\mathbf{B}]\,\{\mathbf{d}\} = \big([\mathbf{B_0}] + [\mathbf{B_L(\{d\})}]\big)\{\mathbf{d}\} \tag{2.18}$$

The displacement vector is calculated using Eq. (2.14) and, since only the shape functions depend on the natural coordinates $r_i = r, s, t$, the partial derivatives in Eq. (2.17) can be expressed as shown in Eq. (2.19).

$$\frac{\partial\{\mathbf{u_{rst}}\}}{r^j} = \frac{\partial\,[\mathbf{N}]}{r^j}\{\mathbf{d}\} \tag{2.19}$$

Substitution of Eq. (2.19) into Eq. (2.17) yields Eq. (2.20), which can be factorised to obtain the covariant Green-Lagrange strain tensor on FE-form in Eq. (2.21)

$$\{\varepsilon_{\mathbf{Cov}}\} = \frac{1}{2}\left(\{\mathbf{G}_i\}\frac{\partial\,[\mathbf{N}]}{r^j}\{\mathbf{d}\} + \frac{\partial\,[\mathbf{N}]}{r^i}\{\mathbf{d}\}\{\mathbf{G}_j\} + \frac{\partial\,[\mathbf{N}]}{r^i}\{\mathbf{d}\}\frac{\partial\,[\mathbf{N}]}{r^j}\{\mathbf{d}\}\right) \tag{2.20}$$

$$= \left(\underbrace{\frac{1}{2}\left(\{\mathbf{G}_i\}\frac{\partial\,[\mathbf{N}]}{r^j} + \frac{\partial\,[\mathbf{N}]}{r^i}\{\mathbf{G}_j\}\right)}_{=[\mathbf{B_0}]} + \underbrace{\frac{1}{2}\frac{\partial\,[\mathbf{N}]}{r^i}\{\mathbf{d}\}\frac{\partial\,[\mathbf{N}]}{r^j}}_{=[\mathbf{B_L(\{d\})}]} \right)\{\mathbf{d}\} \tag{2.21}$$

If a linear analysis is performed, the covariant linear strain definition on FE-form can be obtained by eliminating $[\mathbf{B_L(\{d\})}]$ from Eq. (2.21). (Stagsted and Bertelsen, 2023)

2.2.4 Strain-Stress Equations

In continuum mechanics, the Cauchy stress tensor is defined as the force and unit area ratio in the deformed configuration. This differs from the 2nd Piola-Kirchhoff stress tensor, defined as the force ratio from the undeformed configuration acting on an undeformed unit area. (Lund and Lindgaard, 2022) According to Vu-Quoc and Tan (2003), when using the Green-Lagrange strain tensor, it is necessary to use the contravariant 2nd Piola-Kirchhoff stress tensor to ensure work consistency. The contravariant 2nd Piola-Kirchhoff stress tensor is expressed as shown in Vu-Quoc and Tan (2003) and Eq. (2.22)

$$[\mathbf{S}] = S^{ij}\{\mathbf{G}_i\}\{\mathbf{G}_j\}^T \tag{2.22}$$

The contravariant stress tensor S^{ij} can be expressed using Eq. (2.23) and the covariant Green-Lagrange strain tensor defined in subsection 2.2.3.

$$S^{ij} = C^{ijkl}E_{kl} \tag{2.23}$$

The constitutive properties in the contravariant coordinate system C^{ijkl} is the last expression that must be determined to calculate the contravariant 2nd Piola-Kirchhoff stress tensor. (Stagsted and Bertelsen, 2023)

The constitutive properties of a lamina are defined in the material coordinate system, and it is essential to consider this aspect when expressing C^{ijkl}. A plane stress assumption is introduced through the constitutive properties in the material system, shown in Eq. (2.24), which has no constitutive properties in the transverse normal direction. The assumption contradicts the FSDT assumption that considers plane strain. Despite this, combining the plane stress and plane strain assumption is commonly used for FSDT-based shell elements. It has been extensively used for a wide range of problems with thin composite structures.

$$[\mathbf{C}]_{12} = \begin{bmatrix} \frac{E_1}{1-\nu_{12}\nu_{21}} & \frac{\nu_{21}E_1}{1-\nu_{12}\nu_{21}} & 0 & 0 & 0 & 0 \\ \frac{\nu 21E_1}{1-\nu_{12}\nu_{21}} & \frac{E_2}{1-\nu_{12}\nu_{21}} & 0 & 0 & 0 & 0 \\ 0 & 0 & 0 & 0 & 0 & 0 \\ 0 & 0 & 0 & G_{12} & 0 & 0 \\ 0 & 0 & 0 & 0 & k_1G_{23} & 0 \\ 0 & 0 & 0 & 0 & 0 & k_2G_{13} \end{bmatrix} \tag{2.24}$$

The shear correction factors are in this work set to the value of an isotropic plate, hence $k_1 = 5/6$ and $k_2 = 5/6$.

The transformation of the constitutive properties can be performed step-wise, where the in-plane transformation matrix $[\mathbf{T}_{\boldsymbol{\theta}}]$ in Eq. (2.25) is used to transform the constitutive properties to the element system as shown in Eq. (2.26).

$$[\mathbf{T}_{\boldsymbol{\theta}}] = \begin{bmatrix} a^2 & b^2 & 0 & ab & 0 & 0 \\ b^2 & a^2 & 0 & -ab & 0 & 0 \\ 0 & 0 & 1 & 0 & 0 & 0 \\ -2ab & 2ab & 0 & a^2-b^2 & 0 & 0 \\ 0 & 0 & 0 & 0 & a & -b \\ 0 & 0 & 0 & 0 & b & a \end{bmatrix} \quad \textbf{where: } a = \cos(\theta) \text{ and } b = \sin(\theta) \tag{2.25}$$

$$[\mathbf{C_d}] = [\mathbf{T}_{\boldsymbol{\theta}}]^T [\mathbf{C_{12}}] [\mathbf{T}_{\boldsymbol{\theta}}] \tag{2.26}$$

From the element system, a transformation to the contravariant components can be obtained using the inner product of each element basis vectors $\{\mathbf{d}_j\}$ and the contravariant base vectors $\{\mathbf{G}_i\}$ as shown in Eq. (2.27).

$$t_{ij} = \{\mathbf{d}_j\} \cdot \{\mathbf{G}_i\}, \quad i = 1,2,3 \quad j = 1,2,3 \tag{2.27}$$

The t_{ij}-values from Eq. (2.27) are inserted into Eq. (2.28) to obtain $\left[\mathbf{T}^{\mathbf{Con}}\right]$.

$$[\mathbf{T}^{\mathbf{con}}] = \begin{bmatrix} t_{11}^2 & t_{12}^2 & t_{13}^2 & t_{11}t_{12} & t_{11}t_{13} & t_{12}t_{13} \\ t_{21}^2 & t_{22}^2 & t_{23}^2 & t_{21}t_{22} & t_{21}t_{23} & t_{22}t_{23} \\ t_{31}^2 & t_{32}^2 & t_{33}^2 & t_{31}t_{32} & t_{31}t_{33} & t_{32}t_{33} \\ 2t_{11}t_{21} & 2t_{12}t_{22} & 2t_{13}t_{23} & t_{11}t_{22}+t_{12}t_{21} & t_{11}t_{23}+t_{13}t_{21} & t_{12}t_{23}+t_{13}t_{22} \\ 2t_{21}t_{31} & 2t_{22}t_{32} & 2t_{23}t_{33} & t_{21}t_{32}+t_{22}t_{31} & t_{21}t_{33}+t_{23}t_{31} & t_{22}t_{33}+t_{23}t_{32} \\ 2t_{11}t_{31} & 2t_{12}t_{32} & 2t_{13}t_{33} & t_{11}t_{32}+t_{12}t_{31} & t_{11}t_{33}+t_{13}t_{31} & t_{12}t_{33}+t_{13}t_{32} \end{bmatrix} \tag{2.28}$$

C^{ijkl} is therefore on FE-form calculated using Eq. (2.29)

$$[\mathbf{C}^{\mathbf{con}}] = \left[\mathbf{T}^{\mathbf{Con}}\right]^T \Big([\mathbf{T}_{\boldsymbol{\theta}}]^T [\mathbf{C_{12}}] [\mathbf{T}_{\boldsymbol{\theta}}]\Big) \left[\mathbf{T}^{\mathbf{Con}}\right] \tag{2.29}$$

An FE formulation of the 4-node shell element without stabilisation can be derived from the previous equations. However, the shell element will display both transverse and in-plane shear locking and, therefore, to mitigate this issue, Enhanced assumed Strain (EAS) and Mixed Interpolation of Tensorial Component (MITC) stabilisation can be applied. (Lund, 2022)

2.2.5 Mixed Interpolation of Tensorial Component

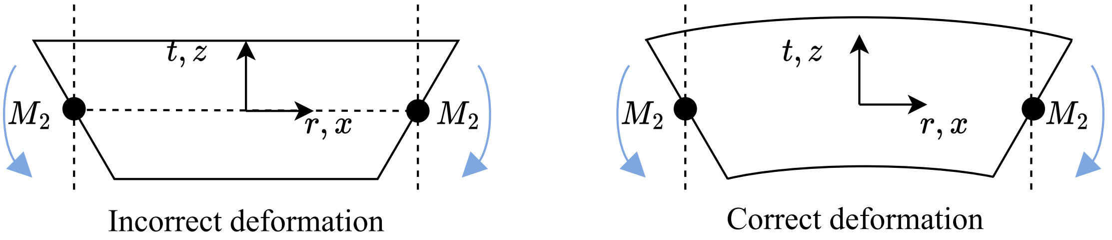

Figure 2.11. The 4-node shell element without stabilisation suffers from transverse shear locking due to incorrect deformation when subjected to bending moments

The transverse shear locking issue occurs as illustrated in Figure 2.11 due to inaccurate deformations from the overly stiff element behaviour when subjected to bending moments. Transverse shear locking is a well-studied phenomenon. Therefore, several attractive solutions have been proposed to address this issue.

In explicit dynamics and non-linear problems, reduced integration is often used for computational efficiency, although it can result in zero-energy modes. A popular solution is to apply hourglass control, where artificial stiffness is added to avoid zero-energy modes.

The MITC-method by Dvorkin and Bathe (1984) is a part of another class of stabilisation methods called Assumed Natural Strain (ANS)-methods or $\bar{B}$-methods since these methods re-interpolate the original strain-displacement matrix. Dvorkin and Bathe (1984) realised that the most accurate covariant transverse shear strains in the linear element can be calculated in the re-interpolation points (also called tying points) A, B, C, D in Figure 2.12.

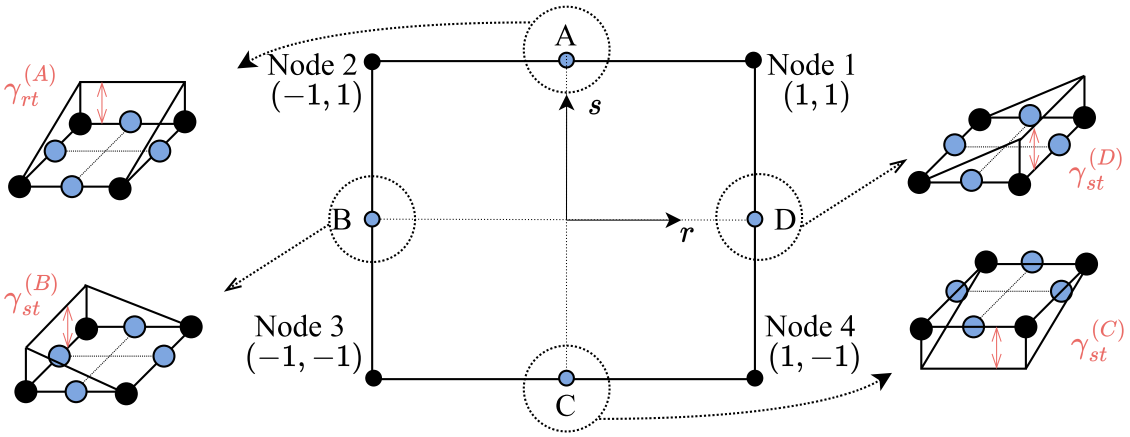

Figure 2.12. The transverse shear strain distribution at each tying point

The covariant transverse shear strains evaluated in the tying points in Figure 2.12 are used to obtain the correct covariant shear strain distribution by a re-interpolation as shown in Eq. (2.30) and (2.31).

$$\gamma_{rt} = \frac{1}{2}(1+s)\,\gamma_{rt}^{(A)} + \frac{1}{2}(1-s)\,\gamma_{rt}^{(C)} = N_{rt}^{(A)}\gamma_{rt}^{(A)} + N_{rt}^{(C)}\gamma_{rt}^{(C)} \tag{2.30}$$

$$\gamma_{st} = \frac{1}{2}(1+r)\,\gamma_{st}^{(D)} + \frac{1}{2}(1-r)\,\gamma_{st}^{(B)} = N_{st}^{(D)}\gamma_{st}^{(D)} + N_{st}^{(B)}\gamma_{13}^{(st)} \tag{2.31}$$

The re-interpolations in Eq. (2.30) and (2.31) are expressed on FE-form as shown in Eq. (2.32) and (2.33).

$$\{\mathbf{B}_{\mathbf{rt}}^{\mathbf{(MITC)}}\}^T = N_{rt}^{(A)}\{\mathbf{B}_{\mathbf{rt}}^{\mathbf{(A)}}\}^T + N_{rt}^{(C)}\{\mathbf{B}_{\mathbf{rt}}^{\mathbf{(C)}}\}^T \tag{2.32}$$

$$\{\mathbf{B}_{\mathbf{st}}^{\mathbf{(MITC)}}\}^T = N_{st}^{(D)}\{\mathbf{B}_{\mathbf{st}}^{\mathbf{(D)}}\}^T + N_{st}^{(B)}\{\mathbf{B}_{\mathbf{st}}^{\mathbf{(B)}}\}^T \tag{2.33}$$

Eq. (2.32) and (2.33) are inserted in the fourth and fifth row in the strain displacement matrix from subsection 2.2.3 as these rows represent the covariant transverse shear strain. (Stagsted and Bertelsen, 2023)

It is important to acknowledge that alternative approaches to address transverse shear locking can achieve comparable results for problems involving flat and undistorted plates but may differ when considering curved shell elements.(Lund, 2022)

2.2.6 Enhanced Assumed Strain-formulation

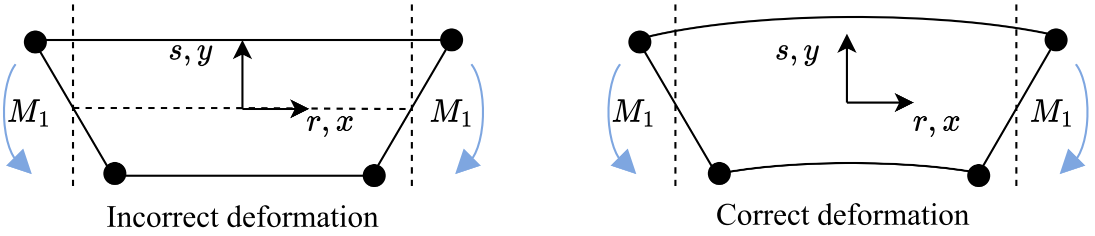

Figure 2.13. The 4-node shell element without stabilisation suffers from in-plane shear locking due to parasitic shear strain

In-plane shear locking occurs due to parasitic inplane shear strains when subjected to pure bending as shown in Figure 2.13. Stabilisation methods to mitigate in-plane shear locking have been thoroughly investigated and developed. Similar to transverse shear locking, reduced integration eliminates in-plane shear locking. However, reduced integration faces the same challenges addressed in subsection 2.2.5. A popular method for solid elements is the incompatible modes method. It allows the displacement field to violate the compatibility equations from elasticity theory by adding incompatible modes and uses modified integration to pass the patch test. Later, EAS formulations were proposed to address the in-plane shear locking problem while avoiding mixed integration.(Lund, 2022) Simo and Rifai (1990) introduced an enhanced strain field $\{\boldsymbol{\varepsilon}_{\mathbf{EAS}}\}$ in the variational formulation. The strain field obtained in subsection 2.2.3 is in this subsection referred to as the compatible strain field $\{\varepsilon_{\mathbf{Comp}}\}$ and an independent strain field $\{\tilde{\varepsilon}_{\mathbf{Ind}}\}$ is added to obtain an enhanced strain field $\{\varepsilon_{\mathbf{EAS}}\}$ as shown in Eq. (2.34).

$$\{\varepsilon_{\mathbf{EAS}}\} = \{\varepsilon_{\mathbf{Comp}}\} + \{\tilde{\varepsilon}_{\mathbf{Ind}}\} \tag{2.34}$$

The independent strain field is defined in Eq. (2.35) and enhances the compatible strain field by including additional linear terms to the in-plane shear strain and in-plane normal strains.

$$\{\varepsilon_{\mathbf{Ind}}\} = \{\mathbf{M}\}\{\boldsymbol{\alpha}\} \quad \text{where} \quad \{\mathbf{M}\} = \begin{bmatrix} r & 0 & 0 & 0 \\ 0 & s & 0 & 0 \\ 0 & 0 & 0 & 0 \\ 0 & 0 & r & s \\ 0 & 0 & 0 & 0 \\ 0 & 0 & 0 & 0 \end{bmatrix} \tag{2.35}$$

The independent strain field in Eq. (2.35) introduces four internal DoFs $\{\boldsymbol{\alpha}\}$ for each element in the model. However, the static condensation makes it computationally attractive by removing the internal DoFs from the global equilibrium equation. Therefore, MITC is a computationally efficient method for eliminating in-plane shear locking. (Lund, 2022)

The original formulation of the independent strain field by Simo and Rifai (1990) in Eq. (2.35) is derived from a local coordinate system in the middle of the element. However, the element coordinate system does not necessarily have to be located in the middle of the 4-node shell element. Furthermore, the independent strain field must be transformed to the covariant coordinate system to remain consistent with the formulation in subsection 2.2.3. Therefore, a Cartesian coordinate system is established in the middle of the element to obtain a transformation matrix $[\mathbf{T_M}]$ using the inner product of the Cartesian base vectors in the middle of the element and the covariant base vectors and Eq. (2.27) and (2.28). The transformation of the independent strain field to the covariant coordinate system is achieved using Eq. (2.36).

$$\{\tilde{\varepsilon}_{\mathbf{Ind}}\} = [\mathbf{T_M}]\{\varepsilon_{\mathbf{Ind}}\} = \{\tilde{\mathbf{M}}\}\{\boldsymbol{\alpha}\} = [\mathbf{T_M}]\{\mathbf{M}\}\{\boldsymbol{\alpha}\} \tag{2.36}$$

The global equilibrium equation used to model fibre-reinforced laminated composites can be derived from the displacement interpolation in section 2.2.2, stress definition in subsection 2.2.4 and the strain representation obtained in subsection 2.2.3, 2.2.5 and 2.2.6.

Several requirements are emphasised by Simo and Rifai (1990) to ensure a unique solution and pass the patch test to ensure convergence:

- To avoid a singular system, it is necessary for the strain fields specified Eq. (2.34) to be linearly independent.
- The independent strain field is not a physical strain. Therefore, to prevent the independent strain field from contributing to the strain energy, it is essential to ensure orthogonality of the strain fields in Eq. (2.34)
- If the strain fields in Eq. (2.34) are orthogonal, the stress field must be at least piece-wise constant to satisfy the patch test.

The thesis does not aim to derive the global equilibrium equation, but Stagsted and Bertelsen (2023) serves as great literature for more information on the derivation.

2.2.7 Global Equilibrium Equation

The global equilibrium equation $[\mathbf{K}]\{\mathbf{D}\} = \{\mathbf{F}\}$ is formulated from the equilibrium equation on the element level. This equation for the geometric non-linear 4-node shell element with EAS and MITC is formulated by Stagsted and Bertelsen (2023) using Eq. (2.37).

$$\begin{bmatrix} [\mathbf{k_{uu}}]_e & [\mathbf{k_{u\boldsymbol{\alpha}}}]_e \\ [\mathbf{k_{\boldsymbol{\alpha}u}}]_e & [\mathbf{k_{\boldsymbol{\alpha\alpha}}}]_e \end{bmatrix} \begin{bmatrix} \Delta\{\mathbf{d}\}_e \\ \Delta\{\boldsymbol{\alpha}\}_e \end{bmatrix} = - \begin{bmatrix} \{\mathbf{f_{int}}\}_e - \{\mathbf{f_{ext}}\}_e \\ \{\mathbf{f_{EAS}}\}_e \end{bmatrix} \tag{2.37}$$

Since it is the non-linear formulation, Δ indicates the increment from applying iterative methods, such as the arc length method, Newton-Raphson method or Broyden-Fletcher-Goldfarb-Shanno method, to solve the non-linear equations.

The force vector on the right-hand side in Eq. (2.37) consists a force vector related to the internal DoF $\{\mathbf{f_{EAS}}\}_e$ in Eq. (2.38), external force vector $\{\mathbf{f_{ext}}\}_e$ in Eq. (2.39), and internal $\{\mathbf{f_{int}}\}_e$ force vector in Eq. (2.40).

$$\{\mathbf{f_{EAS}}\}_e = \int_V \left[\tilde{\mathbf{M}}\right]^T \{\boldsymbol{\sigma}\}\, dV \tag{2.38}$$

$$\{\mathbf{f_{ext}}\}_e = \int_V [\mathbf{N}]^T \{\mathbf{B}\}\, dV + \int_V [\mathbf{N}]^T \{\mathbf{T}\}\, dS \tag{2.39}$$

$$\{\mathbf{f_{int}}\}_e = \int_V [\mathbf{B}]^T \{\boldsymbol{\sigma}\}\, dV \tag{2.40}$$

The element stiffness matrix is defined by the matrices in Eq. (2.41), (2.42), (2.43) and (2.44) (Stagsted and Bertelsen, 2023).

$$[\mathbf{k_{uu}}]_e = \int_V \left([\mathbf{B}]^T [\mathbf{C^{con}}] [\mathbf{B}] + \frac{d\,[\mathbf{B}]^T}{d\{\mathbf{d}\}} \{\boldsymbol{\sigma}\} \right) dV \tag{2.41}$$

$$[\mathbf{k_{u\boldsymbol{\alpha}}}]_e = \int_V [\mathbf{B}]^T [\mathbf{C^{con}}] [\tilde{\mathbf{M}}]\; dV \tag{2.42}$$

$$[\mathbf{k_{\boldsymbol{\alpha}u}}]_e = [\mathbf{k_{\boldsymbol{\alpha}u}}]_e^T = \int_V [\tilde{\mathbf{M}}]^T [\mathbf{C^{con}}] [\mathbf{B}]\; dV \tag{2.43}$$

$$[\mathbf{k_{\boldsymbol{\alpha\alpha}}}]_e = \int_V [\tilde{\mathbf{M}}]^T [\mathbf{C^{con}}] [\tilde{\mathbf{M}}]\; dV \tag{2.44}$$

Static condensation eliminates the internal DoF from the global equilibrium equation and increases computational efficiency. Therefore $\Delta\{\boldsymbol{\alpha}\}_e$ is isolated in Eq. (2.37) as shown in Eq. (2.45)

$$\begin{aligned} -\{\mathbf{f_{EAS}}\}_e &= [\mathbf{k_{\boldsymbol{\alpha}u}}]_e \,\Delta\{\mathbf{d}\}_e + [\mathbf{k_{\boldsymbol{\alpha\alpha}}}]_e \,\Delta\{\boldsymbol{\alpha}\}_e \;\Downarrow \\ \Delta\{\boldsymbol{\alpha}\}_e &= [\mathbf{k_{\boldsymbol{\alpha\alpha}}}]_e^{-1} \left(-\{\mathbf{f_{EAS}}\}_e - [\mathbf{k_{\boldsymbol{\alpha}u}}]_e \,\Delta\{\mathbf{d}\}_e\right) \end{aligned} \tag{2.45}$$

Eq. (2.45) is substituted into the upper part of Eq. (2.37) to obtain Eq. (2.46).

$$[\mathbf{k_{uu}}]_e \,\Delta\{\mathbf{d}\}_e - [\mathbf{k_{u\boldsymbol{\alpha}}}]_e [\mathbf{k_{\boldsymbol{\alpha\alpha}}}]_e^{-1} \left(\{\mathbf{f_{EAS}}\}_e + [\mathbf{k_{\boldsymbol{\alpha}u}}]_e \,\Delta\{\mathbf{d}\}_e\right) = -\left(\{\mathbf{f_{int}}\}_e - \{\mathbf{f_{ext}}\}_e\right) \tag{2.46}$$

Eq. (2.46) can be rearranged to obtain the same expression as Klinkel and Wagner (1997), Klinkel et al. (1999), Vu-Quoc and Tan (2003) and Stagsted and Bertelsen (2023) in Eq. (2.47), here $\{\mathbf{r}\}_e$ is the element residual vector and $[\mathbf{k_T}]_e$ is the element tangent stiffness matrix.

$$\underbrace{\left([\mathbf{k_{uu}}]_e - [\mathbf{k_{\boldsymbol{\alpha}u}}]_e^T [\mathbf{k_{\boldsymbol{\alpha\alpha}}}]_e^{-1} [\mathbf{k_{\boldsymbol{\alpha}u}}]_e\right)}_{[\mathbf{k_T}]_e} \Delta\{\mathbf{d}\}_e = -\left(\underbrace{\{\mathbf{f_{int}}\}_e - [\mathbf{k_{\boldsymbol{\alpha}u}}]_e^T [\mathbf{k_{\boldsymbol{\alpha\alpha}}}]_e^{-1} \{\mathbf{f_{EAS}}\}_e - \{\mathbf{f_{ext}}\}_e}_{\{\mathbf{r}\}_e}\right) \tag{2.47}$$

The internal DoF $\{\boldsymbol{\alpha}\}_e$ is eliminated from the equilibrium equation, which is computationally attractive.

2.2.8 Volume integration

To evaluate the volume integral in the natural coordinate system, the Jacobian determinant $|J|$ is utilised to transform the integration variables from global coordinates to natural coordinates, as demonstrated in Eq. (2.48), (2.49) and (2.50).

$$[\mathbf{k_{uu}}]_e = \int_1^1 \int_1^1 \int_1^1 \underbrace{\left([\mathbf{B}]^T [\mathbf{C^{con}}] [\mathbf{B}] + \frac{d\,[\mathbf{B}]^T}{d\{\mathbf{d}\}} \{\boldsymbol{\sigma}\} \right) |J|}_{[\boldsymbol{\phi}_\mathbf{1}\mathbf{(r,s,t)}]} \; drdsdt \tag{2.48}$$

$$[\mathbf{k_{\boldsymbol{\alpha}u}}]_e = [\mathbf{k_{\boldsymbol{\alpha}u}}]_e^T = \int_1^1 \int_1^1 \int_1^1 \underbrace{[\tilde{\mathbf{M}}]^T [\mathbf{C^{con}}] [\mathbf{B}]}_{[\boldsymbol{\phi}_\mathbf{2}\mathbf{(r,s,t)}]} \; drdsdt \tag{2.49}$$

$$[\mathbf{k_{\boldsymbol{\alpha\alpha}}}]_e = \int_1^1 \int_1^1 \int_1^1 \underbrace{[\tilde{\mathbf{M}}]^T [\mathbf{C^{con}}] [\tilde{\mathbf{M}}] \frac{1}{|J|}}_{[\boldsymbol{\phi}_\mathbf{3}\mathbf{(r,s,t)}]} \; drdsdt \tag{2.50}$$

The integration through the laminate thickness can be addressed using various approaches. One of the most efficient methods for the computation is explicit thickness integration. This is because the relationship between the number of laminae and the time taken for the stiffness matrix to be assembled remains nearly constant, as demonstrated by Hvejsel and Hansen (2007) for a 9-node isoparametric shell element. However, the accuracy of the integration decreases as the curvature increases. Therefore, this method is often used for flat or nearly flat shells. Layer-wise numerical thickness integration is often preferred for shells with higher curvature as it provides a more accurate solution and models the stiffness coupling effects. However, it has a computational cost, especially when the laminate has many layers.(Lund, 2022) Given the complex geometry of wind turbine blades, characterised by multiple curved surfaces with high curvature, the layer-wise numerical thickness integration method is carried out to obtain more accurate results.

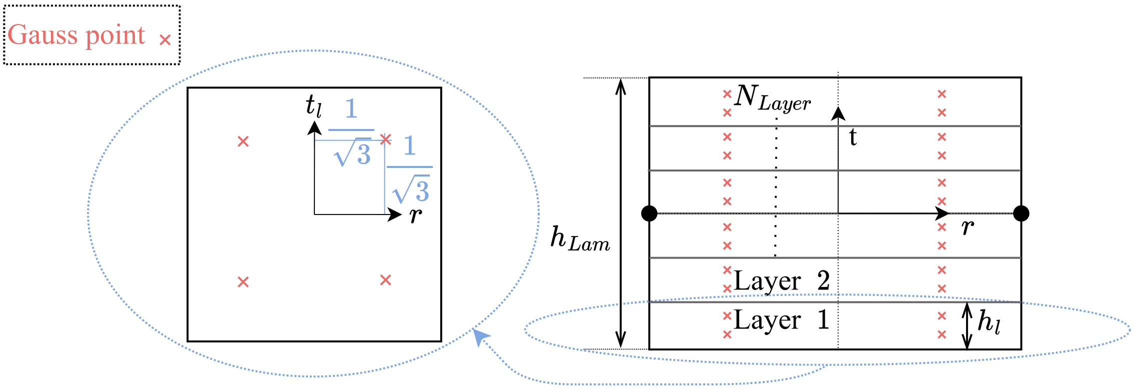

Figure 2.14. Gauss points through the thickness and thickness scaling of each layer using a local layer coordinate t_l

The natural coordinates range from -1 to -1. Therefore, to obtain the contribution of each layer's thickness in the natural coordinate system, the thickness of each layer must be scaled. This scaling is achieved by calculating the thickness t through a layer coordinate t_l using Eq. (2.51).

$$t = \frac{1}{h_{Lam}} \left(2 \sum_{i=1}^{N_{layer}} h_i - h_l(1 - t_l) \right) - 1 \tag{2.51}$$

Here, the total laminate thickness h_{Lam} scales the thickness contribution of each lamina and N_{layer} is the number of layers in the laminate. Another issue that must be addressed is the integration variable, which must be formulated using the layer coordinate t_l to utilise Eq. (2.51). From Figure 2.14, an infinitesimal change in the thickness direction is expressed, and dt_l can be isolated as shown in Eq. (2.52).

$$\frac{dt}{dt_l} = \frac{h_l}{h_{Lam}} \quad \Rightarrow \quad dt = \frac{h_l}{h_{Lam}} dt_l \tag{2.52}$$

Eq. (2.52) is substituted into Eq. (2.48), (2.49) and (2.50) to change the integration variable in the thickness direction. To calculate the volume integral using Gauss integration, a $2 \times 2 \times 2$-Gauss quadrature is used to calculate each block in the element stiffness matrix

$[\mathbf{k}]_e^{block,z}$ as shown in Eq. (2.53) and (2.54)

$$[\mathbf{k}]_e^{block,z} = \sum_{l=1}^{N_{layer}} \sum_{i=1}^{2} \sum_{m=1}^{2} \sum_{k=1}^{2} w_i w_m w_k \, [\boldsymbol{\phi}_{\mathbf{z}}(\mathbf{r},\mathbf{s},\mathbf{t})]_{limk} \, \frac{h_l}{h_{Lam}}, \qquad z = 1,2,3 \tag{2.53}$$

$$r, s, t_l = \pm \frac{1}{\sqrt{3}}, \qquad w_i w_m w_k = 1 \tag{2.54}$$

The element rotational DoFs, denoted by $(\alpha_a, \beta_a, \mu_a), \quad a = 1,..,4$ is defined in the node director coordinate systems. To account for this, when transforming the global equilibrium equation, a transformation matrix $[\mathbf{T_{dG}}]_e$ is required to transform these DoFs from the director systems to the global system. This transformation follows the approach described by Stagsted and Bertelsen (2023), where the rotations in the director system can be transformed into rotations in the global system using Eq. (2.55). This approach is also often referred to as a basis change.

$$\begin{bmatrix} \alpha_a \\ \beta_a \\ \mu_a \end{bmatrix}_{Global} = \underbrace{[\{\mathbf{V_{1a}}\}, \{\mathbf{V_{2a}}\},]}_{[\mathbf{V_{base}}]_a} \begin{bmatrix} \alpha_a \\ \beta_a \end{bmatrix}_{Director} = [\mathbf{V_{base}}]_a \begin{bmatrix} \alpha_a \\ \beta_a \end{bmatrix} \tag{2.55}$$

Eq. (2.55) is valid because the director base vectors $\{\mathbf{V_{1a}}\}$ and $\{\mathbf{V_{2a}}\}$ are defined in the global coordinate system. The contribution from $\{\mathbf{V_{3a}}\}$ is excluded in the director basis matrix $[\mathbf{V_{base}}]_a$ since there is no drilling DoF in the element system.

To restrict the base change to only the rotational DoFs, the equation for the basis of a single node a in Eq. (2.55) is expanded by implementing a 3 × 3 identity matrix, which is denoted by $[\mathbf{I_3}]$. The transformation matrix defined in Eq. (2.56) can be established to transform the rotational DoFs.

$$[\mathbf{T_{dG}}]_e = \begin{bmatrix} [\mathbf{I_3}] & [\mathbf{0}] & [\mathbf{0}] & [\mathbf{0}] & [\mathbf{0}] & [\mathbf{0}] & [\mathbf{0}] & [\mathbf{0}] \\ [\mathbf{0}] & [\mathbf{V_{base}}]_1 & [\mathbf{0}] & [\mathbf{0}] & [\mathbf{0}] & [\mathbf{0}] & [\mathbf{0}] & [\mathbf{0}] \\ [\mathbf{0}] & [\mathbf{0}] & [\mathbf{I_3}] & [\mathbf{0}] & [\mathbf{0}] & [\mathbf{0}] & [\mathbf{0}] & [\mathbf{0}] \\ [\mathbf{0}] & [\mathbf{0}] & [\mathbf{0}] & [\mathbf{V_{base}}]_2 & [\mathbf{0}] & [\mathbf{0}] & [\mathbf{0}] & [\mathbf{0}] \\ [\mathbf{0}] & [\mathbf{0}] & [\mathbf{0}] & [\mathbf{0}] & [\mathbf{I_3}] & [\mathbf{0}] & [\mathbf{0}] & [\mathbf{0}] \\ [\mathbf{0}] & [\mathbf{0}] & [\mathbf{0}] & [\mathbf{0}] & [\mathbf{0}] & [\mathbf{V_{base}}]_3 & [\mathbf{0}] & [\mathbf{0}] \\ [\mathbf{0}] & [\mathbf{0}] & [\mathbf{0}] & [\mathbf{0}] & [\mathbf{0}] & [\mathbf{0}] & [\mathbf{I_3}] & [\mathbf{0}] \\ [\mathbf{0}] & [\mathbf{0}] & [\mathbf{0}] & [\mathbf{0}] & [\mathbf{0}] & [\mathbf{0}] & [\mathbf{0}] & [\mathbf{V_{base}}]_4 \end{bmatrix}_{24 \times 20} \tag{2.56}$$

This transformation from rotational DoFs described in the element system obtains the global equilibrium equation in Eq. (2.57).

$$\underbrace{\sum_{e=1}^{N_e} [\mathbf{L}]_e^T \left([\mathbf{T_{dG}}]_e^T \, [\mathbf{k_T}]_e \, [\mathbf{T_{dG}}]_e \right) [\mathbf{L}]_e}_{[\mathbf{K_T}]} \Delta\{\mathbf{D}\} = \underbrace{-\sum_{e=1}^{N_e} [\mathbf{L}]_e^T \left([\mathbf{T_{dG}}]_e \, \{\mathbf{r}\}_e \right)}_{\{\mathbf{R}\}} \tag{2.57}$$

Here $[\mathbf{K_T}]$ and $[\mathbf{R}]$ are the global tangent stiffness matrix and global residual vector. The inclusion of the sparse bookkeeping matrix $[\mathbf{L}]_e$ in Eq. (4.19) can be regarded more as a mathematical statement than an implementation detail.

2.2.9 Linear 4-node Shell element with EAS and MITC

This subsection explains the differences between the geometrical linear and geometrical non-linear formulations.

A geometrical linear formulation can be achieved by utilising the linear strain tensor and Cauchy's stress tensor in the derivation. As a result, the strain-displacement matrix $[\mathbf{B}]$ only consists of the linear strain-displacement matrix $[\mathbf{B_0}]$. Additionally, the element equilibrium equation only incorporates the external force vector. Therefore, the linear version of Eq. (2.47) is expressed for the geometrical linear formulation as shown in Eq. (2.58).

$$\underbrace{\left([\mathbf{k_{uu}}]_e - [\mathbf{k_{\boldsymbol{\alpha} u}}]_e^T [\mathbf{k_{\boldsymbol{\alpha\alpha}}}]_e^{-1} [\mathbf{k_{\boldsymbol{\alpha} u}}]_e\right)}_{[\mathbf{k_0}]_e} \{\mathbf{d}\}_e = \{\mathbf{f_{ext}}\}_e \tag{2.58}$$

The linear strain displacement matrix $[\mathbf{B_0}]$ is used in Eq. (2.49) and (2.50) to calculate $[\mathbf{k_{\boldsymbol{\alpha} u}}]_e$ and $[\mathbf{k_{\boldsymbol{\alpha\alpha}}}]_e$, while $[\mathbf{k_{uu}}]_e$ is calculated using Eq. (2.59).

$$[\mathbf{k_{uu}}]_e = \int_1^1 \int_1^1 \int_1^1 [\mathbf{B_0}]^T [\mathbf{C^{con}}] [\mathbf{B_0}] |J| \, drdsdt \tag{2.59}$$

Since there is no EAS force vector $\{\mathbf{f_{EAS}}\}_e$ in Eq. (2.58), then $\{\boldsymbol{\alpha}\}_e$ is calculated using Eq. (2.60). A linear analysis can be performed using these changes in formulation.

$$\{\boldsymbol{\alpha}\}_e = -[\mathbf{k_{\boldsymbol{\alpha\alpha}}}]_e^{-1} [\mathbf{k_{\boldsymbol{\alpha} u}}]_e \{\mathbf{d}\}_e \tag{2.60}$$

A comprehensive knowledge of both formulations of laminated fibre-reinforced composites is crucial to ensure accurate and reliable design using the 4-node EAS and MITC shell element. These composites are often prone to buckling, a significant concern that needs to be addressed during the design process. In this regard, buckling analysis and optimisation are essential aspects to be considered. Therefore, the following chapter will cover these topics to help designers develop more efficient and effective designs for laminated fibre-reinforced composites.

3 Discrete Material Optimisation of Laminated Composites

This chapter introduces the parameterisation used for gradient-based optimisation methods of fibre-reinforced laminated composites in this thesis while highlighting the challenges and advantages.

It is widely recognised that selecting the most effective optimisation approach to any given structural problem is a complex task that heavily relies on the specific circumstances of the structural problem. Therefore, no universally applicable strategy can be used across all structural optimisation problems. Instead, a nuanced understanding of the unique characteristics of each problem is essential to identifying the most appropriate approach. Traditionally, optimisation problems of laminated composites are tailored to consider the stacking sequence, lamina angles and lamina thickness while minimising or maximising performance features such as the weight of the structure, buckling behaviour, failure load, deflection, stiffness and fundamental frequency.(Nikbakt et al., 2018)

An important aspect of structural optimisation is manufacturing the optimised design, which can only be achieved through careful consideration of the manufacturing methods in the particular industry. One particularly useful parameterisation in optimising wind turbine blades is the DMO parameterisation proposed by Stegmann and Lund (2005). However, this method is not only limited to wind turbine blades but is preferable for structures where the laminated composite is manufactured using Non-Crimp Fabrics (NCFs), and the lamina angles are limited to discrete values. The different materials in the laminated composite structure are efficiently introduced to the optimisation problem through a multi-material interpolation to calculate the constitutive properties of each element denoted e and layer l as shown in Eq. (3.1).

A density-based approach can represent the presence or absence of a candidate material. The presence or absence of the candidate material can be expressed as a binary value of either 1 or 0. However, formulating the optimisation problem as an integer programming problem can be computationally expensive for problems involving many design variables. To address this issue, the variable x_{elc} is represented as a continuous variable ranging from

0 to 1, as shown in Eq. (3.3), instead of a binary representation.

$$[\mathbf{C}]_{el} = \sum_{c=1}^{N_c} w_c(x_{elc})\,[\mathbf{C}]_c \tag{3.1}$$

$$\sum_{c=1}^{N_c} x_{elc} = 1 \qquad \forall(e,l,c) \tag{3.2}$$

$$x_{elc} \in [0;1] \qquad \forall(e,l,c) \tag{3.3}$$

To drive the multi-material interpolation to a single candidate material, a weight function $w_c(x_{elc})$ is used to penalise intermediate candidate materials.

Two of the most widely used weight functions are the Solid Isotropic Material and Penalisation (SIMP) proposed by Bendsøe (1989) and Rational Approximation of Material Properties (RAMP) introduced by Stolpe and Svanberg (2001). Later Hvejsel and Lund (2011) introduced the multi-material formulation of SIMP and RAMP, which extended the traditional DMO-parameterisation to optimise for discrete candidate materials and topology simultaneously. This is achieved by including a void material in the multi-material interpolation. It is further important to realise that the penalisation of the traditional RAMP and SIMP differs from that of the multi-material formulations. Hvejsel and Lund (2011) introduced Eq. (3.4) to calculate an equivalent multi-material RAMP penalisation $\tilde{p}$ for a number of candidate materials N_c, where p is the traditional SIMP penalisation.

$$\tilde{p} = \frac{\left(\frac{1}{N_c}\right)^{-p} - N_c}{N_c - 1} \tag{3.4}$$

The main advantage of RAMP over traditional SIMP interpolation is that the gradient is non-zero for $x_{elc} = 0$, as shown in Figure 3.1. Alternatively, the SINH-interpolation penalise the constitutive properties and the volume constraint as proposed by Bruns (2005) for topology optimisation.

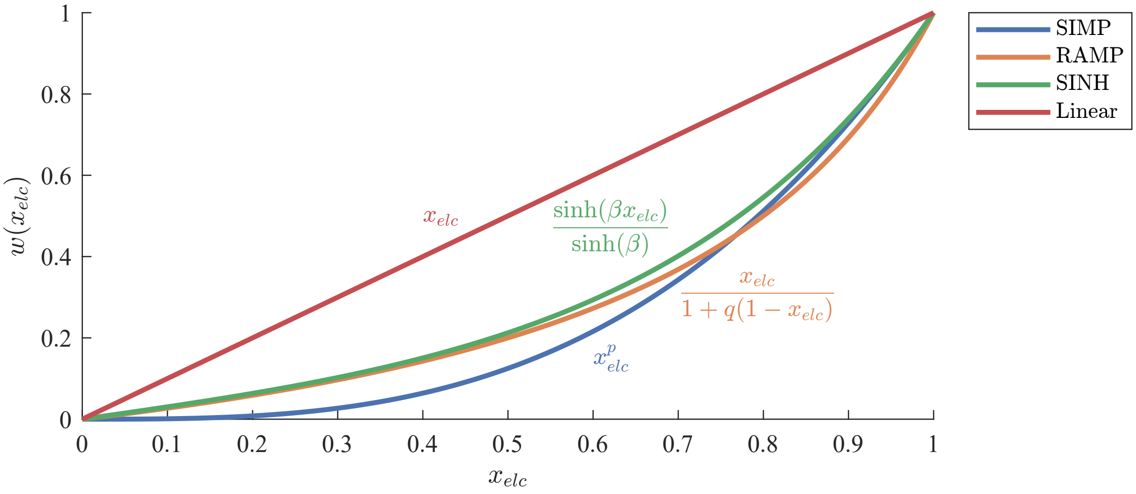

Figure 3.1. Interpolations often used in structural optimisation. Here, all penalisations are set to 3

Selecting appropriate penalisation is crucial for achieving a discrete design and a strong optimum. High penalisation can make the optimisation problem more non-convex, (Labanda and Stolpe, 2015), thereby increasing the risk of obtaining a local optimum. Petersson and Sigmund (1998) suggested that gradually increasing the penalisation, known as a continuation, leads to better-optimised designs. The continuation strategy is widely used, but new research in structural optimisation focuses on the relation between computational performance and penalisation strategies. Labanda and Stolpe (2015) proposed an automatic continuation strategy, where the penalisation is included as a design variable in the optimisation problem.

In structural optimisation, manufacturing methods are often considered to realise optimised designs and to study their effects on the design. The NCFs used for wind turbine blades have a specific minimum width and length. To address this manufacturing constraint in the DMO parameterisation, the blade geometry can be divided into subdomains called patches. This is very efficient since it reduces the number of design variables and introduces no additional constraints. To introduce patches the parameterisation in Eq. (3.1), (3.2) and (3.3) is reformulated as shown in Eq. (3.5), (3.6) and (3.7)

$$[\mathbf{C}]_{el} = \sum_{c=1}^{N_c} w_c(x_{plc})\,[\mathbf{C}]_c \tag{3.5}$$

$$\sum_{c=1}^{N_c} x_{plc} = 1 \qquad \forall(p,l,c) \tag{3.6}$$

$$x_{plc} \in [0;1] \qquad \forall(p,l,c) \tag{3.7}$$

In this thesis, the DMO parameterisation is used for the optimisation problem. It is less computationally demanding and particularly useful for optimising wind turbine blades.

3.1 Stress Based Optimisation

Predicting failure in composites is challenging due to the absence of a universally accepted criterion for failure.(Jones, 1998) In the wind turbine industry, the Puck Failure criterion is widely used. However, using the adaption of the Puck failure criterion is limited in optimisation since a part of the failure criterion involves solving an extremum problem to determine the fracture plane (Puck and Schürmann, 2002; Jakobsen, 2022). Lund (2018) used the maximum strain criterion and maximum stress criterion and a 9-node isoparametric shell element to optimise laminated composite structures. Initial work by Schøn (2023) was conducted to include the maximum strain criterion, maximum stress criterion, and the inverse scaling of Tsai-Wu failure criterion by Groenwold and Haftka (2006) using DMO and the stabilised 4-node shell element.

The Tsai-Wu failure criterion is a generalisation of the Von Mises failure criterion for orthotropic materials. It captures the coupling between dilation and distortion in such materials, which the Von Mises failure criterion fails to account for. Another advantage of the Tsai-Wu failure criterion is its ability to consider the interaction between stress components. This differentiates it from other criteria, such as the maximum strain and maximum stress criteria. However, the Tsai-Wu failure criterion has been criticised since Hart-Smith (1990) called the failure envelope a "meaningless curve drawn by unrelated data points".

Aggregate functions are commonly used to convert the local failure criterion into a global criterion that can be represented as a single function. This can be achieved using, for example, the P-norm aggregate function or the Kreisselmeier-Steinhauser function. However, using the aggregate functions, there is an error between the largest failure value and the aggregated function, which can be minimised by increasing the penalisation, but this increases the non-linearity of the problem. When minimising the p-norm, its accuracy becomes less important compared to when it is employed as a constraint. The adaptive constraint scaling method proposed by Le et al. (2010) addresses this issue and introduces numerical damping into the problem.

In gradient-based topology optimisation with stress constraints, singular optima becomes an issue. This was first observed by Sved and Ginos (1968) for truss structures, where the global optimum could not be attained through gradient optimisation by reducing the cross-section. The issue was later explained by Kirsch (1989, 1990), where conventional gradient-based methods fail to reach the optimal solution due to degenerated subspace of the feasible domain.

The qp-relaxation by Bruggi (2008) is shown as $x_{plc}^{0.5}$ in Figure 3.2 can address this issue. This approach reformulates the problem and makes it more favourable for a candidate material to be either present or not present since its intermediate values have a higher weighting in the failure criteria and do not contribute to stiffness. Lund (2018) utilised RAMP with negative penalisation on the failure index and linear interpolation on the stress field to ensure intermediate densities were unfavourable.

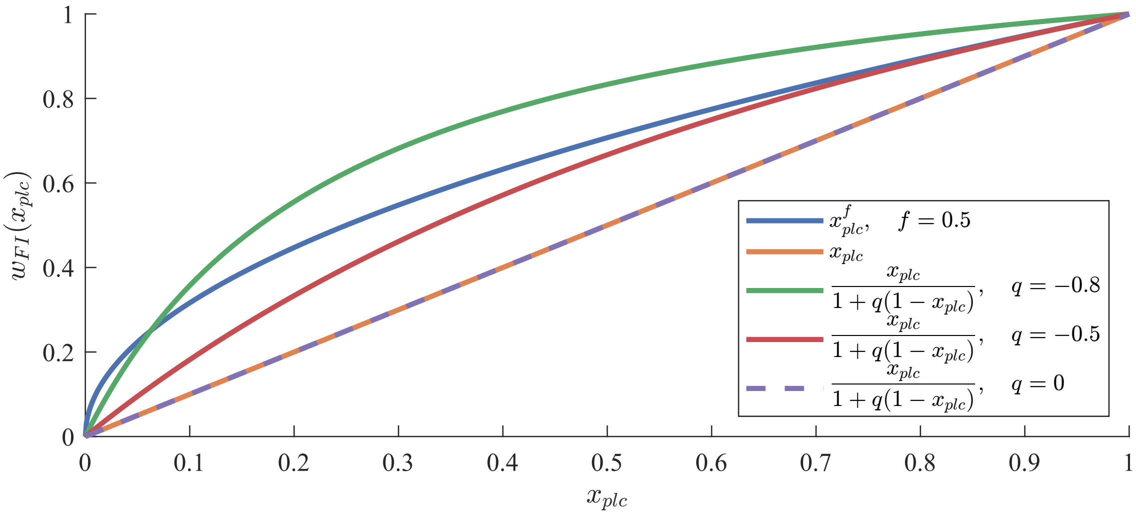

Figure 3.2. Weight functions used in structural optimisation for failure criterion.

These methods can introduce a failure criterion in the optimisation problem, thereby preventing failure of the optimised laminated composites due to static loading. However, other phenomena must be considered to ensure the structural integrity of the optimised design. Laminated composites can be used to design thin-walled structures to obtain low mass. As a result, buckling often becomes a crucial factor in the design of laminated composites. As outlined in Appendix B, several approaches have different limitations to optimise laminated composite structures and avoid structural instabilities.

3.2 Optimisation Method

Appropriate selection of an optimisation method is essential to ensure computational efficiency and a strong minimum. Structural gradient-based optimisation methods such as the Moving Methods of Asymptotes (MMA), Sequential Quadratic Programming (SQP) and Sequential Linear Programming (SLP) have been used to solve various problems. MMA by Svanberg (1987) has been proven to be a powerful approach for addressing non-linear problems and optimisation problems involving many design variables. However, equality constraints can not be introduced directly, and the method becomes inefficient for problems with many constraints (Hua et al., 2022). SLP is computationally attractive for DMO since the parameterisation introduce several linear constraints, as shown in Eq. (3.6). Therefore, this thesis will rely on previous experience with DMO and use the SLP from IBM ILOG CPLEX and Sparse Nonlinear OPTimizer (SNOPT). SLP solves a linearised version of the original nonlinear problem sequentially. Appropriate selection of move limits is crucial for successful optimisation using SLP since the linearisation must approximate the original problem adequately. Sørensen et al. (2014) introduce an adaptive move limit strategy for selecting move limits based on oscillations of the object function.

Feasibility of the linearised problems can be ensured by reformulating the original objective function $\kappa^{(n)}$ using the merit function ψ_0^n as shown in Eq. (3.8).

$$\psi_0^{(n)} = \kappa^{(n)} + a \sum_{k=1}^{K} \left(c y_k^{(n)} + \frac{1}{2} \left(y_k^{(n)} \right)^2 \right) \tag{3.8}$$

Here, n is the iteration number, and K is the total number of non-linear inequality constraints denoted $g_k^{(n)}$. To ensure a well-scaled problem between the objective function and constraints, a must be appropriately selected by letting $a = \kappa^{(1)}$. The positive penalisation factor c prevents the positive slack variables $y_k^{(n)} > 0$ from attaining large values by making them numerically unattractive.

To include the slack variables in the constraints, the reformulated inequality constraints denoted $g_{\psi,k}^{(n)}$ are introduced in Eq. (3.9).

$$g_{\psi,k}^{(n)} = g_k^{(n)} - y_k^{(n)} \leq g_{max}, \qquad k = 1, 2 \cdots, K \tag{3.9}$$

This strategy can be applied to optimise a structural objective function denoted κ^n, but gradient information of the objective function and constraint in Eq. (3.8) and (3.9) must be provided. (Sørensen et al., 2014)

4 Linear Buckling Optimisation

This chapter implements linear buckling optimisation using an EAS and MITC stabilised 4-node shell element since it is less computationally expensive than the non-linear buckling analysis. A linear buckling problem can be formulated from the incremental equilibrium equation in Eq. (2.47) and (2.57), where the tangent stiffness matrix can be reformulated to a linear stiffness matrix $[\mathbf{K_0}]$ and stress stiffening matrix $[\mathbf{K}_{\boldsymbol{\sigma}}]$ as shown in.

$$\left([\mathbf{K_0}] + [\mathbf{K}_{\boldsymbol{\sigma}}]\right) \Delta\{\mathbf{D}\} = \{\mathbf{R}\} \tag{4.1}$$

For the element tangent stiffness matrix in Eq (2.47) the only term that depends on the stress vector is $[\mathbf{k_{uu}}]_e$, which can be observed from Eq. (2.48), (2.49) and (2.50). Therefore only $[\mathbf{k_{uu}}]_e$ must be addressed to reformulate the element tangent stiffness matrix to the linear element stiffness matrix in Eq (4.2) and the element stress stiffening matrix Eq (4.3), where $[\mathbf{k_T}]_e = [\mathbf{k_0}]_e + [\mathbf{k}_{\boldsymbol{\sigma}}]_e$.

$$[\mathbf{k_0}]_e = \int_1^1 \int_1^1 \int_1^1 [\mathbf{B_0}]^T \left[\mathbf{C^{con}}\right] [\mathbf{B_0}] \, |J| \; drdsdt - [\mathbf{k}_{\boldsymbol{\alpha}\mathbf{u}}]_e^T \, [\mathbf{k}_{\boldsymbol{\alpha\alpha}}]_e^{-1} \, [\mathbf{k}_{\boldsymbol{\alpha}\mathbf{u}}]_e \tag{4.2}$$

$$[\mathbf{k}_{\boldsymbol{\sigma}}]_e = \int_1^1 \int_1^1 \int_1^1 \frac{d\,[\mathbf{B}]^T}{d\{\mathbf{d}\}} \{\boldsymbol{\sigma}\} |J| \; drdsdt \tag{4.3}$$

The linear buckling problem assumes small displacements. Thus, the linear strain displacement matrix is used, while the volume integral is evaluated using the same methods from subsection 2.2.8, i.e. thickness scaling and full integration.

To formulate the buckling problem, only in-plane forces are considered as $\lambda\{\mathbf{F_0}\}$, here $\{\mathbf{F_0}\}$ is a reference load and λ load multiplier also called the buckling load factor. The stress stiffening matrix depends on the membrane forces expressed through the constant λ. Therefore, the incremental equilibrium equation of the post-buckled denoted 0 and buckled structure can be expressed using Eq. (4.4) and (4.5). Here, $\{\boldsymbol{\Phi}\}$ denotes the displacement from the post buckled to the buckled configuration.

$$([\mathbf{K_0}] + \lambda\,[\mathbf{K}_{\boldsymbol{\sigma}}])\Delta\{\mathbf{D}\} = \lambda\{\mathbf{F_0}\} \tag{4.4}$$

$$([\mathbf{K_0}] + \lambda\,[\mathbf{K}_{\boldsymbol{\sigma}}])\left(\Delta\{\mathbf{D}\} + \{\boldsymbol{\Phi}\}\right) = \lambda\{\mathbf{F_0}\} \tag{4.5}$$

Eq. (4.4) is subtracted from Eq. (4.5) to obtain the eigenvalue problem in Eq. (4.6). (Cook et al., 2001; Lund and Lindgaard, 2022)

$$\big([\mathbf{K_0}] + \lambda_j\,[\mathbf{K}_{\boldsymbol{\sigma}}]\big)\{\boldsymbol{\Phi}_j\} = \{\mathbf{0}\}, \qquad j = 1, 2, \cdots, N_{EV}, \qquad N_{EV} \leq N_{DoF} \qquad \{\boldsymbol{\Phi}_j\} \neq \{\mathbf{0}\} \tag{4.6}$$

It implies the buckling load λ_j and the corresponding mode shape $\{\mathbf{\Phi}_j\}$ are arranged in ascending order based on the magnitude of the buckling load. Thus, λ_1 represents the lowest buckling load. N_{DoF} is the total number of DOF in the model, and N_{EV} is the desired number of buckling loads to include in the optimisation problem. Due to computational limitations, it is not feasible to introduce all the buckling loads that can be calculated in the model. In this work, N_{EV} is set to 10 to balance the computational efficiency.

4.1 Design Sensitivity Analysis

The sensitivities of λ_j are needed because the buckling load λ_j is incorporated into the problem as a constraint or as part of the objective function. DSA of linear buckling and vibration problems has been conducted multiple times. Therefore, the approach described in the current section aligns with the approach described in Lund (2009) and Sørensen et al. (2014)

Buckling and vibration optimisation problems present challenges in situations where multiple eigenvalues obtain the exact same value. This is often encountered in problems with a large design space and symmetry (Seyranian et al., 1994). It results in non-differentiable eigenvalues but can be addressed as shown by Lund (1994) and Seyranian et al. (1994). In this thesis, only distinct eigenvalues are considered to reduce the complexity of the DSA.

The full derivative of the buckling load factor with respect to (w.r.t) a design variable x_{plc} is calculated using direct differentiation of Eq. (4.6) as shown in Eq. (4.7).

$$\frac{d\left[\mathbf{K_0}\right]}{dx_{plc}}\{\mathbf{\Phi}_j\} + \left(\left[\mathbf{K_0}\right] + \lambda_j \left[\mathbf{K_{\sigma}}\right]\right)\frac{d\{\mathbf{\Phi}_j\}}{dx_{plc}} + \frac{d\lambda_j}{dx_{plc}}\left[\mathbf{K_{\sigma}}\right]\{\mathbf{\Phi}_j\} + \lambda_j\frac{d\left[\mathbf{K_{\sigma}}\right]}{dx_{plc}}\{\mathbf{\Phi}_j\} = \{\mathbf{0}\} \tag{4.7}$$

The full derivative w.r.t a variable x is denoted with $\frac{d}{dx}$, where partial derivatives are denoted $\frac{\partial}{\partial x}$.

Eq. (4.7) is premultiplied with $\{\mathbf{\Phi}_j\}^T$ as shown in Eq. (4.8) to utilise the orthogonality properties of eigenvectors. It is chosen to scale the eigenvector so $\{\mathbf{\Phi}_i\}^T\left[\mathbf{K_{\sigma}}\right]\{\mathbf{\Phi}_j\} = -\delta_{ij}$, which is known as $[\mathbf{K_{\sigma}}]$-orthonormalisation. Since δ_{ij} is Kronecker's delta and $j = i$ then the $[\mathbf{K_{\sigma}}]$-orthonormalisation can be written as $\{\mathbf{\Phi}_j\}^T\left[\mathbf{K_{\sigma}}\right]\{\mathbf{\Phi}_j\} = -1$.

$$\begin{aligned} \{\mathbf{\Phi}_j\}^T\frac{d\left[\mathbf{K_0}\right]}{dx_{plc}}\{\mathbf{\Phi}_j\} + \underbrace{\{\mathbf{\Phi}_j\}^T\left(\left[\mathbf{K_0}\right] + \lambda_j\left[\mathbf{K_{\sigma}}\right]\right)}_{\left(\left[\mathbf{K_0}\right]+\lambda_j\left[\mathbf{K_{\sigma}}\right]\right)\{\mathbf{\Phi}_j\}=\{\mathbf{0}\}}\frac{d\{\mathbf{\Phi}_j\}}{dx_{plc}} + \frac{d\lambda_j}{dx_{plc}}\underbrace{\{\mathbf{\Phi}_j\}^T\left[\mathbf{K_{\sigma}}\right]\{\mathbf{\Phi}_j\}}_{-1} \\ +\lambda_j\{\mathbf{\Phi}_j\}^T\frac{d\left[\mathbf{K_{\sigma}}\right]}{dx_{plc}}\{\mathbf{\Phi}_j\} = \{\mathbf{0}\} \end{aligned} \tag{4.8}$$

$\frac{d\{\mathbf{\Phi}_j\}}{dx_{plc}}$ is eliminated from Eq. (4.8) and $\frac{d\lambda_j}{dx_{plc}}$ is isolated to obtain Eq. (4.9)

$$\frac{d\lambda_j}{dx_{plc}} = \{\mathbf{\Phi}_j\}^T\left(\frac{d\left[\mathbf{K_0}\right]}{dx_{plc}} + \lambda_j\frac{d\left[\mathbf{K_{\sigma}}\right]}{dx_{plc}}\right)\{\mathbf{\Phi}_j\} \tag{4.9}$$

The stiffness matrix is only a function of the design variables $\left[\mathbf{K}\big(\{\mathbf{x}\}\big)\right]$, therefore $\frac{d[\mathbf{K_0}]}{dx_{plc}}$ is the same as the partial derivative $\frac{\partial[\mathbf{K_0}]}{\partial x_{plc}}$.

$\frac{d[\mathbf{K}_{\boldsymbol{\sigma}}]}{dx_{plc}}$ is often calculated using a finite difference approximation since it is an implicit function of the displacements $\left[\mathbf{K}_{\boldsymbol{\sigma}}\left(\{\mathbf{D}\}(\{\mathbf{x}\}),\{\mathbf{x}\}\right)\right]$ and it makes it more complicated to determine the analytical expression. Finite difference approximation is computationally expensive because it requires perturbation on each design variable. Direct differentiation of $[\mathbf{K}_{\boldsymbol{\sigma}}]$ yields Eq. (4.10).

$$\frac{d\left[\mathbf{K}_{\boldsymbol{\sigma}}\right]}{dx_{plc}} = \frac{\partial\left[\mathbf{K}_{\boldsymbol{\sigma}}\right]}{\partial x_{plc}} + \frac{\partial\left[\mathbf{K}_{\boldsymbol{\sigma}}\right]}{\partial\{\mathbf{D}\}}\frac{d\{\mathbf{D}\}}{dx_{plc}} \tag{4.10}$$

Similarly, applying direct differentiation of $\{\boldsymbol{\Phi}_j\}^T\frac{d[\mathbf{K}_{\boldsymbol{\sigma}}]}{dx_{plc}}\{\boldsymbol{\Phi}_j\}$, leads to Eq. (4.11).

$$\{\boldsymbol{\Phi}_j\}^T\frac{d\left[\mathbf{K}_{\boldsymbol{\sigma}}\right]}{dx_{plc}}\{\boldsymbol{\Phi}_j\} = \{\boldsymbol{\Phi}_j\}^T\left(\frac{\partial\left[\mathbf{K}_{\boldsymbol{\sigma}}\right]}{\partial x_{plc}} + \frac{\partial\left[\mathbf{K}_{\boldsymbol{\sigma}}\right]}{\partial\{\mathbf{D}\}}\frac{d\{\mathbf{D}\}}{dx_{plc}}\right)\{\boldsymbol{\Phi}_j\} \tag{4.11}$$

$\frac{d\{\mathbf{D}\}}{dx_{plc}}$ is computationally expensive for problems with many design variables but can be eliminated from the total derivative. This is achieved by solving an additional system of linear algebraic equations (adjoint equation) for each eigenvalue.

The derivative of the state variable can be calculated by direct differentiation of the linear global equilibrium equation $[\mathbf{K_0}]\{\mathbf{D}\} = \{\mathbf{F_{ext}}\}$ as shown in Eq. (4.12).

$$\frac{d\left[\mathbf{K_0}\right]}{dx_{plc}}\{\mathbf{D}\} + \left[\mathbf{K_0}\right]\frac{d\{\mathbf{D}\}}{dx_{plc}} = \frac{d\{\mathbf{F_{ext}}\}}{dx_{plc}} \quad\Rightarrow\quad \frac{d\{\mathbf{D}\}}{dx_{plc}} = \left[\mathbf{K_0}\right]^{-1}\left(\frac{d\{\mathbf{F_{ext}}\}}{dx_{plc}} - \frac{d\left[\mathbf{K_0}\right]}{dx_{plc}}\{\mathbf{D}\}\right) \tag{4.12}$$

It is assumed the forces are independent of the design variables, thus $\frac{d\{\mathbf{F_{ext}}\}}{dx_{plc}} = \{\mathbf{0}\}$. This applies to problems without volume forces and situations where the forces are applied on a fixed boundary, preventing material removal. Consequently Eq. (4.11) can be written as shown in Eq. (4.13), where $\frac{d[\mathbf{K_0}]}{dx_{plc}}$ in Eq. (4.12) is equal to the partial derivative.

$$\{\boldsymbol{\Phi}_j\}^T\frac{d\left[\mathbf{K}_{\boldsymbol{\sigma}}\right]}{dx_{plc}}\{\boldsymbol{\Phi}_j\} = \{\boldsymbol{\Phi}_j\}^T\left(\frac{\partial\left[\mathbf{K}_{\boldsymbol{\sigma}}\right]}{\partial x_{plc}} - \frac{\partial\left[\mathbf{K}_{\boldsymbol{\sigma}}\right]}{\partial\{\mathbf{D}\}}\left[\mathbf{K_0}\right]^{-1}\frac{\partial\left[\mathbf{K_0}\right]}{\partial x_{plc}}\{\mathbf{D}\}\right)\{\boldsymbol{\Phi}_j\} \tag{4.13}$$

Calculating the inverse of $[\mathbf{K_0}]$ is computationally expensive, therefore an adjoint vector $\{\boldsymbol{\Lambda}\}$ is introduced in Eq. (4.14)

$$\{\boldsymbol{\Lambda}\}^T = \{\boldsymbol{\Phi}_j\}^T\left[\mathbf{K_0}\right]^{-1}\frac{\partial\left[\mathbf{K}_{\boldsymbol{\sigma}}\right]}{\partial\{\mathbf{D}\}}\{\boldsymbol{\Phi}_j\} \tag{4.14}$$

This is an advantage since it is more computationally expensive to invert the matrix than determine the solution to the linear system of equations in Eq. (4.15), where $[\mathbf{K_0}] = [\mathbf{K_0}]^T$ due to symmetry of the linear global stiffness matrix.

$$\{\boldsymbol{\Lambda}\}^T\left[\mathbf{K_0}\right] = \{\boldsymbol{\Phi}_j\}^T\frac{\partial\left[\mathbf{K}_{\boldsymbol{\sigma}}\right]}{\partial\{\mathbf{D}\}}\{\boldsymbol{\Phi}_j\}, \quad \text{Symmetry:} \ \Rightarrow \quad \left[\mathbf{K_0}\right]\{\boldsymbol{\Lambda}\} = \left(\{\boldsymbol{\Phi}_j\}^T\frac{\partial\left[\mathbf{K}_{\boldsymbol{\sigma}}\right]}{\partial\{\mathbf{D}\}}\{\boldsymbol{\Phi}_j\}\right)^T \tag{4.15}$$

Inserting the adjoint vector into Eq. (4.13) yields Eq. (4.16).

$$\{\boldsymbol{\Phi}_j\}^T\frac{d\left[\mathbf{K}_{\boldsymbol{\sigma}}\right]}{dx_{plc}}\{\boldsymbol{\Phi}_j\} = \{\boldsymbol{\Phi}_j\}^T\frac{\partial\left[\mathbf{K}_{\boldsymbol{\sigma}}\right]}{\partial x_{plc}}\{\boldsymbol{\Phi}_j\} - \{\boldsymbol{\Lambda}\}^T\frac{\partial\left[\mathbf{K_0}\right]}{\partial x_{plc}}\{\mathbf{D}\} \tag{4.16}$$

The computationally expensive derivative $\frac{d\{\mathbf{D}\}}{dx_{plc}}$ is thereby eliminated from the total derivative by solving Eq. (4.15) and inserting $\{\mathbf{\Lambda}\}^T$ into (4.17)

$$\frac{d\lambda_j}{dx_{plc}} = \{\mathbf{\Phi}_j\}^T \frac{\partial \left[\mathbf{K_0}\right]}{\partial x_{plc}} \{\mathbf{\Phi}_j\} + \lambda_j \left(\{\mathbf{\Phi}_j\}^T \frac{\partial \left[\mathbf{K}_{\boldsymbol{\sigma}}\right]}{\partial x_{plc}} \{\mathbf{\Phi}_j\} - \{\mathbf{\Lambda}\}^T \frac{\partial \left[\mathbf{K_0}\right]}{\partial x_{plc}} \{\mathbf{D}\} \right) \tag{4.17}$$

This approach is very computationally efficient as $\frac{\partial[\mathbf{K_0}]}{\partial x_{plc}}$ and $\frac{\partial[\mathbf{K}_{\boldsymbol{\sigma}}]}{\partial x_{plc}}$ are computationally inexpensive to calculate and the factorised $[\mathbf{K_0}]$ can be reused from the analysis.

4.1.1 Partial derivative of the stress stiffening matrix w.r.t $\{\mathbf{D}\}$

To determine the adjoint vector in Eq. (4.15), it is necessary to calculate the partial derivative of the stress stiffening matrix w.r.t $\{\mathbf{D}\}$ and the product with the eigenvector $\{\mathbf{\Phi}_j\}$. This calculation can be evaluated on the element level as shown in Eq. (4.18).

$$\left(\{\mathbf{\Phi}_j\}^T \frac{\partial \left[\mathbf{K}_{\boldsymbol{\sigma}}\right]}{\partial \{\mathbf{D}\}} \{\mathbf{\Phi}_j\} \right)^T = \left(\sum_{e=1}^{N_e} \left[\mathbf{L}\right]_e \left[\mathbf{T^{(dG)}}\right]_e \{\mathbf{\Phi}_j\}_e^T \frac{\partial \left[\mathbf{k}_{\boldsymbol{\sigma}}\right]_e}{\partial \{\mathbf{d}\}_e} \{\mathbf{\Phi}_j\}_e \right)^T \tag{4.18}$$

To calculate $\frac{\partial[\mathbf{k}_{\boldsymbol{\sigma}}]_e}{\partial\{\mathbf{d}\}_e}$ it is important to realise $\frac{d[\mathbf{B}]^T_{limk}}{d\{\mathbf{d}\}_e}$ in Eq. (4.3) is independent of $\{\mathbf{d}\}$. Therefore, it is only necessary to calculate the partial derivative of the stress vector in each Gauss point and layer $\{\boldsymbol{\sigma}\}_{limk}$ as shown in Eq. (4.19)

$$\begin{aligned} \{\mathbf{\Phi}_j\}_e^T \frac{\partial \left[\mathbf{k}_{\boldsymbol{\sigma}}\right]_e}{\partial \{\mathbf{d}\}_e} \{\mathbf{\Phi}_j\}_e = & \sum_{l=1}^{N_{layer}} \sum_{i=1}^{2} \sum_{m=1}^{2} \sum_{k=1}^{2} w_i w_m w_k \{\mathbf{\Phi}_j\}_e^T \left(\frac{d\left[\mathbf{B}\right]^T_{limk}}{d\{\mathbf{d}\}_e} \frac{\partial \{\boldsymbol{\sigma}\}_{limk}}{\partial \{\mathbf{d}\}_e} \right) \\ & |J|_{limk} \frac{h_l}{h_{Lam}} \{\mathbf{\Phi}_j\}_e, \quad \text{Where:} \quad w_i = w_m = w_k = 1 \end{aligned} \tag{4.19}$$

It is important to recognise in chapter 2 that the stress vector can be calculated using Eq. (4.20) since it consists of $\left[\mathbf{C^{Con}}\right]_{limk}$ and the sum of the compatible strain and independent strain field shown in Eq. (2.34), while the internal DoF is removed using static condensation in Eq. (2.60).

$$\{\boldsymbol{\sigma}\}_{limk} = \left[\mathbf{C^{Con}}\right]_{limk} \left(\left[\mathbf{B_0}\right]_{limk} \{\mathbf{d}\}_e - \left[\bar{\mathbf{M}}\right]_{limk} \left[\mathbf{k}_{\boldsymbol{\alpha\alpha}}\right]_e^{-1} \left[\mathbf{k}_{\boldsymbol{\alpha}\mathbf{u}}\right]_e \{\mathbf{d}\}_e \right) \Big) \tag{4.20}$$

Partial differentiation of Eq. (4.20) result in Eq. (4.21)

$$\frac{\partial \{\boldsymbol{\sigma}\}_{limk}}{\partial \{\mathbf{d}\}_e} = \left[\mathbf{C^{Con}}\right]_{limk} \left(\left[\mathbf{B_0}\right]_{limk} - \left[\bar{\mathbf{M}}\right]_{limk} \left[\mathbf{k}_{\boldsymbol{\alpha\alpha}}\right]_e^{-1} \left[\mathbf{k}_{\boldsymbol{\alpha}\mathbf{u}}\right]_e \right) \Big) \tag{4.21}$$

The $\left[\mathbf{k}_{\boldsymbol{\alpha\alpha}}\right]_e^{-1} \left[\mathbf{k}_{\boldsymbol{\alpha}\mathbf{u}}\right]_e$ term can be calculated efficiently by determining $[\mathbf{x}]$ in $\left[\mathbf{k}_{\boldsymbol{\alpha\alpha}}\right]_e [\mathbf{x}] = \left[\mathbf{k}_{\boldsymbol{\alpha}\mathbf{u}}\right]_e$. The equation can be solved efficiently using Cholesky decomposition with highly optimised Basic Linear Algebra Subprograms (BLAS-routines).

The $\left[\mathbf{C^{Con}}\right]_{limk}$ is calculated using the same approach as shown in Eq. (2.29) for an orthotropic material, but must include the DMO parameterisation. The constitutive properties of the candidate material are defined in material coordinates, where $\left[\mathbf{C_{12}}\right]_c$ is transformed to the element system using an in-plane transformation matrix $\left[\mathbf{T}_{\boldsymbol{\theta}}\right]_c$ in

Eq. (2.25). Subsequently, the constitutive properties are transformed to the contravariant components at each Gauss point using $[\mathbf{T_{con}}]_{limk}$ as shown in Eq. (4.22).

$$\left[\mathbf{C^{Con}}\right]_{limk} = [\mathbf{T_{con}}]_{limk}^T \sum_{c=1}^{N_c} \left([\mathbf{T}_{\boldsymbol{\theta}}]_c^T \, w_c(x_{plc}) \, [\mathbf{C_{12}}]_c \, [\mathbf{T}_{\boldsymbol{\theta}}]_c \right) [\mathbf{T_{con}}]_{limk} \tag{4.22}$$

$\left(\{\boldsymbol{\Phi}_j\}^T \frac{\partial[\mathbf{K}_{\boldsymbol{\sigma}}]}{\partial\{\mathbf{D}\}}\{\boldsymbol{\Phi}_j\}\right)^T$ is calculated in the same loop since this will lead to $DoF \times N_{EV}$ matrix, where N_{EV} indicates the number of eigenvectors and buckling loads considered in the optimisation problem. This is mathematically permissible since $\frac{\partial[\mathbf{k}_{\boldsymbol{\sigma}}]_e}{\partial d_{DoF}}$ can be determined using Eq. (4.23), here d_{DoF} represents a single DoF in $\{\mathbf{d}\}_e$.

$$\begin{aligned} \frac{\partial\left[\mathbf{k}_{\boldsymbol{\sigma}}\right]_e}{\partial d_{DoF}} = \left[\mathbf{T^{(dG)}}\right]_e \sum_{l=1}^{N_{layer}} \sum_{i=1}^{2} \sum_{m=1}^{2} \sum_{k=1}^{2} w_i w_m w_k & \left(\left(\frac{d\left[\mathbf{B}\right]^T}{d\{\mathbf{d}\}} \right)_{limk} [\mathbf{C_{Con}}]_{limk} \left([\mathbf{B_0}]_{limk} \right.\right. \\ & \left.\left. \{\mathbf{I_{DoF}}\}_e - \left[\bar{\mathbf{M}}\right]_{limk} \left[\mathbf{k}_{\boldsymbol{\alpha\alpha}}\right]_e^{-1} \left[\mathbf{k}_{\boldsymbol{\alpha}\mathbf{u}}\right]_e \{\mathbf{I_{DoF}}\}_e \right) \right) |J|_{limk} \frac{h_l}{h} \end{aligned} \tag{4.23}$$

Consequently, $\{\mathbf{I_{DoF}}\}_e$ is a vector with zero values in all its components except for the one that corresponds to d_{DoF} in $\frac{\partial\{\mathbf{d}\}_e}{\partial d_{DoF}}$. This process can be effectively performed in MUST through loops over each DoF, equivalent to extracting the components related to the specific degree of freedom. Hence, there is no requirement to store and carry out multiplication with a $N_{DoF} \times N_{DoF} \times N_{DoF}$-array, which requires a significant memory allocation compared to a 2-dimensional array.

4.1.2 Partial derivative of the linear stiffness matrix w.r.t x_{plc}

The derivative of the global linear stiffness matrix w.r.t the design variables in Eq. (4.24) must be calculated to obtain the total derivative.

$$\frac{\partial\left[\mathbf{K_0}\right]}{\partial x_{plc}} = \sum_{e=1}^{N_e} [\mathbf{L}]_e \left[\mathbf{T^{(dG)}}\right]_e^T \frac{\partial\left[\mathbf{k_0}\right]_e}{\partial x_{plc}} \left[\mathbf{T^{(dG)}}\right]_e \tag{4.24}$$

The partial derivative of the linear element stiffness matrix w.r.t x_{plc} can be calculated by partial differentiation of the element stiffness in Eq. (2.58) as shown in Eq. (4.25). (Stagsted and Bertelsen, 2023)

$$\begin{aligned} \frac{\partial\left[\mathbf{k_0}\right]_e}{\partial x_{plc}} = & \frac{\partial\left[\mathbf{k_{uu}}\right]_e}{\partial x_{plc}} - \frac{\partial\left[\mathbf{k}_{\boldsymbol{\alpha}\mathbf{u}}\right]^T}{\partial x_{plc}} \left[\mathbf{k}_{\boldsymbol{\alpha\alpha}}\right]_e^{-1} \left[\mathbf{k}_{\boldsymbol{\alpha}\mathbf{u}}\right]_e + \left[\mathbf{k}_{\boldsymbol{\alpha}\mathbf{u}}\right]^T \left[\mathbf{k}_{\boldsymbol{\alpha\alpha}}\right]_e^{-1} \frac{\partial\left[\mathbf{k}_{\boldsymbol{\alpha\alpha}}\right]_e}{\partial x_{plc}} \left[\mathbf{k}_{\boldsymbol{\alpha\alpha}}\right]_e^{-1} \\ & \left[\mathbf{k}_{\boldsymbol{\alpha}\mathbf{u}}\right]_e - \left[\mathbf{k}_{\boldsymbol{\alpha}\mathbf{u}}\right]^T \left[\mathbf{k}_{\boldsymbol{\alpha\alpha}}\right]_e^{-1} \frac{\partial\left[\mathbf{k}_{\boldsymbol{\alpha}\mathbf{u}}\right]_e}{\partial x_{plc}} \end{aligned} \tag{4.25}$$

The DMO parameterisation uses the weight function $w_c\big(x_{plc}\big)$ in Eq. (3.5), to parameterise the constitutive properties for each candidate material. This means that only the constitutive properties are dependent on x_{plc} and the partial differentiation of Eq. (2.42), (2.43), (2.44) and (2.59) yields Eq. (4.26), (4.27), (4.28), and (4.29).

$$\frac{\partial [\mathbf{k}_{\boldsymbol{\alpha\alpha}}]}{\partial x_{plc}} = \sum_{l=1}^{N_{layer}} \sum_{i=1}^{2}\sum_{m=1}^{2}\sum_{k=1}^{2} w_i w_m w_k [\tilde{\mathbf{M}}]_{limk}^T \frac{\partial [\mathbf{C}^{\mathbf{con}}]_{limk}}{\partial x_{plc}} [\tilde{\mathbf{M}}]_{limk} \frac{1}{|J|_{limk}} \frac{h_l}{h_{Lam}} \tag{4.26}$$

$$\frac{\partial [\mathbf{k}_{\mathbf{uu}}]}{\partial x_{plc}} = \sum_{l=1}^{N_{layer}} \sum_{i=1}^{2}\sum_{m=1}^{2}\sum_{k=1}^{2} w_i w_m w_k \, [\mathbf{B_0}]_{limk}^T \, \frac{\partial [\mathbf{C}^{\mathbf{con}}]_{limk}}{\partial x_{plc}} \, [\mathbf{B_0}]_{limk} \, |J| \frac{h_l}{h_{Lam}} \tag{4.27}$$

$$\frac{\partial [\mathbf{k}_{\boldsymbol{\alpha}\mathbf{u}}]}{\partial x_{plc}} = \sum_{l=1}^{N_{layer}} \sum_{i=1}^{2}\sum_{m=1}^{2}\sum_{k=1}^{2} w_i w_m w_k [\tilde{\mathbf{M}}]_{limk}^T \frac{\partial [\mathbf{C}^{\mathbf{con}}]_{limk}}{\partial x_{plc}} \, [\mathbf{B_0}]_{limk} \, \frac{h_l}{h_{Lam}} \tag{4.28}$$

$$\frac{\partial [\mathbf{k}_{\boldsymbol{\alpha}\mathbf{u}}]^T}{\partial x_{plc}} = \sum_{l=1}^{N_{layer}} \sum_{i=1}^{2}\sum_{m=1}^{2}\sum_{k=1}^{2} w_i w_m w_k \, [\mathbf{B_0}]_{limk}^T \, \frac{\partial [\mathbf{C}^{\mathbf{con}}]_{limk}}{\partial x_{plc}} [\tilde{\mathbf{M}}]_{limk} \frac{h_l}{h_{Lam}} \tag{4.29}$$

$\frac{\partial [\mathbf{C}^{\mathbf{Con}}]_{limk}}{\partial x_{plc}}$ is calculated by the partial derivative of Eq. (4.22) using Eq. (4.30).

$$\frac{\partial \left[\mathbf{C}^{\mathbf{Con}}\right]_{limk}}{\partial x_{plc}} = [\mathbf{T_{con}}]_{limk}^T \sum_{c=1}^{N_c} \left([\mathbf{T}_{\boldsymbol{\theta}}]_c^T \, \frac{\partial w_c(x_{plc})}{\partial x_{plc}} \, [\mathbf{C_{12}}]_c \, [\mathbf{T}_{\boldsymbol{\theta}}]_c \right) [\mathbf{T_{con}}]_{limk} \tag{4.30}$$

The thesis uses RAMP by Stolpe and Svanberg (2001). Accordingly, the derivative is calculated using Eq. (4.31).

$$\frac{\partial w_c(x_{plc})}{\partial x_{plc}} = \frac{1+q}{(1+q(1-x_{plc}))^2} \tag{4.31}$$

4.1.3 Partial derivative of Stress stiffening matrix

$\frac{\partial [\mathbf{K}_{\boldsymbol{\sigma}}]}{\partial x_{plc}}$ can be calculated on element level as shown in Eq. (4.32).

$$\frac{\partial [\mathbf{K}_{\boldsymbol{\sigma}}]}{\partial x_{plc}} = \sum_{e=1}^{N_e} [\mathbf{L}]_e \left[\mathbf{T}^{(\mathbf{dG})}\right]_e^T \frac{\partial [\mathbf{k}_{\boldsymbol{\sigma}}]_e}{\partial x_{plc}} \left[\mathbf{T}^{(\mathbf{dG})}\right]_e \tag{4.32}$$

The stress vector is the only part of the element stress stiffening matrix in Eq (4.3) which depends explicitly on the design variables. Therefore $\frac{\partial [\mathbf{k}_{\boldsymbol{\sigma}}]_e}{\partial x_{plc}}$ is calculated using Eq. (4.33).

$$\frac{\partial [\mathbf{k}_{\boldsymbol{\sigma}}]_e}{\partial x_{plc}} = \sum_{l=1}^{N_{layer}} \sum_{i=1}^{2}\sum_{m=1}^{2}\sum_{k=1}^{2} w_i w_m w_k \left(\frac{d\,[\mathbf{B}]^T}{d\{\mathbf{d}\}_e} \right)_{limk} \frac{\partial \{\boldsymbol{\sigma}\}_{limk}}{\partial x_{plc}} |J|_{limk} \frac{h_l}{h_{Lam}} \tag{4.33}$$

In Eq. (4.20) it is only the constitutive properties that depends explicitly on x_{plc}, thus $\frac{\partial \{\boldsymbol{\sigma}\}_{limk}}{\partial x_{plc}}$ is calculated as shown in Eq. (4.34), where $\frac{\partial [\mathbf{C}^{\mathbf{Con}}]_{limk}}{\partial x_{plc}}$ is calculated using Eq. (4.30).

$$\frac{\partial \{\boldsymbol{\sigma}\}_{limk}}{\partial x_{plc}} = \frac{\partial \left[\mathbf{C}^{\mathbf{Con}}\right]_{limk}}{\partial x_{plc}} \Big([\mathbf{B_0}]_{limk} \, \{\mathbf{d}\}_e - \left[\bar{\mathbf{M}}\right]_{limk} [\mathbf{k}_{\boldsymbol{\alpha\alpha}}]_e^{-1} \, [\mathbf{k}_{\boldsymbol{\alpha}\mathbf{u}}]_e \, \{\mathbf{d}\}_e \Big) \Big) \tag{4.34}$$

4.2 Benchmark Examples

Validating the sensitivities is a step-wise process in which complexity is added to each step. Therefore, this section utilises three benchmark examples to validate the analytical DSA and compare the implementation to a 9-node isoparametric shell formulation and an 8-node solid shell formulation with EAS and ANS stabilisation.

4.2.1 Single layered cantilever beam

The first benchmark example is shown in Figure 4.1. The benchmark example is utilised since it only consists of a single layer with no curvature to reduce the complexity, and it is possible to benchmark the implementation against a 9-node isoparametric shell formulation and an 8-node solid shell formulation with EAS and ANS stabilisation.

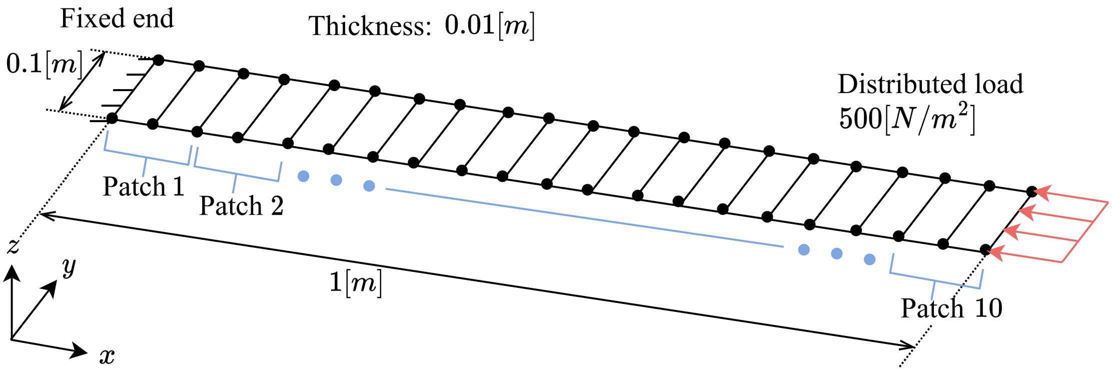

Figure 4.1. Cantilever beam modelled using 20 stabilised 4-node shell elements and 500 N/m pressure load at the end.

The bound formulation by Bendsøe and Olhoff (1985); Olhoff (1989) shown in Eq. (4.35a) is particularly useful to maximise the buckling load factors. Maximisation of the bound variable β avoids certain buckling load factors increasing while decreasing other buckling load factors.

$$\underset{\{\mathbf{x}\},\beta}{\text{Maximise}} \quad \beta \tag{4.35a}$$

$$\text{Subjected to} \quad \lambda_j \geq \beta, \qquad j = 1, \cdots, 10 \tag{4.35b}$$

$$\sum_{c=1}^{N_c} x_{plc} = 1 \qquad \forall(p,l,c) \tag{4.35c}$$

$$x_{plc} \in [0;1] \qquad \forall(p,l,c) \tag{4.35d}$$

The material properties of glass/epoxy in Table 4.1 are used to formulate 12 candidate materials with lamina angle of $0, \pm15, \pm30, \pm45, \pm60, \pm75, 90$. The penalisation factor in RAMP is based on a continuation approach, where the penalty factors gradually increase each 2^{nd} iteration with +5 from $1, 1, 6, 6, 11, 11, \cdots, 151, 151, 156, 156$. The highest penalisation is calculated using Eq. (3.4), where the single phase SIMP penalisation is set to 3, which results in a multi-material RAMP penalisation of 156 (Hvejsel and Lund, 2011). Different penalisation for $[\mathbf{k_0}]_e$ and $[\mathbf{k}_\sigma]_e$ can be applied, however the same penalisations for $[\mathbf{k_0}]_e$ and $[\mathbf{k}_\sigma]_e$ is used in this thesis. In this work x_{plc} is initialised by $\frac{1}{N_c}$ $\forall(p,l,c)$ and the merit function penalisation factor c is set to 100.

Table 4.1. Material data used for the benchmark examples

Constant	**Unit**	**Glass/epoxy**
E_1	[MPa]	$3.8 \cdot 10^4$
E_2	[MPa]	$9.0 \cdot 10^3$
E_3	[MPa]	$9.0 \cdot 10^3$
ν_{12}	$[-]$	0.3
ν_{13}	$[-]$	0.3
ν_{23}	$[-]$	0.3
G_{12}	[MPa]	$3.6 \cdot 10^3$
G_{23}	[MPa]	$3.6 \cdot 10^3$
G_{13}	[MPa]	$3.5 \cdot 10^3$
ρ	$[kg/m^3]$	1870.0

The analytical sensitivities are validated using the absolute error between the approximated sensitivities using forward difference and the analytical sensitivities. The absolute error decreases linearly as expected until it becomes numerically unstable, as shown in Figure 4.2. (Martins and Ning, 2021) However, the absolute error increases at different perturbation sizes. The same is observed for a 9-node isoparametric shell element formulation and a stabilised solid shell element formulation. Further, the error is larger than expected but can be explained by the approach used to solve the linear buckling problem. Here, the subspace iteration method initially proposed by Bathe and Wilson (1973) for frequency problems is utilised. This method is a computationally efficient and robust approach to solve large eigenvalue problems (Bathe, 2013). Appendix C study the influence of the subspace convergence tolerance on the sensitivities. It is observed the absolute error when the convergence tolerance is decreased can be drastically reduced for smaller perturbation sizes.

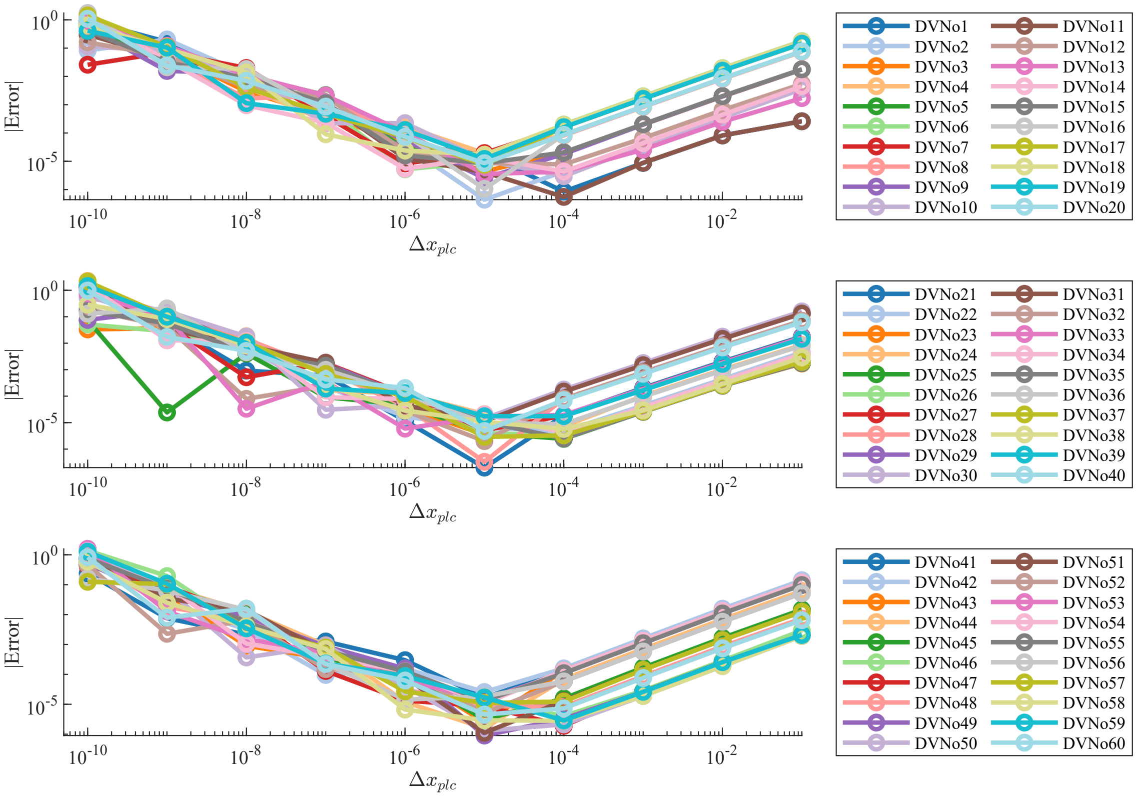

Figure 4.2. Absolute error between the finite difference approximation and the analytical expression for $\frac{d\lambda_1}{dx_{plc}}$ in the single-layered cantilever beam benchmark example

To measure the convergence, it is convenient to use the candidate non-discreteness M_{cnd} in Eq. (4.36), introduced by Sørensen et al. (2014). Here V_{el} is the volume of the layer l in element e. The candidate non-discreteness $M_{cnd} = 0\%$ if all the design variables are either 0 or 1 and $M_{cnd} = 100\%$ when all the design variables are equal to $\frac{1}{N_c}$.

$$M_{cnd} = \frac{\sum_{e=1}^{N_e} \sum_{l=1}^{N_{layer}} V_{el} \Pi_{c=1}^{N_c} \left(\frac{1 - x_{plc}}{1 - \frac{1}{N_c}} \right)^2}{\sum_{e=1}^{N_e} \sum_{l=1}^{N_{layer}} V_{el}} \cdot 100\% \tag{4.36}$$

Figure 4.3 shows the convergence of m_{cnd} and β for the stabilised 4-node shell element, 9-node isoparametric shell and the stabilised solid shell formulation have the same convergence behaviour and results in a fully converged solution, where all x_{plc} are either 1 or 0. The optimised results in all patches are 0°, meaning all fibres are aligned with the load direction.

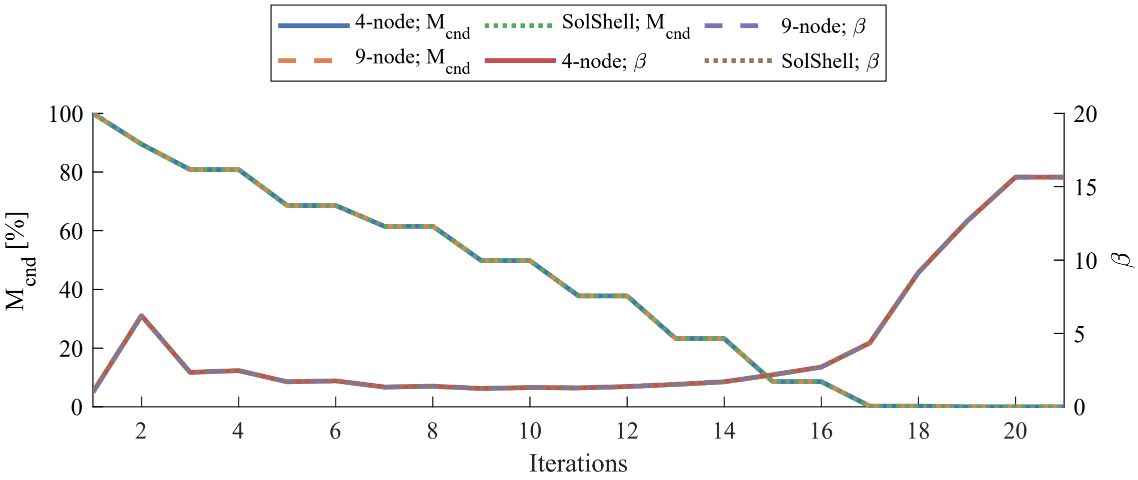

Figure 4.3. Convergence of the cantilever beam

The time to calculate the analytical sensitivities and assemble the stiffness matrix in Figure 4.4 demonstrates that the stabilised 4-node shell element is less computationally expensive than the 9-node isoparametric shell element. Further, it shows similar computational performance to the 8-node solid shell formulation with EAS and ANS stabilisation. The differences in the back substitution times are limited compared to those observed for the sensitivity calculations and assembly time. In this example a Direct Sparse Solver (DSS) is utilised and back substitution is performed when the global equilibrium equation and the adjoint problem is solved.

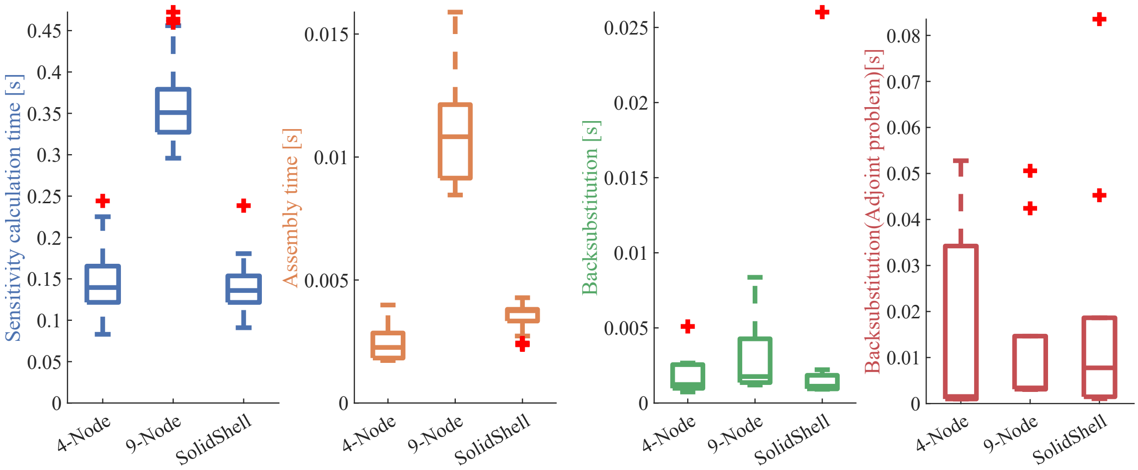

Figure 4.4. Time comparison of the time to perform sensitivity analysis assemble the stiffness matrix and DSS solver back substitutions using the different elements. In the DSS back substitution (GE) denotes the global equilibrium equation and (AP) adjoint problem.

4.2.2 Single Curved shell

A single curved shell structure with four layers illustrated in Figure 4.5 is used to validate the sensitivities and compare the performance of the stabilised 4-node element and the 9-node isoparametric shell element. This benchmark example is selected since it adds complexity with more layers and has a large radius of curvature, as illustrated in Figure 4.5b to ensure the transformations are carried out correctly. Furthermore, the computational time to perform the finite difference approximations is feasible as the model consists of only 10×10 elements. In this example, the penalisation for $w_c(x_{plc})$ is increased with 1 in each iteration $1, 2, 3, \cdots, 156$.

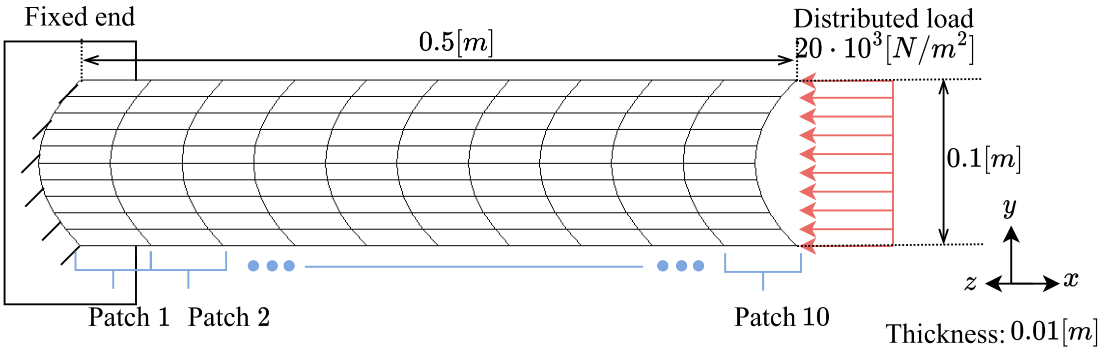

(a) The dimensions and the 10×10 domain is divided into 10 patches

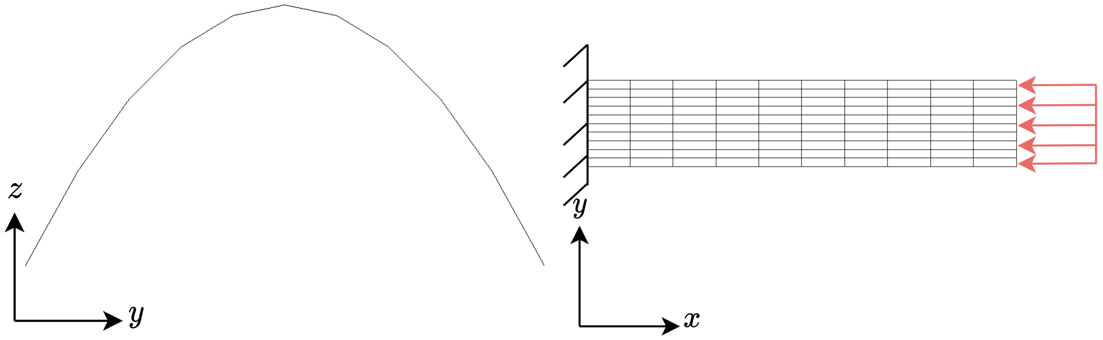

(b) The curved shell from yz plane ***(c)*** The curved shell from xy plane

Figure 4.5. The curved shell has 4 layers created by elevating the midpoint 0.05m along the width. In the fixed end, translations and rotations are fixed

The analytical sensitivities are validated using the absolute error between the approximated sensitivities using forward difference and the analytical sensitivities in Figure 4.6. The absolute error curves show similar behaviour as addressed in subsection 4.2.1.

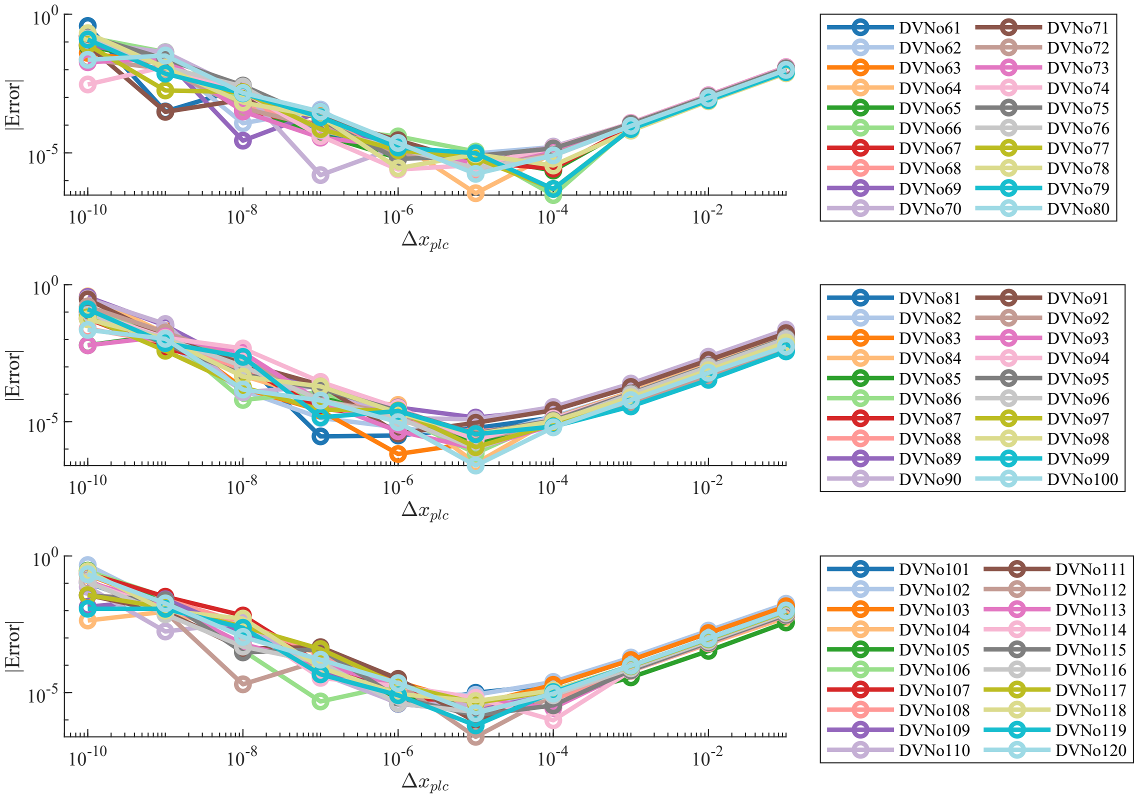

Figure 4.6. Absolute error between the finite difference approximation and the analytical expression for $\frac{d\lambda_1}{dx_{plc}}$ in the single curved shell structure

Figure 4.7 shows the stabilised 4-node shell element sensitivity calculation time and assembly time of the stiffness matrix is more than three times faster than the 9-node isoparametric shell element. The difference in the back substitution times is increased compared to the differences observed in the cantilever beam benchmark example.

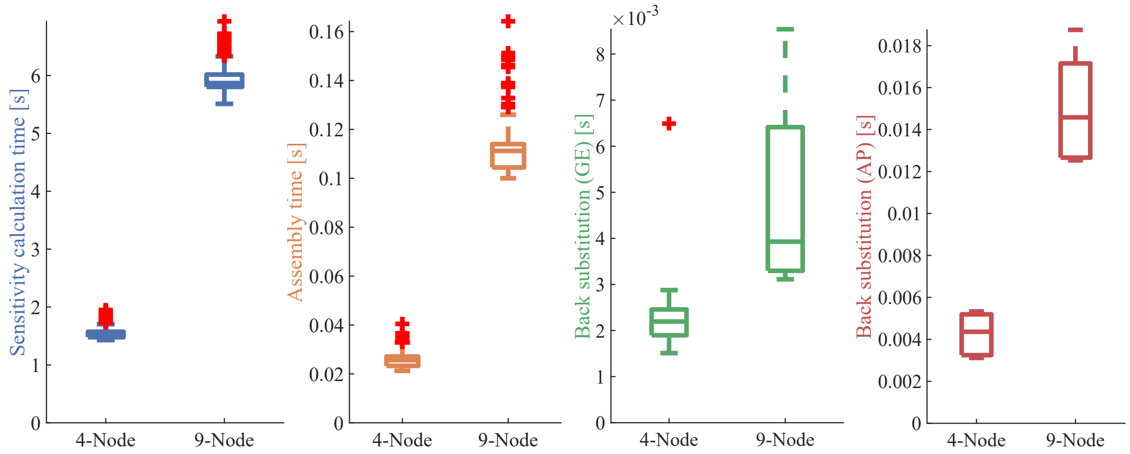

Figure 4.7. Time comparison of the time to perform sensitivity analysis assemble the stiffness matrix and DSS solver back substitutions using the different elements. In the DSS back substitution (GE) denotes the global equilibrium equation and (AP) adjoint problem.

The stabilised 4-node shell element and the 9-node isoparametric shell element show the exact same convergence of the objective function and m_{cnd} as shown in Figure 4.8. The same applies to the results obtained from the convergence of the normalised buckling load factors. Therefore, 4.9 only shows the normalised buckling load factors using the stabilised 4-node shell element. Here, all the buckling load factors are maximised, with the first buckling load factor showing a greater increase than the others.

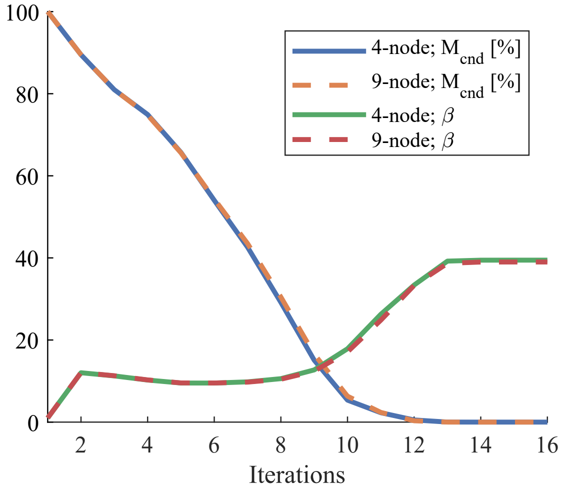

Figure 4.8. Convergence of the single curved shell model

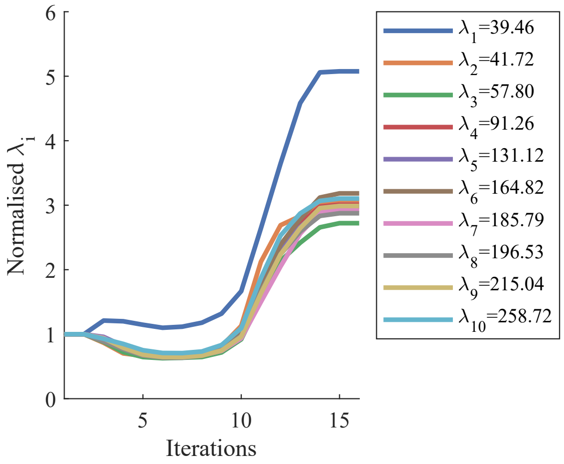

Figure 4.9. Convergence of each normalised buckling load factor. The buckling load factors are normalised with the values in the first iteration.

The optimised results in Figure 4.10 show unexpectedly different layups in the area close to the load introduction. This was further investigated by applying different merit function penalisation and continuation strategies to the stiffness penalisation. They converged to different solutions, which demonstrates the non-convexity of the problem.

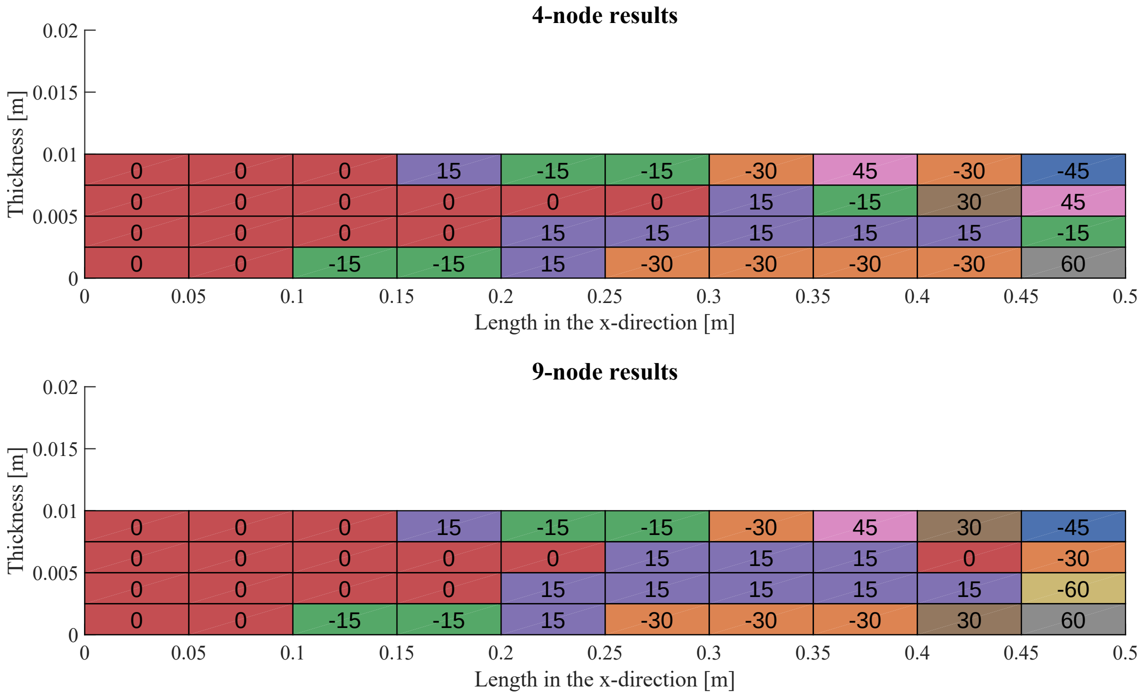

4-node results

0	0	0	15	-15	-15	-30	45	-30	-45
0	0	0	0	0	0	15	-15	30	45
0	0	0	0	15	15	15	15	15	-15
0	0	-15	-15	15	-30	-30	-30	-30	60

9-node results

0	0	0	15	-15	-15	-30	45	30	-45
0	0	0	0	0	15	15	15	0	-30
0	0	0	0	15	15	15	15	15	-60
0	0	-15	-15	15	-30	-30	-30	30	60

Figure 4.10. The optimised design and the layer angle in degrees

4.2.3 Spar cap

A simplified spar cap model in Figure 4.11 is used as a benchmark example. It is selected to test the computational performance when the stabilised 4-node shell element and the 9-node isoparametric shell element are used on a larger problem than the previous two benchmark examples. Additionally, the load and geometry create a symmetry plane in the xz-plane, and it is expected that the optimised design will yield a similar symmetric solution. The optimisation problem is formulated by dividing the elements into 6 equal-sized patches along the width. An isotropic core material is introduced with the material properties shown in Table 4.2. Increasing the number of design variables per patch also increases the stiffness penalisation to 182 by using Eq. (3.4). In this example, the penalisation is increased with 1 in each iteration $1, 2, 3, \cdots, 182$.

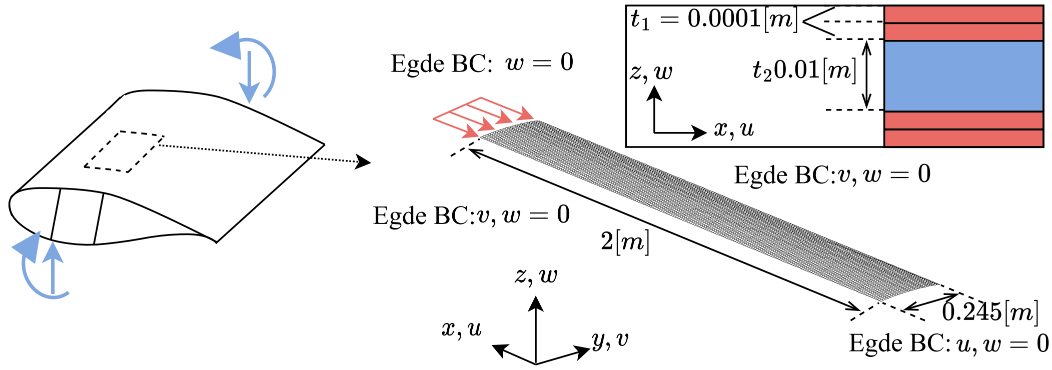

Figure 4.11. Simplified spar cap model inspired by Kühlmeier (2006); Lund (2009), with a radius of curvature on 0.987m. This model consists of 4 1mm glass/epoxy layers (illustrated as the red layer) and a 100mm isotropic foam core (illustrated as the blue layer). The model consists of 24 elements in width and 200 elements in the length direction with a $1 \cdot 10^5 \mathrm{N/m^2}$ pressure load.

Table 4.2. Material data used in the benchmark example

Constant	**Unit**	**Divinycell H130 (isotropic foam)**
E_1	[MPa]	180
ν_{12}	[−]	0.29
G_{12}	[MPa]	7
ρ	[kg/m^3]	1100

The computational performance in Figure 4.12 shows that the calculation time of the 9-node isoparametric shell element's sensitivities and the assembly time is nearly four times larger than the stabilised shell element, while back substitution times are four and five times larger.

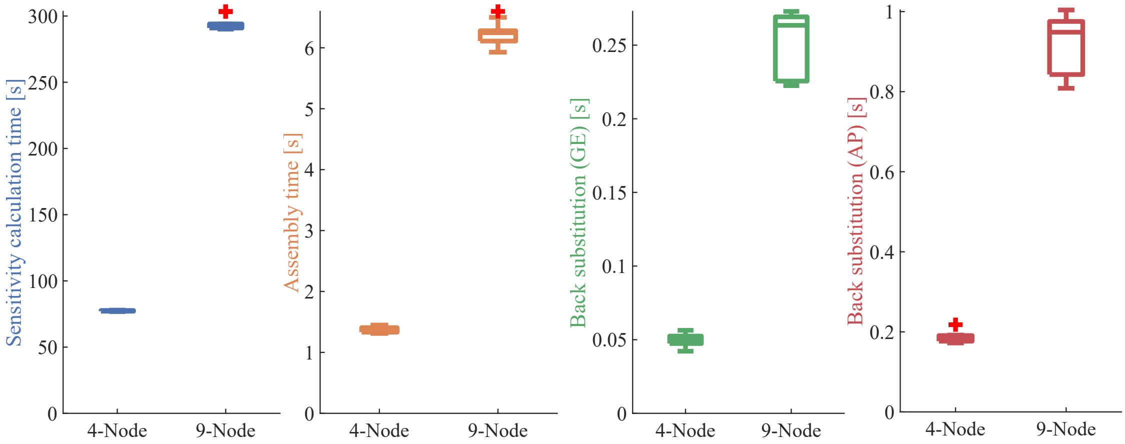

Figure 4.12. Time comparison of the time to perform sensitivity analysis assemble the stiffness matrix and DSS solver back substitutions using the different elements. The DSS back substitution (GE) denotes the global equilibrium equation and (AP) adjoint problem.

The convergence of the objective function in Figure 4.13 exhibits a desirable behaviour where β increases and m_{cnd} decreases without oscillations. The result is completely discrete, so all design variables are either 1 or 0. The convergence of the normalised buckling load factors,β and m_{cnd} are nearly the same. Therefore, Figure 4.14 only shows the buckling load factors for the stabilised 4-node shell element.

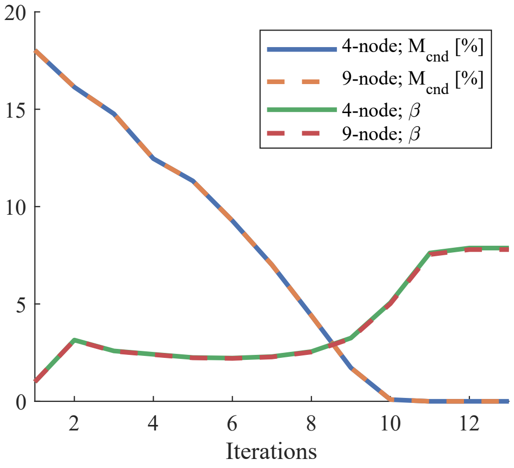

Figure 4.13. Convergence of the spar cap benchmark example.

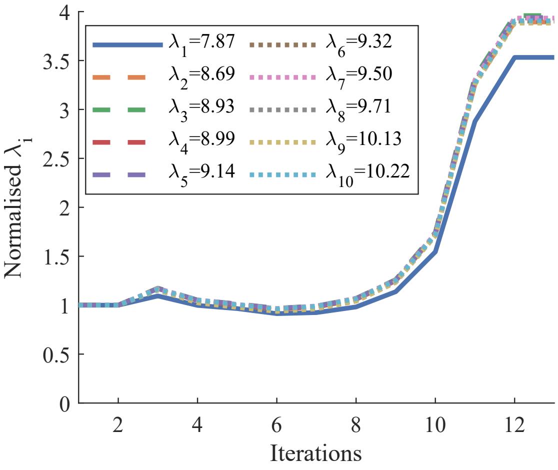

Figure 4.14. Convergence of each normalised buckling load factor. The buckling load factors are normalised with the values in the first iteration.

The optimised design is shown in Figure 4.15 and the corresponding buckling modes in Figure 4.17. As expected, the optimised design exhibits symmetry around the symmetry line in Figure 4.16.

The buckling load factors are numerically close to each other as seen in Figure 4.14. It can be observed that the buckling loads close to each other indicate similar buckling modes as shown in Figure 4.17. This is particularly evident for $\lambda_3 \rightleftharpoons \lambda_4$, $\lambda_5 \rightleftharpoons \lambda_6$, and $\lambda_8 \rightleftharpoons \lambda_9$. Here, $\rightleftharpoons$ indicates that the buckling modes before and after the symbol show similar behaviour and the buckling load factors are close. The optimised design is not suitable for real-world applications because the various fibre angles do not contribute to a tolerant design against static failure or global stiffness. This is especially noticeable in the fourth layer, where the 90°-layer does not contribute to the overall stiffness or strength against static failure.

In the benchmark examples, the buckling load factors are maximised with a fast convergence rate to a fully discrete solution.

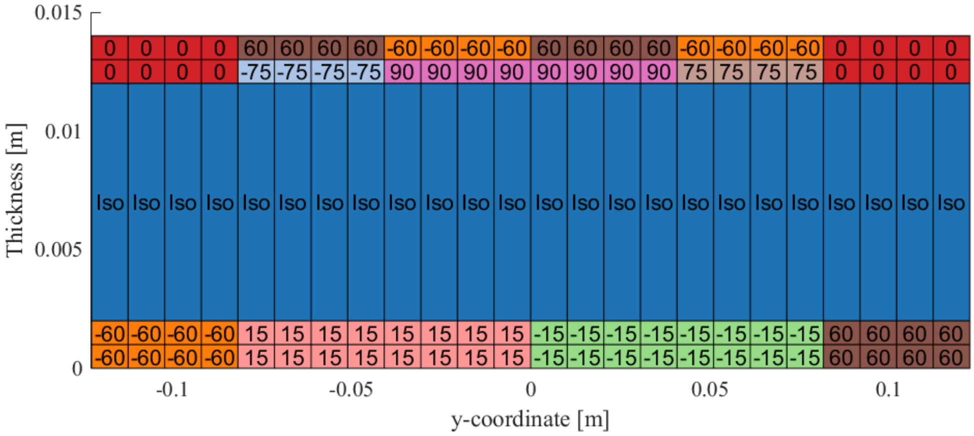

Figure 4.15. The optimised design with the layer angle in degrees.

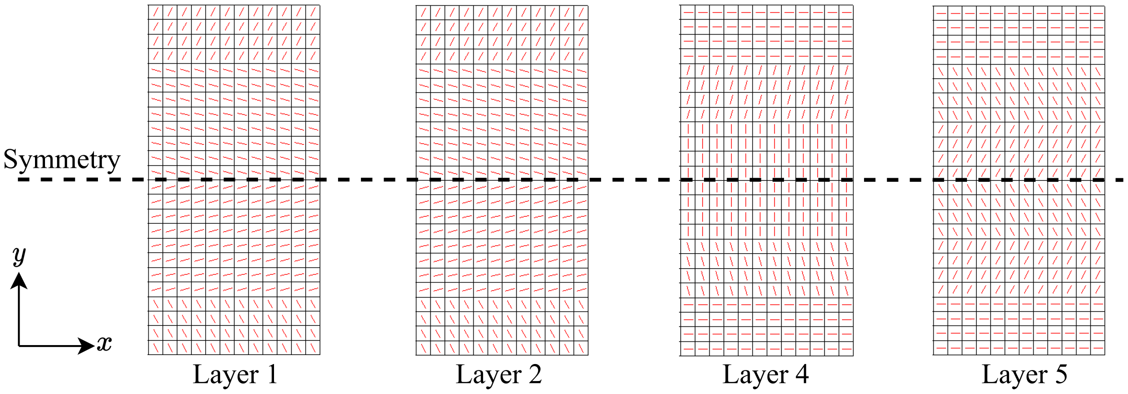

Figure 4.16. A subset of the geometry to show the optimised layer angle in the xy-plane.

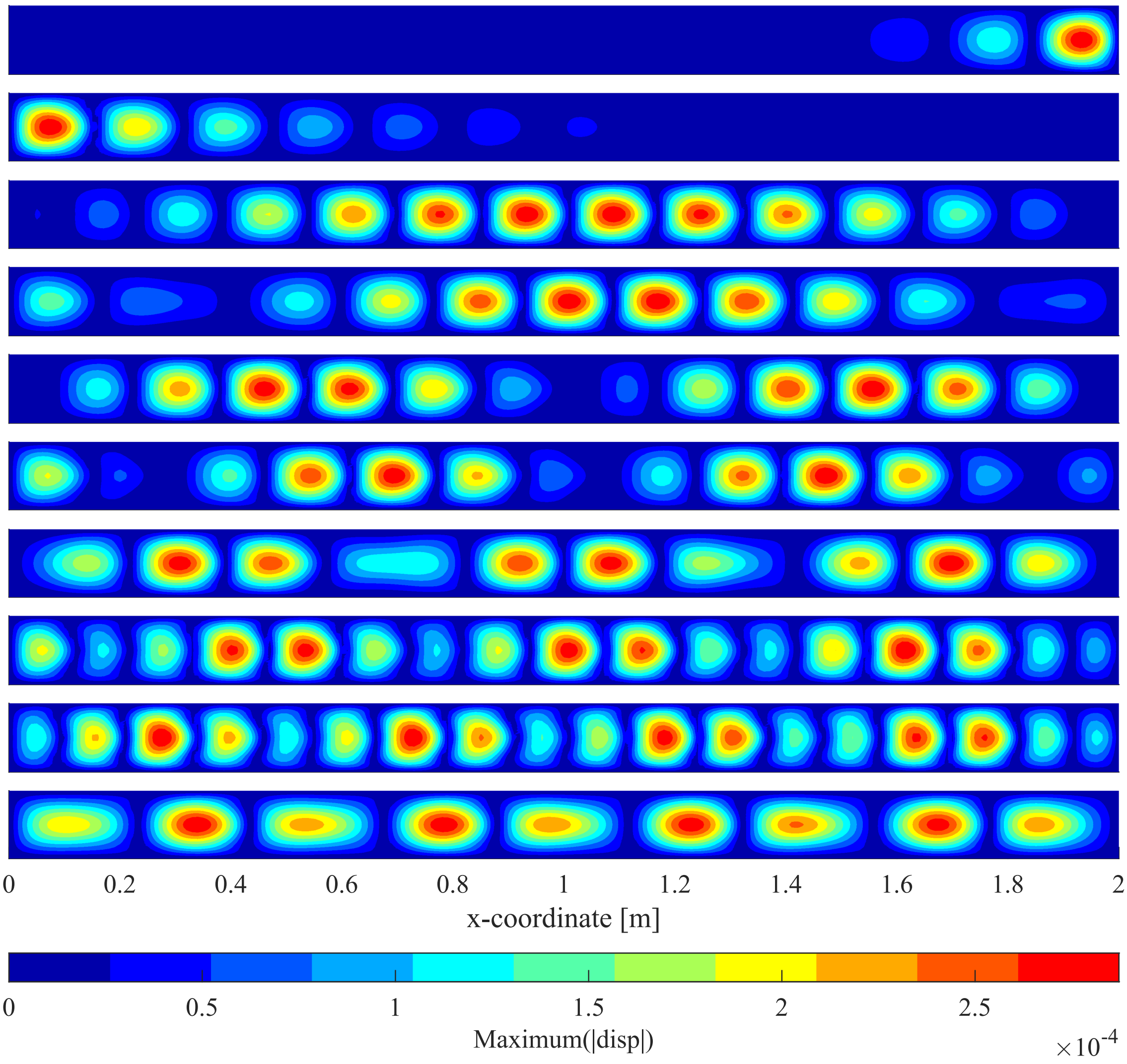

Figure 4.17. The buckling modes for the optimised design, in descending order. $\{\mathbf{\Phi}_1\}$ is in the top and $\{\mathbf{\Phi}_{10}\}$ in the bottom.

5 Static Failure Optimisation

This chapter derives and validates the sensitivities for the maximum strain, maximum stress, and Tsai-Wu failure criteria. Schøn (2023) derived the sensitivities for the EAS and MITC stabilised 4-node shell element and tested the implementation on flat shells and SIMP. This chapter extends the work to be used using RAMP and includes an additional weight function to the stress field. A benchmark example demonstrates its application.

5.1 Strain and Stress Post-Processing

The most accurate covariant strains are evaluated at the super convergent Gauss Points. The EAS formulation causes the element to behave similarly to a 9-node isoparametric shell element. Consequently, the most accurate covariant strains are calculated in the $2 \times 2 \times 2$ Gauss points, as they are considered the super convergent Gauss Points of a non-distorted 9-node isoparametric shell element. To accurately capture the linear variation of covariant normal strains caused by bending moment, it is necessary to perform post-processing of the strains at the top ($m = 2$) and bottom ($m = 1$) of each lamina as shown in Figure 5.1 for a single layer.

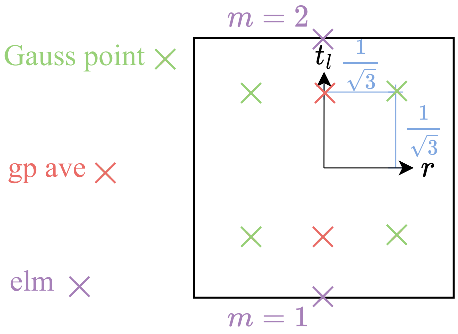

Figure 5.1. Post processing of the covariant strains from the Gauss points of each element e, layer l and top or bottom value m

The covariant strain in each Gauss point is transformed to the element system using $[\mathbf{T^{con}}]_{el}^{(gp)}$ as shown in Eq. (5.1).

$$[\mathbf{T^{con}}]_{el}^{(gp)} \{\boldsymbol{\varepsilon}_{\mathbf{cov}}\}_{elm}^{(gp)} = \{\boldsymbol{\varepsilon}_{\mathbf{d}}\}_{elm}^{(gp)} \tag{5.1}$$

The average strain vector at $t_l = \pm\frac{1}{\sqrt{3}}$ denoted $\{\boldsymbol{\varepsilon}_{\mathbf{d}}\}_{elm}^{(gp,ave)}$ is calculated using the strain vector in the Gauss points $\{\boldsymbol{\varepsilon}_{\mathbf{d}}\}_{elm}^{(gp)}$ and Eq. (5.2).

$$\{\boldsymbol{\varepsilon}_{\mathbf{d}}\}_{elm}^{(gp,ave)} = \frac{1}{4}\sum_{gp=1}^{4}\{\boldsymbol{\varepsilon}_{\mathbf{d}}\}_{elm}^{(gp)} \tag{5.2}$$

The strain vector in the bottom and top of a layer in the laminate can be calculated by extrapolation of $\{\boldsymbol{\varepsilon}_{\mathbf{d}}\}_{elm}^{(gp,ave)}$ as shown in Eqs. (5.3) and (5.4).

$$\{\boldsymbol{\varepsilon}_{\mathbf{d}}\}_{el1} = \frac{1}{2}(1-\sqrt{3})\{\boldsymbol{\varepsilon}_{\mathbf{d}}\}_{el1}^{(gp,ave)} + \frac{1}{2}(1+\sqrt{3})\{\boldsymbol{\varepsilon}_{\mathbf{d}}\}_{el2}^{(gp,ave)} \tag{5.3}$$

$$\{\boldsymbol{\varepsilon}_{\mathbf{d}}\}_{el2} = \frac{1}{2}(1+\sqrt{3})\{\boldsymbol{\varepsilon}_{\mathbf{d}}\}_{el1}^{(gp,ave)} + \frac{1}{2}(1-\sqrt{3})\{\boldsymbol{\varepsilon}_{\mathbf{d}}\}_{el2}^{(gp,ave)} \tag{5.4}$$

The post-processed strain vector $\{\boldsymbol{\varepsilon}_{\mathbf{d}}\}_{elm}$ and the constitutive properties in the element coordinate system are used to calculate the post-processed stress vector $\{\boldsymbol{\sigma}_{\mathbf{d}}\}_{elm}$ in Appendix D and E.

5.2 Maximum Strain Criterion

To apply the maximum strain criterion, it is necessary to transform $\{\boldsymbol{\varepsilon}_{\mathbf{d}}\}_{elm}$ to the material coordinate system as shown in Eq. (5.5).

$$[\mathbf{T}_{\boldsymbol{\theta}}]_c\{\boldsymbol{\varepsilon}_{\mathbf{d}}\}_{elm} = \{\boldsymbol{\varepsilon}_{\mathbf{12}}\}_{elmc} \tag{5.5}$$

Here $[\mathbf{T}_{\boldsymbol{\theta}}]_c$ is defined in Eq. (2.25), where θ is determined by the corresponding candidate material.

The strains in the material coordinate system $\{\boldsymbol{\varepsilon}_{\mathbf{12}}\}_{elmc}$ are used to calculate the failure index $FI^{(p)}$ using the maximum strain criterion as shown in Eqs. (5.6), (5.7) and (5.8), where failure occur when $FI^{(p)} = 1$.

$$-e_{1c} \geq \varepsilon_1 \geq e_{1t} \quad \Rightarrow \frac{\varepsilon_1}{e_{1x}} = FI^{(p1)} \tag{5.6}$$

$$-e_{2c} \geq \varepsilon_2 \geq e_{2t} \quad \Rightarrow \frac{\varepsilon_2}{e_{2x}} = FI^{(p2)} \tag{5.7}$$

$$\frac{|\varepsilon_{12}|}{e_{12}} = FI^{(p12)}, \quad \frac{|\varepsilon_{13}|}{e_{13}} = FI^{(p13)}, \quad \frac{|\varepsilon_{23}|}{e_{23}} = FI^{(p23)} \tag{5.8}$$

Here e_{1c} and e_{1t} are the failure strain in compression and tension in the material 1-direction. Similarly, e_{2c} and e_{2t} are the failure strain in compression and tension in the material 2-direction, while e_{12}, e_{23} and e_{13} are shear failure strain values. Index x denote the corresponding failure strain value determined by the sign of components $\{\boldsymbol{\varepsilon}_{\mathbf{12}}\}_{elmc}$.

For each candidate material, a failure index FI_{elmc} is calculated as the maximum value of the potential failure index $FI_{elmc} = max\Big(FI_{elmc}^{(p1)}, FI_{elmc}^{(p2)}, FI_{elmc}^{(p12)}, FI_{elmc}^{(p13)}, FI_{elmc}^{(p23)}\Big)$.

The failure criterion is introduced into the optimisation problem using the same approach as Lund (2018). A weight function, denoted as $w_{FI}(x_{plc})$ penalise intermediate x_{plc} to calculate an effective failure index $FI_{elm}^{(eff)}$ as shown in Eq. (5.9).

$$FI_{elm}^{(eff)} = \sum_{c=1}^{N_c} w_{FI}(x_{plc})FI_{elmc} \tag{5.9}$$

The P-norm aggregate function in Eq. (5.10) converts the failure criterion to a single function as described in section 3.1.

$$f_{pn} = \left(\sum_{e=1}^{N_e} \sum_{l=1}^{N_{layer}} \sum_{m=1}^{2} \left(FI_{elm}^{(eff)} \right)^P \right)^{\frac{1}{P}} \tag{5.10}$$

The aggregate function converges to the maximum value of $FI_{elm}^{(eff)}$ as P approaches infinity. However, a higher penalisation factor makes the problem increasingly non-linear, which can cause numerical problems. Eq. (5.10) can be introduced as the objective function or a constraint.

5.2.1 Design Sensitivity Analysis

The adjoint method is preferable since the failure criterion is described as a single function with more design variables. Here, an additional equation is used to eliminate the computationally expensive $\frac{d\{\mathbf{D}\}}{dx_{plc}}$.

This is achieved by establishing the augmented Lagrange function in Eq. (5.11).

$$\tilde{f}_{pn}\big(\{\mathbf{D}\}(\{\mathbf{x}\}), \{\mathbf{x}\}\big) = f_{pn}\big(\{\mathbf{D}\}(\{\mathbf{x}\}), \{\mathbf{x}\}\big) - \{\mathbf{\Lambda}\}^T \big([\mathbf{K_0}]\{\mathbf{D}\} - \{\mathbf{F_{ext}}\}\big) \tag{5.11}$$

The Lagrange multiplier vector $\{\mathbf{\Lambda}\}$ can be freely chosen as the extra term has no contribution.

The chain rule is applied to determine the derivative of the augmented Lagrange function as shown in Eq. (5.12).

$$\begin{aligned} \frac{d\tilde{f}_{pn}}{dx_{plc}} =& \frac{\partial f_{pn}}{\partial\{\mathbf{D}\}} \frac{d\{\mathbf{D}\}}{dx_{plc}} + \frac{\partial f_{pn}}{\partial x_{plc}} - \{\mathbf{\Lambda}\}^T \bigg(\frac{\partial}{\partial\{\mathbf{D}\}} \big([\mathbf{K_0}]\{\mathbf{D}\} - \{\mathbf{F_{ext}}\}\big) \frac{d\{\mathbf{D}\}}{dx_{plc}} + \frac{\partial}{\partial x_{plc}} \big([\mathbf{K_0}]\{\mathbf{D}\} \\ &- \{\mathbf{F_{ext}}\}\big)\bigg) - \frac{d\{\mathbf{\Lambda}\}^T}{dx_{plc}} \underbrace{\big([\mathbf{K_0}]\{\mathbf{D}\} - \{\mathbf{F_{ext}}\}\big)}_{=0} \end{aligned} \tag{5.12}$$

In this thesis, the forces are assumed to be independent of the design variables. Therefore Eq. (5.12) reduces to Eq. (5.13).

$$\frac{d\tilde{f}_{pn}}{dx_{plc}} = \frac{\partial f_{pn}}{\partial\{\mathbf{D}\}} \frac{d\{\mathbf{D}\}}{dx_{plc}} + \frac{\partial f_{pn}}{\partial x_{plc}} - \{\mathbf{\Lambda}\}^T \left([\mathbf{K_0}] \frac{\partial\{\mathbf{D}\}}{\partial\{\mathbf{D}\}} \frac{d\{\mathbf{D}\}}{dx_{plc}} + \frac{\partial [\mathbf{K_0}]}{\partial x_{plc}} \{\mathbf{D}\} \right) \tag{5.13}$$

Eq. (5.13) is re-expressed in Eq. (5.14) using factorisation of $\frac{d\{\mathbf{D}\}}{dx_{plc}}$.

$$\frac{d\tilde{f}_{pn}}{dx_{plc}} = \left(\frac{\partial f_{pn}}{\partial\{\mathbf{D}\}} - \{\mathbf{\Lambda}\}^T [\mathbf{K_0}] \right) \frac{d\{\mathbf{D}\}}{dx_{plc}} + \frac{\partial f_{pn}}{\partial x_{plc}} - \{\mathbf{\Lambda}\}^T \frac{\partial [\mathbf{K_0}]}{\partial x_{plc}} \{\mathbf{D}\} \tag{5.14}$$

The computationally expensive $\frac{d\{\mathbf{D}\}}{dx_{plc}}$ is eliminated if the Lagrange multiplier vector is a solution to $\frac{\partial f_{pn}}{\partial\{\mathbf{D}\}} - \{\mathbf{\Lambda}\}^T [\mathbf{K_0}] = \{\mathbf{0}\}$, which is rewritten to obtain Eq. (5.15).

$$[\mathbf{K_0}]\{\mathbf{\Lambda}\} = \left(\frac{\partial f_{pn}}{\partial\{\mathbf{D}\}} \right)^T \tag{5.15}$$

The Lagrange multiplier vector is then inserted to obtain the total derivative $\frac{d\tilde{f}_{pn}}{dx_{plc}}$ in Eq. (5.16).

$$\frac{d\tilde{f}_{pn}}{dx_{plc}} = \frac{\partial f_{pn}}{\partial x_{plc}} - \{\boldsymbol{\Lambda}\}^T \frac{\partial\left[\mathbf{K_0}\right]}{\partial x_{plc}}\{\mathbf{D}\} \tag{5.16}$$

Adjoint equation

$\frac{\partial f_{pn}}{\partial\{\mathbf{D}\}}$ can be expressed by applying the chain rule to Eq. (5.10) as shown in Eq. (5.17).

$$\left(\frac{\partial f_{pn}}{\partial\{\mathbf{D}\}}\right)^T = \sum_{e=1}^{N_e}\sum_{l=1}^{N_{layer}}\sum_{m=1}^{2} \underbrace{[\mathbf{L}]_e}_{N_{DoF}\times 24}\left(\underbrace{[\mathbf{T_{dG}}]_e}_{24\times 20}\left(\underbrace{\frac{\partial f_{pn}}{\partial FI_{elm}^{(eff)}}}_{1\times 1}\underbrace{\frac{\partial FI_{elm}^{(eff)}}{\partial FI_{elmc}}}_{1\times 1}\underbrace{\frac{\partial FI_{elmc}}{\partial\{\boldsymbol{\varepsilon}_{\mathbf{12}}\}_{elmc}}}_{1\times 6}\underbrace{\frac{\partial\{\boldsymbol{\varepsilon}_{\mathbf{12}}\}_{elmc}}{\partial\{\boldsymbol{\varepsilon}_{\mathbf{d}}\}_{elmc}}}_{6\times 6}\underbrace{\frac{\partial\{\boldsymbol{\varepsilon}_{\mathbf{d}}\}_{elmc}}{\partial\{\mathbf{d}\}_e}}_{6\times 20}\right)^T\right) \tag{5.17}$$

The first partial derivative in Eq. (5.17) is calculated by the partial derivative of the P-norm aggregate function in Eq. (5.10) as shown in Eq. (5.18).

$$\frac{\partial f_{pn}}{\partial FI_{elm}^{(eff)}} = \left(FI_{elm}^{(eff)}\right)^{P-1}\left(\sum_{e=1}^{N_e}\sum_{l=1}^{N_{layer}}\sum_{m=1}^{2}\left(FI_{elm}^{(eff)}\right)^P\right)^{\frac{1}{P}-1} \tag{5.18}$$

$FI_{elm}^{(eff)}$ in Eq. (5.9) is differentiated to obtain Eq. (5.19).

$$\frac{\partial FI_{elm}^{(eff)}}{\partial FI_{elmc}} = \sum_{c=1}^{N_c} w_{FI}(x_{plc}) \tag{5.19}$$

The maximum strain criterion can predict mixed failure modes. These load scenarios are rare, so assuming the failure mode is fixed is convenient. This leads to the expression $\frac{\partial FI_{elmc}}{\partial\{\boldsymbol{\varepsilon}_{\mathbf{12}}\}_{elmc}}$ in Eq. (5.20) being a scalar that corresponds to the failure mode. Hence, the dimensions in Eq. (5.17) can be regarded as a mathematical statement rather than implementation details.

$$\frac{\partial FI_{elmc}}{\partial\{\boldsymbol{\varepsilon}_{\mathbf{12}}\}_{elmc}} = \left\lfloor\frac{1}{e_{1x}},\frac{1}{e_{2x}},0,\frac{1}{e_{12}},\frac{1}{e_{13}},\frac{1}{e_{23}}\right\rfloor \tag{5.20}$$

Partial differentiation of Eq. (5.5) yields Eq. (5.21).

$$\frac{\partial\{\boldsymbol{\varepsilon}_{\mathbf{12}}\}_{elmc}}{\partial\{\boldsymbol{\varepsilon}_{\mathbf{d}}\}_{elmc}} = [\mathbf{T}_{\boldsymbol{\theta}}]_{elmc} \tag{5.21}$$

To calculate $\frac{\partial\{\boldsymbol{\varepsilon}_{\mathbf{12}}\}_{elmc}}{\partial\{\boldsymbol{\varepsilon}_{\mathbf{d}}\}_{elmc}}$ it is convenient to introduce the extrapolation matrices $[\mathbf{E}]_{(\pm)}$ in Eq. (5.22).

$$[\mathbf{E}]_{(\pm)} = \begin{bmatrix} \frac{1}{2}(1\pm\sqrt{3}) & 0 & 0 & 0 & 0 & 0 \\ 0 & \frac{1}{2}(1\pm\sqrt{3}) & 0 & 0 & 0 & 0 \\ 0 & 0 & \frac{1}{2}(1\pm\sqrt{3}) & 0 & 0 & 0 \\ 0 & 0 & 0 & \frac{1}{2}(1\pm\sqrt{3}) & 0 & 0 \\ 0 & 0 & 0 & 0 & \frac{1}{2}(1\pm\sqrt{3}) & 0 \\ 0 & 0 & 0 & 0 & 0 & \frac{1}{2}(1\pm\sqrt{3}) \end{bmatrix} \tag{5.22}$$

For $m = 1$ and $m = 2$ then $\frac{\partial\{\boldsymbol{\varepsilon}_{\mathbf{d}}\}_{elmc}}{\partial\{\mathbf{d}\}_e}$ is calculated using Eqs. (5.23) and (5.24).

$$\begin{aligned}\frac{\partial\{\boldsymbol{\varepsilon}_{\mathbf{d}}\}_{el1c}}{\partial\{\mathbf{d}\}_e} = &[\mathbf{E}]_{(-)}\frac{1}{4}\sum_{gp=1}^{4}[\mathbf{T}^{\mathbf{con}}]_{el}^{(gp)}\left([\mathbf{B}]_{e1m}^{(gp)} - [\bar{\mathbf{M}}]_{e1m}^{(gp)}[\mathbf{K}_{\boldsymbol{\alpha\alpha}}]_e^{-1}[\mathbf{K}_{\boldsymbol{\alpha}\mathbf{u}}]_e\right)\\ &+ [\mathbf{E}]_{(+)}\frac{1}{4}\sum_{gp=1}^{4}[\mathbf{T}^{\mathbf{con}}]_{el}^{(gp)}\left([\mathbf{B}]_{e2m}^{(gp)} - [\bar{\mathbf{M}}]_{e2m}^{(gp)}[\mathbf{K}_{\boldsymbol{\alpha\alpha}}]_e^{-1}[\mathbf{K}_{\boldsymbol{\alpha}\mathbf{u}}]_e\right)\end{aligned} \tag{5.23}$$

$$\begin{aligned}\frac{\partial\{\boldsymbol{\varepsilon}_{\mathbf{d}}\}_{el2c}}{\partial\{\mathbf{d}\}_e} = &[\mathbf{E}]_{(+)}\frac{1}{4}\sum_{gp=1}^{4}[\mathbf{T}^{\mathbf{con}}]_{el}^{(gp)}\left([\mathbf{B}]_{e1m}^{(gp)} - [\bar{\mathbf{M}}]_{e1m}^{(gp)}[\mathbf{K}_{\boldsymbol{\alpha\alpha}}]_e^{-1}[\mathbf{K}_{\boldsymbol{\alpha}\mathbf{u}}]_e\right)\\ &+ [\mathbf{E}]_{(-)}\frac{1}{4}\sum_{gp=1}^{4}[\mathbf{T}^{\mathbf{con}}]_{el}^{(gp)}\left([\mathbf{B}]_{e2m}^{(gp)} - [\bar{\mathbf{M}}]_{e2m}^{(gp)}[\mathbf{K}_{\boldsymbol{\alpha\alpha}}]_e^{-1}[\mathbf{K}_{\boldsymbol{\alpha}\mathbf{u}}]_e\right)\end{aligned} \tag{5.24}$$

These equations are used to calculate $\left(\frac{\partial f_{pn}}{\partial\{\mathbf{D}\}}\right)^T$ and determine the Lagrange multiplier vector.

Partial derivative of the aggregated failure criterion

To calculate the total derivative $\frac{\partial f_{pn}}{\partial x_{plc}}$ is the only expression that needs to be calculated since the $\frac{\partial[\mathbf{K_0}]}{\partial x_{plc}}$ is determined in subsection 4.1.2. $\frac{\partial f_{pn}}{\partial x_{plc}}$ is calculated using the chain rule as shown in Eq. (5.25).

$$\frac{\partial f_{pn}}{\partial x_{plc}} = \sum_{e=1}^{N_e}\sum_{l=1}^{N_{layer}}\sum_{m=1}^{2}\frac{\partial f_{pn}}{\partial FI_{elm}^{(eff)}}\frac{\partial FI_{elm}^{(eff)}}{\partial w_{FI}(x_{plc})}\frac{\partial w_{FI}(x_{plc})}{\partial x_{plc}} \tag{5.25}$$

The first partial derivative in Eq. (5.25) is calculated in Eq. (5.18). $\frac{\partial FI_{elm}^{(eff)}}{\partial w_{FI}(x_{plc})}$ results in the element failure index as shown in Eq. (5.26).

$$\frac{\partial FI_{elm}^{(eff)}}{\partial w_{FI}(x_{plc})} = FI_{elm} \tag{5.26}$$

This thesis uses RAMP with negative penalisation as a weight function for FI_{elm}. The calculation of $\frac{\partial w_{FI}(x_{plc})}{\partial x_{plc}}$ is performed using Eq. (4.31). This approach enables the calculation of the sensitivities of the maximum strain criterion using the provided equations.

5.2.2 Single Curved shell

The example of the single curved shell from subsection 4.2.2 and failure strength data in Table 5.1 is used to validate the analytical sensitivities. The absolute error between the analytical DSA $\frac{d\tilde{f}_{pn}}{dx_{plc}}$ and the finite difference approximation is illustrated in Figure 5.2. The error decreases as expected until it becomes numerically unstable (Martins and Ning, 2021). Noticeably, the error is smaller than in the chapter 4.

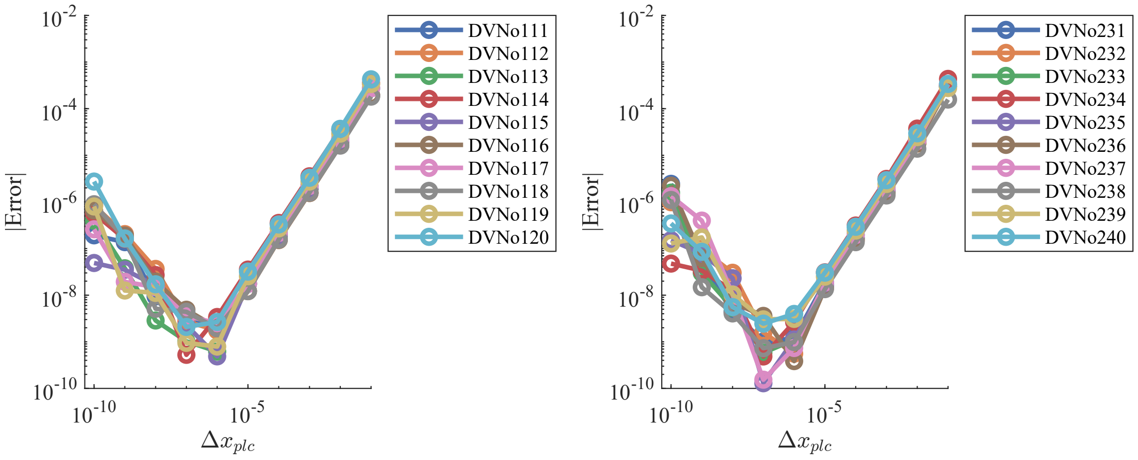

Figure 5.2. Absolute error between the finite difference approximation and the analytical sensitivities in the single-curved shell benchmark example.

Table 5.1. Ultimate failure strength material data .

Constant	Unit	Glass/epoxy	Divinycell H130
X_t	[MPa]	930.0	3.7
X_c	[MPa]	570.0	3.6
Y_t	[MPa]	33.0	3.7
Y_c	[MPa]	110.0	3.6
S_{12}	[MPa]	70.0	2.4
S_{13}	[MPa]	70.0	2.4
S_{23}	[MPa]	41.5	2.4
e_{1t}	[-]	$2.4\cdot10^{-2}$	$3.2\cdot10^{-2}$
e_{1c}	[-]	$1.5\cdot10^{-2}$	$2.0\cdot10^{-2}$
e_{2t}	[-]	$0.4\cdot10^{-2}$	$3.2\cdot10^{-2}$
e_{2c}	[-]	$1.2\cdot10^{-2}$	$2.0\cdot10^{-2}$
e_{12}	[-]	$1.9\cdot10^{-2}$	$4.4\cdot10^{-2}$
e_{13}	[-]	$1.9\cdot10^{-2}$	$4.4\cdot10^{-2}$
e_{23}	[-]	$1.2\cdot10^{-2}$	$4.4\cdot10^{-2}$

5.3 Benchmark Example: Spar Cap

The simplified spar cap model in subsection 4.2.3 compares the buckling-optimised design with a failure-optimised design that includes a buckling constraint. This is achieved by minimising the failure index while ensuring that the buckling load factors are larger than five, as shown in Eqs. (5.27a), (5.27b), (5.27c) and (5.27d). The maximum stress criterion and the Tsai-Wu failure criterion derived in Appendix D and E are used to compare the influence of the failure criterion on the spar cap. It can be observed from Table 5.1 divinycell H130 is not entirely isotropic in the failure strength since the material has differences in tension and compression. However, it is still referred to as an isotropic material in this work.

$$
\begin{aligned}
&\underset{\{\mathbf{x}\}}{\text{Minimise}} && f_{pn}(\{\mathbf{x}\}) && && (5.27a)\\
&\text{Subjected to} && \lambda_j \geq 5, && j = 1, \cdots, 10 && (5.27b)\\
& && \sum_{c=1}^{N_c} x_{plc} = 1 && \forall(e, l, c) && (5.27c)\\
& && x_{plc} \in [0; 1] && \forall(e, l, c) && (5.27d)
\end{aligned}
$$

This benchmark example uses the following continuation strategy on the stiffness penalisation $1, 4, 7, \cdots, 178, 182$. Here, it increases each 3rd iteration or if the convergence tolerance on the objective function is satisfied. The convergence tolerance is set to $0.1 \cdot 10^{-5}$. The stress penalisation is set to 0 throughout the entire optimisation problem. A continuation strategy is used to penalise the failure index. In this strategy, the penalisation factor of the failure index decreases by -0.01 each 3rd iteration, following the sequence $0, -0.01, -0.02, \cdots, -0.8$.

The optimised laminate is shown in 5.3. None of the optimisation problems obtain the same result, but some general tendencies can be observed. At the edges, the maximum strain and Tsai-Wu failure criterion, the fibres are aligned along the load direction, while the top layers in the centre are more transverse to the load direction. The results for the maximum stress criterion are not entirely symmetric around the same symmetry line drawn in Figure 4.16. It is expected this is due to a local minima.

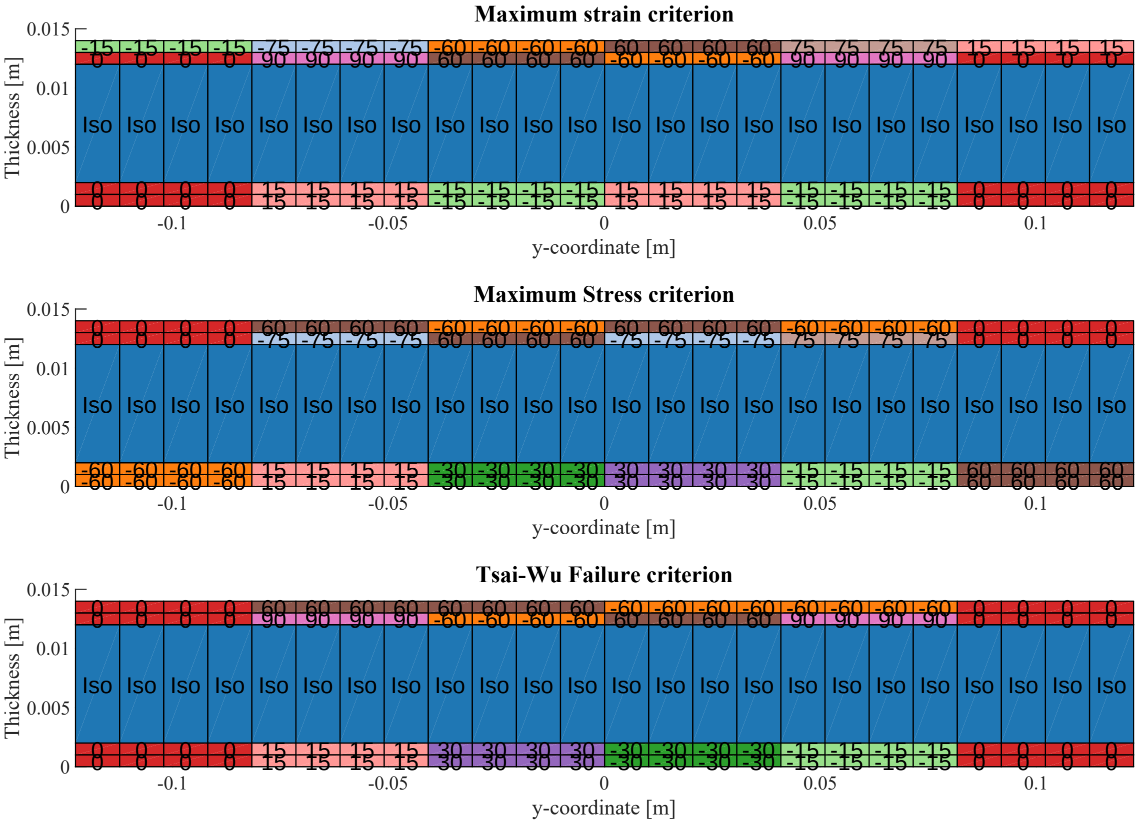
Maximum strain criterion

Maximum Stress criterion

Tsai-Wu Failure criterion

Figure 5.3. The optimised design with the layer angle in degrees.

The convergence curves in Figure 5.4 show a relatively discrete solution, here $m_{cnd} = 0.082\%$ and there are only small oscillations on m_{cnd}. This indicates good convergence behaviour, as stress-based optimisation is recognised for its susceptibility to oscillatory convergence. This is demonstrated by the convergence of the P-norm and the buckling load factor constraint. Here are the amplitudes on the P-norm oscillations significant. The constraint is infeasible for the initial 31 iterations but becomes feasible for the remainder. In the first iteration, a global convergence filter was initialised. This filter is commonly used to enhance global convergence by adaptively expanding and reducing the move limits while rejecting unsatisfactory solutions to the linearised problem. (Hermansen and Lund, 2023a)

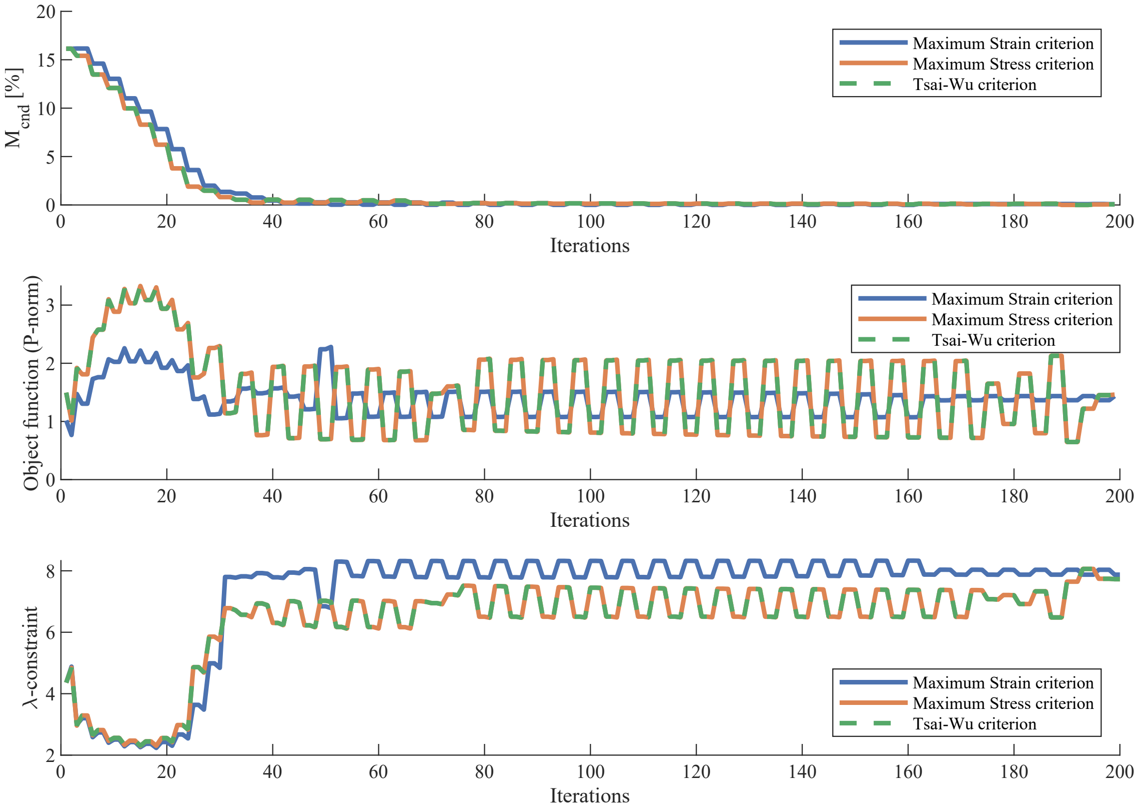

Figure 5.4. Iteration data using the stabilised 4 node shell element

The failure indices for the optimised designs in Figure 5.5 reveal consistently low values across most of the structure except the load introduction and corners. This presents a challenge in stress-constrained optimisation, where singularities at load introductions and corners can make it difficult to achieve feasible stress constraints.

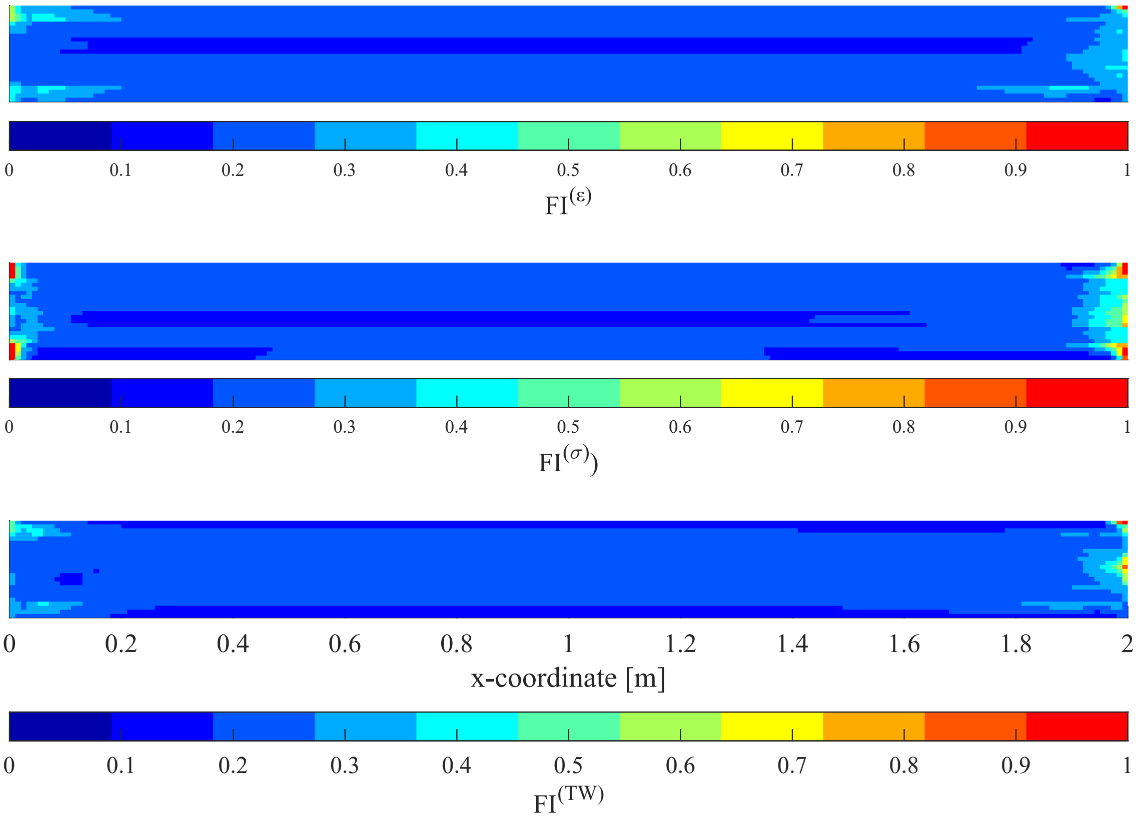

Figure 5.5. Failure index of the optimised design.

6 Conclusion

In conclusion, this thesis has highlighted the limitations of various theories for modelling laminated composites, with a particular focus on ESL-based theories. General laminated composite structures are efficiently modelled using a 4-node shell element with EAS and MITC stabilisation to address in-plane and transverse shear locking. The efficiency of the element formulation makes it computationally attractive to use for the optimisation of laminated composite structures.

The thesis uses the DMO parameterisation, which introduces many linear constraints, making SLP the preferred method. In the design of laminated composites, it is essential to consider buckling to ensure structural integrity. To efficiently address this in optimisation, analytical DSA for linear buckling load factors has been implemented and validated using forward difference approximation. The Bound formulation is utilised to maximise the buckling load factors of three benchmark examples. It is demonstrated that improved computational performance can be achieved using the stabilised 4-node shell element compared to a 9-node shell element while performing similarly to an 8-node solid shell formulation with EAS and ANS stabilisation.

This thesis implements and validates the DSA for the Tsai-Wu failure criterion, maximum strain, and maximum stress criterion. This allows designers and researchers to gain insight into how the choice of failure criterion impacts the design.

The failure criteria are introduced by calculating a failure index and utilising the P-norm aggregate function to express the criteria as a global. To make intermediate densities, unfavourable weight functions are introduced to penalise the stress field and failure index. A benchmark example demonstrates how the choice of failure criterion can significantly impact the design. In this case, three distinct solutions were obtained when minimising the P-norm subjected to a buckling load factor constraint. The results were not fully discrete, and large oscillations were observed in both the P-norm and the buckling constraint.

7 Future work

The optimisation of large structures, such as wind turbine blades, presents a significant challenge due to the trade-off between complexity and the time required to obtain the optimised design. This thesis demonstrates the computational efficiency of the stabilised 4-node shell element in optimisation failure and buckling optimisation. Therefore, the computational advantage is expected to be obtained for other criteria and parameterisations.

7.1 Failure optimisation

This thesis demonstrates efficient DSA for optimisation against failure predicted by the maximum strain, maximum stress and Tsai-Wu failure criterion. These criteria are widely used but come with the drawbacks described in section 3.1. Introducing the Puck failure criterion is particularly interesting for optimising wind turbine blades, as this criterion is commonly used in the industry.

Wind turbine blades are often exposed to various loading conditions, which can result in structural damage, leading to reduced stiffness and strength. As described in the review article by Passipoularidis and Brøndsted (2010), various approaches can be utilised to model fatigue in composite structures. Hermansen and Lund (2023b) introduced high-cycle fatigue as both a constraint and an objective. Predicting fatigue in laminated composite structures with accuracy poses a significant challenge. Furthermore, validating these predictions is costly due to the time required for fatigue experiments. This area of research is particularly complex and interesting to address in optimisation.

7.2 Buckling

Another perspective on fatigue is the stiffness degradation and its effect on compliance, buckling, and free vibration. Several phenomenological-based models exist where a damage type is related to a decrease in some elastic properties.

It could be interesting to use these models to predict the stiffness reduction after a given load spectrum and add buckling or free vibration constraints using the initial stiffness and damaged stiffness. This can theoretically lead to a more damage-tolerant design compared to only using the initial stiffness. This approach requires an additional buckling analysis to be solved, which increases the computational expenses. Further, literature on the accuracy of the stiffness reduction models for complex structures such as wind turbine blades is sparse. Therefore, it raises questions about the worth of the effort.

The linearised buckling analysis assumes a mathematically perfect structure, as described in Appendix B. Therefore, the non-linear buckling problem will increase the accuracy of the buckling analysis and reduce the safety factor of the buckling load factor. Analytical DSA of the non-linear buckling problem can significantly contribute to making it computationally attractive for optimising large laminated composite structures.

The non-linear buckling analysis also allows for considering geometrical and material imperfections, as described in Appendix B.

7.3 Parameterisation

Optimisation with the stabilised 4-node shell element can be extended to include the lamina thickness as a design variable using the Discrete Material and Thickness optimisation (DMTO) by Sørensen et al. (2014). The DMTO scales the constitutive properties with the additional thickness design variable. Initially, this caused challenges with intermediate laminae artificially increasing the moment of inertia. This issue and the requirements for thickness variation due to manufacturing are effectively addressed by introducing additional constraints as explained in Sørensen et al. (2014). Instead of scaling the constitutive properties Sjølund et al. (2018) proposed the DMTO parameterisation where the thickness-variable is scaled directly, therefore later referred to as Discrete Material and Direct Thickness Optimisation (DMDTO). Analytical DSA of the thickness variable using DMDTO is particularly interesting to implement for the EAS and MITC stabilised 4-node shell element since selecting the appropriate layer thickness is crucial for designing wind turbine blades. Therefore, implementing analytical DSA of the thickness variable for the stabilised 4-node shell element will be a substantial step towards computationally efficient optimisation of wind turbine blades.

Bibliography

Ahmad et al., 1970. S. Ahmad, B. M. Irons and O. C. Zienkiewicz. *Analysis of thick and thin shell structures by curved finite elements.* International Journal for Numerical Methods in Engineering, 2(3), 419–451, 1970.

Bathe, 2013. K. J. Bathe. *The subspace iteration method – Revisited.* Computers Structures, 126, 177–183, 2013.

Bathe and Wilson, 1973. K. J. Bathe and E. L. Wilson. *Solution methods for eigenvalue problems in structural mechanics.* International journal for numerical methods in engineering, 6(2), 213–226, 1973.

Bendsøe, 1989. M. P. Bendsøe. *Optimal shape design as a material distribution problem.* Structural Optimization, 1, 193–202, 1989.

Bendsøe and Olhoff, 1985. M. P. Bendsøe and N. Olhoff. *A method of design against vibration resonance of beams and shafts.* Optimal control applications methods, 6(3), 191–200, 1985.

Bruggi, 2008. M. Bruggi. *On an alternative approach to stress constraints relaxation in topology optimization.* Structural and multidisciplinary optimization, 36(2), 125–141, 2008.

Bruns, 2005. T. E. Bruns. *A reevaluation of the SIMP method with filtering and an alternative formulation for solid-void topology optimization.* Structural and multidisciplinary optimization, 30(6), 428–436, 2005.

Cook et al., 2001. R. D. Cook, D. S. Malkus, M. E. Plesha and R. J. Witt. *Concepts and applications of finite element analysis.* John Wiley & Sons, New York, 4 edition, 2001. ISBN 9780471356059.

Dvorkin and Bathe, 1984. E. N. Dvorkin and K. J. Bathe. *A continuum mechanics based four-node shell element for general non-linear analysis.* Engineering Computations, 1(1), 77–88, 1984.

Dym and Shames, 2013. C. L. Dym and I. H. Shames. *Solid Mechanics : A Variational Approach, Augmented Edition.* Springer New York, New York, NY, 2013. ISBN 9781461460343.

Euler, 1744. L. Euler. *Methodus inveniendi lineas curvas maximi minimive proprietate gaudentes, sive Solutio problematis isoperimetrici latissimo sensu accepti.* 1744.

Gadegaard and Thuesen, 2022. F. J. Gadegaard and J. Thuesen. *Strength based optimization and test of fiber reinforced additively manufactured structures considering topology and fiber orientation*, 2022.

Goodno. and Gere, 2016. J. B Goodno. and J. M Gere. *Mechanics of Materials.* Cengage Learning, Boston, Mass; Australia, 9. edition, si edition. edition, 2016. ISBN 9781337093354.

Groenwold and Haftka, 2006. A. A. Groenwold and R. T. Haftka. *Optimization with non-homogeneous failure criteria like Tsai-Wu for composite laminates.* Structural and multidisciplinary optimization, 32(3), 183–190, 2006.

Hart-Smith, 1990. L. J. Hart-Smith. *Fibrous Composite Laminate Strength Prediction Demystified.* 1990.

Henrichsen, 2015. S. R. Henrichsen. *Optimization of Laminated Composite Structures*, 2015. Ph.D Thesis, Aalborg University.

Henrichsen et al., 2015. S. R. Henrichsen, E. Lindgaard and E. Lund. *Robust buckling optimization of laminated composite structures using discrete material optimization considering "worst" shape imperfections.* Thin-Walled Structures, 94, 624–635, 2015.

Henrichsen et al., 2016. S. R. Henrichsen, P. M. Weaver, E. Lindgaard and E. Lund. *Post-buckling optimization of composite structures using Koiter's method.* International Journal for Numerical Methods in Engineering, 108(8), 902–940, 2016.

Hermansen and Lund, 2023a. S. M. Hermansen and E. Lund. *Multi-material and thickness optimization of a wind turbine blade root section*, 2023a. 12 December 2023, PREPRINT (Version 1) available at Research Square, [https://doi.org/10.21203/rs.3.rs-3710253/v1].

Hermansen and Lund, 2023b. S. M. Hermansen and E. Lund. *Multi-material and thickness optimization of laminated composite structures subject to high-cycle fatigue.* Structural and multidisciplinary optimization, 66(12), 259, 2023b.

Hua et al., 2022. X. Hua, Z. Lia, R. Baoa, W. Chena and H. Wanga. *An adaptive method of moving asymptotes for topology optimization based on the trust region.* Computer Methods in Applied Mechanics and Engineering, Journal 393, 2022.

Hvejsel and Hansen, 2007. C. F. Hvejsel and H. F. Hansen. *Efficient finite element formulation for analysis and optimization of laminated composite shell structures.* 2007.

Hvejsel and Lund, 2011. C. F. Hvejsel and E. Lund. *Material interpolation schemes for unified topology and multi-material optimization.* Structural and Multidisciplinary Optimization, 43(6), 811–825, 2011.

Jakobsen, 2022. J. Jakobsen. *Notes for course on Mechanics of Composite Materials and Structures*, 2022. M.Sc. course on Aalborg University, Lecture 7–Static failure in composite materials (part-2).

Jones, 1998. R. M. Jones. *Mechanics of Composite Materials.* ISBN:1-56032-712-x. Taylor & Francis Inc., 1998.

Kirsch, **1989**. U. Kirsch. *Optimal topologies of truss structures.* Computer Methods in Applied Mechanics and Engineering, 72(1), 15–28, 1989.

Kirsch, **1990**. U. Kirsch. *On singular topologies in optimum structural design.* Structural Optimization, 2(3), 133–142, 1990.

Klinkel and Wagner, **1997**. S. Klinkel and W. Wagner. *A geometrical non-linear brick element based on the EAS-method.* International journal for numerical methods in engineering, 40(24), 4529–4545, 1997.

Klinkel et al., **1999**. S. Klinkel, F. Gruttmann and W. Wagner. *A continuum based three-dimensional shell element for laminated structures.* Computers Structures, 71(1), 43–62, 1999.

Kühlmeier, **2006**. L. Kühlmeier. *Buckling of wind turbine rotor blades – analysis, design and experimental validation*, 2006. Ph.D. Thesis, Institute of Mechanical Engineering, Aalborg University, Denmark, special report no. 58.

Labanda and Stolpe, **2015**. S. R. Labanda and M. Stolpe. *Automatic penalty continuation in structural topology optimization.* Structural and multidisciplinary optimization, 52(6), 1205–1221, 2015.

Le et al., **2010**. C. Le, J. Norato, T. Bruns, C. Ha and D. Tortorelli. *Stress-based topology optimization for continua.* Structural and multidisciplinary optimization, 41 (4), 605–620, 2010.

Levinson, **1980**. M. Levinson. *An accurate, simple theory of the statics and dynamics of elastic plates.* Mechanics research communications, 7(6), 343–350, 1980.

Lindgaard, **2020**. E. Lindgaard. *Notes for course on Analysis of Laminated Composite Structures*, 2020. Ph.D. course on Aalborg University, Buckling Analysis and Design Optimization of Laminated Composite Structures.

Lindgaard, **2013**. E. Lindgaard. *An Optimization Formulation for Improved Post-Buckling Stability of Laminated Composite Structures.* 2013. In: Proc. WCSMO10 - 10th World Congress on Structural and Multidisciplinary Optimization, Orlando, Florida, 19-24 May 2013, USA.

Lindgaard and Lund, **2011**. E. Lindgaard and E. Lund. *Optimization Formulations for the Maximum Nonlinear Buckling Load of Composite Structures.* Structural and Multidisciplinary Optimization, 43(5), 631–646, 2011.

Lindgaard et al., **2010**. E. Lindgaard, E. Lund and K. Rasmussen. *Nonlinear buckling optimization of composite structures considering "worst" shape imperfections.* International Journal of Solids and Structures, 47(22), 3186–3202, 2010.

Lund, **2022**. E. Lund. *Notes for course on Analysis of Laminated Composite Structures*, 2022. Ph.D. course on Aalborg University, Analysis and Gradient Based Optimization of Laminated Composite Structures.

Lund, 2018. E. Lund. *Discrete Material and Thickness Optimization of laminated composite structures including failure criteria.* Structural and Multidisciplinary Optimization, 57(6), 2357–2375, 2018.

Lund, 1994. E. Lund. *Finite Element Based Design Sensitivity Analysis and Optimization*, 1994. Ph.D Thesis, Aalborg University.

Lund, 2009. E. Lund. *Buckling topology optimization of laminated multi-material composite shell structures.* Composite Structures, 91(2), 158–167, 2009.

Lund and Lindgaard, 2022. E. Lund and E. Lindgaard. *Notes for course in Finite Element Methods*, 2022. M.Sc. course on Aalborg University, Lecture 8–Geometric non-linearity.

Martins and Ning, 2021. J. R. R. A. Martins and A. Ning. *Engineering Design Optimization.* Cambridge University Press, 2021. ISBN 9781108833417.

Medwadowski, 1958. S. J. Medwadowski. *A Refined Theory of Elastic, Orthotropic Plates.* Journal of Applied Mechanics, 25(4), 437–443, 1958.

Mishnaevsky et al., 2017. L. Mishnaevsky, K. Branner, H. N. Petersen, J. Beauson, M. McGugan and B. F. Sørensen. *Materials for Wind Turbine Blades: An Overview.* Materials, 10(11), 2017. ISSN 1996-1944.

Murthy, 1981. M. V. V. Murthy. *An improved transverse shear deformation theory for laminated antisotropic plates.* 1981.

Nielsen, 2018. S. R. K. Nielsen. *Tensor Calculus with applications to Differential Theory of Surfaces and Dynamics.* (242), 2018.

Nikbakt et al., 2018. S. Nikbakt, S. Kamarian and M. Shakeri. *A review on optimization of composite structures Part I: Laminated composites.* Composite Structures, 195, 158–185, 2018.

Olhoff, 1989. N. Olhoff. *Multicriterion structural optimization via bound formulation and mathematical programming.* Structural Optimization, 1(1), 11–17, 1989.

Passipoularidis and Brøndsted, 2010. V. Passipoularidis and P. Brøndsted. *Fatigue Evaluation Algorithms: Review*, 2010.

Petersson and Sigmund, 1998. J. Petersson and O. Sigmund. *Slope constrained topology optimization.* International journal for numerical methods in engineering, 41 (8), 1417–1434, 1998.

Puck and Schürmann, 2002. A. Puck and H. Schürmann. *Failure analysis of FRP laminates by means of physically based phenomenological models.* Composites Science and Technology, 62(12), 1633–1662, 2002.

Ragani et al., 2023. A. F. Ragani, P. Stein, R. Keene and I. Symingto. *Unveiling the next frontier of engineering simulation.* 2023.

Reddy, 1984. J. N. Reddy. *Simple higher-order theory for laminated composite plates.* Journal of Composite Materials, 52, 745–752, 1984.

Reddy, **1986**. J. N. Reddy. *A Refined Shear Deformation Theory for the Analysis of Laminated Plates.* NASA Contractor Report 3955, 1986.

Schøn, **2023**. R. K. Schøn. *Adjoint sensitivity analysis and optimisation of laminated composites using a stabilised 4-node shell element*, 2023.

Seyranian et al., **1994**. A. P. Seyranian, E. Lund and N. Olhoff. *Multiple eigenvalues in structural optimization problems.* Structural Optimization, 8(4), 207–227, 1994.

Simo and Rifai, **1990**. J. C. Simo and M. S. Rifai. *A class of mixed assumed strain methods and the method of incompatible modes.* International Journal for Numerical Methods in Engineering, 29(8), 1595–1638, 1990.

Sjølund et al., **2018**. J. H. Sjølund, D. Peeters and E. Lund. *A new thickness parameterization for Discrete Material and Thickness Optimization.* Structural and Multidisciplinary Optimization, 58(5), 1885–1897, 2018.

Sørensen et al., **2014**. S. N. Sørensen, R. Sørensen and E. Lund. *DMTO – a method for Discrete Material and Thickness Optimization of laminated composite structures.* Structural and Multidisciplinary Optimization, 50(1), 25–47, 2014.

Stagsted and Bertelsen, **2023**. N. K. K. Stagsted and N. M. Bertelsen. *4-Node Stabilised Shell Element Accounting for Large Displacements, Drilling and Draping in Structural Optimisation of Laminated Composites*, 2023.

Stegmann and Lund, **2005**. J. Stegmann and E. Lund. *Discrete material optimization of general composite shell structures.* International Journal for Numerical Methods in Engineering, 62(14), 2009–2027, 2005.

Stolpe and Svanberg, **2001**. M. Stolpe and K. Svanberg. *An alternative interpolation scheme for minimum compliance topology optimization.* Structural and multidisciplinary optimization, 22, 116–124, 2001.

Svanberg, **1987**. K. Svanberg. *The method of moving asymptotes-a new method for structural optimization.* International journal for numerical methods in engineering, 24 (2), 359–373, 1987.

Sved and Ginos, **1968**. G. Sved and Z. Ginos. *Structural optimization under multiple loading.* International journal of mechanical sciences, 10(10), 803–805, 1968. ISSN 0020-7403.

Troelsgaard et al., **2023**. C. Troelsgaard, F. Elmstrøm, F. Østergaard, J. Hansen and R. K. Schøn. *The Science of Compliance: Continuous Fiber Angle Topology Optimization with Stress Constraints and Path-Planning*, 2023.

Vu-Quoc and Tan, **2003**. L. Vu-Quoc and X. G. Tan. *Optimal solid shells for non-linear analyses of multilayer composites. II. Dynamics.* Computer methods in applied mechanics and engineering, 192(9), 1017–1059, 2003.

Whitney, **1969**. J. M. Whitney. *The Effect of Transverse Shear Deformation on the Bending of Laminated Plates.* Journal of Composite Materials, 3(3), 534–547, 1969.

Whitney and Pagano, 1970. J. M. Whitney and N. J. Pagano. *Shear deformation in heterogeneous anisotropic plates.* Journal of Applied Mechanics, 37, 1031–1036, 1970.

A Covariant Green-Lagrange strain tensor

This chapter derives the Green-Lagrange strain tensor in covariant components from Vu-Quoc and Tan (2003) and Stagsted and Bertelsen (2023). This chapter is written in matrix-vector notation to conform to the FE-form but concerns tensors. Therefore it is still referred to as tensors.

The derivation is initiated from the general definition of the Green-Lagrange strain tensor $[\mathbf{E}]$ in Eq. (A.1).

$$[\mathbf{E}] = \frac{1}{2}\left([\mathbf{F}]^T [\mathbf{F}] - [\mathbf{I}]\right) \tag{A.1}$$

Here $[\mathbf{I}]$ is the identity tensor, and $[\mathbf{F}]$ is the deformation gradient.

The position of the deformed configuration denoted $\{\mathbf{X}\}$ and undeformed configuration $\{\mathbf{x}\}$ is used to define the deformation gradient $[\mathbf{F}] = \frac{\partial\{\mathbf{x}\}}{\partial\{\mathbf{X}\}}$. To formulate the deformation gradient using Curvilinear coordinates, then the covariant base in Eq. (2.3) of the undeformed configuration and contravariant base in the deformed configuration as shown in Eq. (A.2).

$$[\mathbf{F}] = \frac{\partial\{\mathbf{x}\}}{\partial\{\mathbf{X}\}} = \{\mathbf{g}_i\}\{\mathbf{G}^j\}^T \tag{A.2}$$

The identity tensor in Curvilinear coordinates can be expressed in various forms, where it is convenient to use the form in Eq. (A.3).

$$[\mathbf{I}] = G_{ij}\{\mathbf{G}^i\}\{\mathbf{G}^j\}^T \tag{A.3}$$

Eq. (A.2) and (A.3) are inserted to Eq. (A.1) and to obtain Eq. (A.4)(Vu-Quoc and Tan, 2003), where E_{ij} is the covariant components of the strain tensor.

$$[\mathbf{E}] = \frac{1}{2}\left((\{\mathbf{G}^i\}\{\mathbf{g}_j\}^T)(\{\mathbf{g}_i\}\{\mathbf{G}^j\}^T) - G_{ij}\{\mathbf{G}^i\}\{\mathbf{G}^j\}^T\right) = \underbrace{\frac{1}{2}(g_{ij} - G_{ij})}_{=E_{ij}}\{\mathbf{G}^i\}\{\mathbf{G}^j\}^T \tag{A.4}$$

$\{\mathbf{g}_i\}$ can be expressed using the initial configuration and the displacements $\{\mathbf{g}_i\} = \frac{\partial\{\mathbf{x}\}}{\partial r_i} = \{\mathbf{G}_i\} + \frac{\partial\{\mathbf{u}\}}{\partial r_i}$ and $g_{ij} = \{\mathbf{g}_i\}\cdot\{\mathbf{g}_j\}$. This is substituted into the expression for E_{ij} to obtain the Covariant Green-Lagrange strain tensor in Eq. (A.5).

$$\begin{aligned} E_{ij} &= \frac{1}{2}\left(\left(\{\mathbf{G}_i\} + \frac{\partial\{\mathbf{u}\}}{\partial r_i}\right)\left(\{\mathbf{G}_j\} + \frac{\partial\{\mathbf{u}\}}{\partial r_j}\right) - G_{ij}\right) \\ &= \frac{1}{2}\left(\underbrace{\{\mathbf{G}_i\}\frac{\partial\{\mathbf{u}\}}{r^j} + \frac{\partial\{\mathbf{u}\}}{r^i}\{\mathbf{G}_j\}}_{\text{Linear term}} + \underbrace{\frac{\partial\{\mathbf{u}\}}{r^i}\frac{\partial\{\mathbf{u}\}}{r^j}}_{\text{Nonlinear term}}\right) \end{aligned} \tag{A.5}$$

B Optimisation of Structural Instabilities

Structures can obtain several equilibrium configurations, but not all are stable. Therefore, it is essential to account for buckling to prevent failure and structural instability. The study of buckling has a long history in engineering. It can be traced back to the publication by Euler (1744), where the buckling load for a column was calculated. Therefore, this type of problem is often called Euler buckling. Advanced methods have been developed to predict and optimise buckling behaviour in structural mechanics. (Goodno. and Gere, 2016)

The excellent stiffness and strength-to-weight ratios allow designers to design thin-walled structures to obtain low mass. As a result, buckling often becomes a crucial factor in the design of laminated composites. Buckling can take various forms, such as bifurcation buckling. This buckling occurs when some part of the structure converts the membrane strain energy into bending strain energy without applying additional load. This results in large bending deformation to dissipate the membrane strain energy. It can also occur without bifurcation, known as a limit point, where an increase in load leads to "snap-through" buckling, and the structure adopts a new equilibrium configuration.

Buckling problems are often addressed in optimisation through linearised buckling despite being non-conservative and unable to predict limit points. Linear buckling analysis assumes a perfect structure without imperfections, disregarding the membrane and bending coupling. Therefore, high safety factors should be used in linear buckling analysis. On the other hand, non-linear buckling analysis provides more accurate buckling behaviour and information about the post-buckling regime, but it comes at a higher computational cost. (Cook et al., 2001)

The ability of structures to withstand buckling loads is significantly affected by imperfections such as geometric, material, and load variations. There are several ways to consider the effects of geometric imperfections in the analysis. These include incorporating initial geometric flaws, introducing variations in material properties, and considering observed imperfections in the physical structure. However, if the physical structure is not available, other approaches, such as utilising the lowest mode shape of buckling as a geometric imperfection, can be used. These approaches involve introducing imperfections that lead to the lowest buckling load of the structure, known as the "worst" shape imperfection. However, using the lowest buckling mode shape as a geometric imperfection may not always accurately predict the "worst" imperfection. (Lindgaard, 2020) As a result, Lindgaard et al. (2010) and Henrichsen et al. (2015) developed a two-step optimisation process known as recurrence optimisation. It involves minimising the buckling load to determine the buckling mode shape and calculate the "worst" shape imperfection by adding multiple mode shapes. Afterwards, the buckling load is maximised for the imperfect structure to achieve a more reliable design. To achieve a design that is resistant to buckling load, both linear and non-linear compliance minimisation techniques can be utilised as they enhance the overall stiffness of the structure. Lindgaard and Lund (2011) proposed an optimisation method using an element non-linearity factor to improve resistance to buckling load for problems without stability points. The formulation was tested against several other formulations, including linear buckling, nonlinear buckling, linear compliance, nonlinear compliance, and first principal strain. The findings showed that the most favourable formulation depends on the buckling behaviour. Nonlinear buckling was superior for buckling with instability points, while the element non-linearity factor formulation was preferred when stability points were absent.

In certain situations, loads exceeding the buckling load may enhance a structure's performance. As a result, a new field has emerged known as post-buckling optimisation, which involves employing methods to achieve stable post-buckled structures. According to the Lagrange-Dirichlet theorem, for a structure to be stable, the eigenvalues of the tangent stiffness matrix must be positive. Therefore, as shown by Lindgaard (2013), optimisation for stable post-buckled configurations can be obtained by ensuring that the eigenvalues are positive. Henrichsen et al. (2016) and Henrichsen (2015) introduced an alternative method using Koiter's asymptotic analysis, involving calculating Koiter factors. The method draws from Koiter's asymptotic analysis, where a positive b-Koiter factor indicates a stable configuration and a negative a-Koiter factor means asymmetric buckling behaviour. Several objective functions were developed, such as maximising the b-Koiter factor and minimising the absolute value of the a-Koiter factor. One key benefit of the proposed method is that it reduces the computationally expensive post-buckling problem to a series of linear buckling problems. The accuracy of the post-buckling behaviour can be enhanced by including an additional linear term, but choosing an appropriate number of linear terms is challenging.

These methods have different characteristics regarding conservativeness, objective and computational efficiency, but they serve as valuable methods to prevent failure of laminated composites due to structural instabilities.

C Buckling DSA Studies

C.1 DSA comparison of stabilised 4-node shell element and EAS stabilised 8-node solid shell element

The following graphs show the absolute error between the forward difference approximation and the analytical sensitivities for the stabilised 4-node shell element and EAS stabilised 8-node solid shell element at different perturbations Δx_{plc}.

The results show nearly exact same behaviour using when $10^{-1} \leq \Delta x_{plc} \leq 10^{-4}$. The results using perturbations from $10^{-5} \leq \Delta x_{plc} \leq 10^{-10}$ shows very different behaviour. The absolute error for the stabilised 4-node shell element is generally lower, and the highest values tend to cluster around certain design variables at higher buckling loads. This clustering is not observed for the 8-node solid shell element, but the absolute error is larger, and the largest values are observed at the highest buckling load.

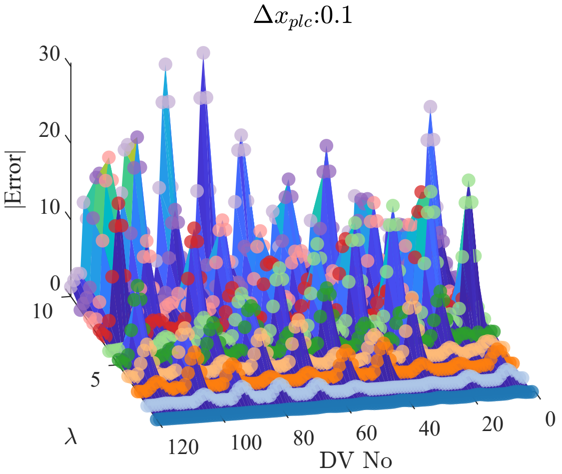

Figure C.1. Stabilised 4-node shell element

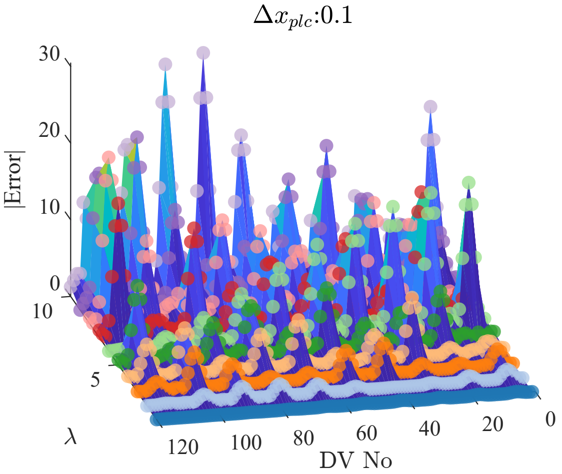

Figure C.2. EAS stabilised 8-node solid shell element

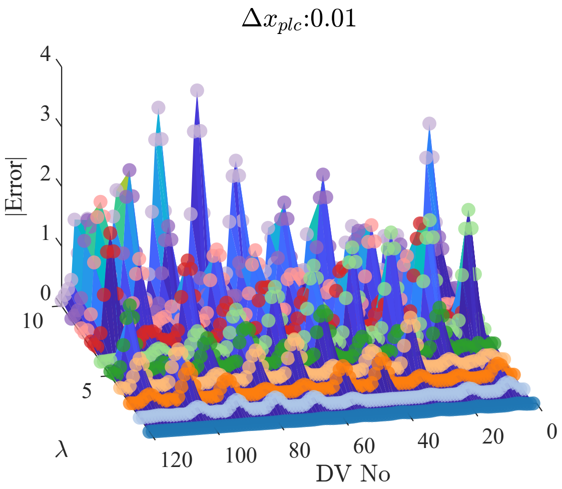

Figure C.3. Stabilised 4-node shell element

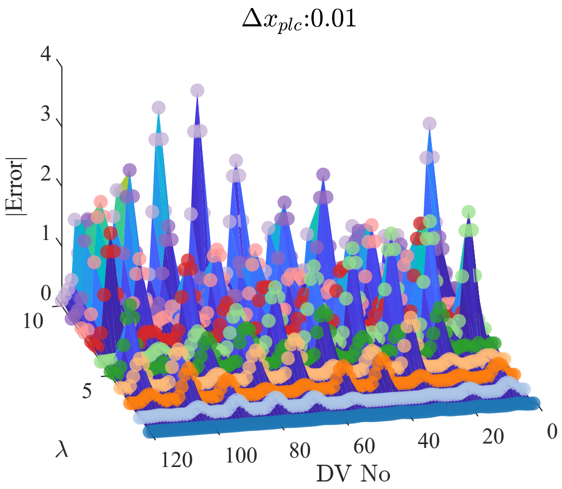

Figure C.4. EAS stabilised 8-node solid shell element

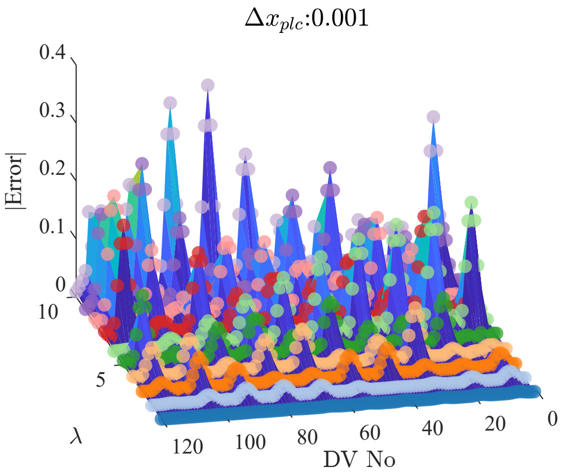

Figure C.5. Stabilised 4-node shell element

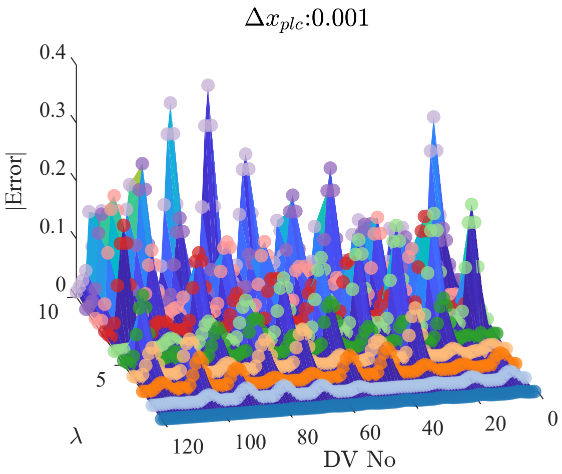

Figure C.6. EAS stabilised 8-node solid shell element

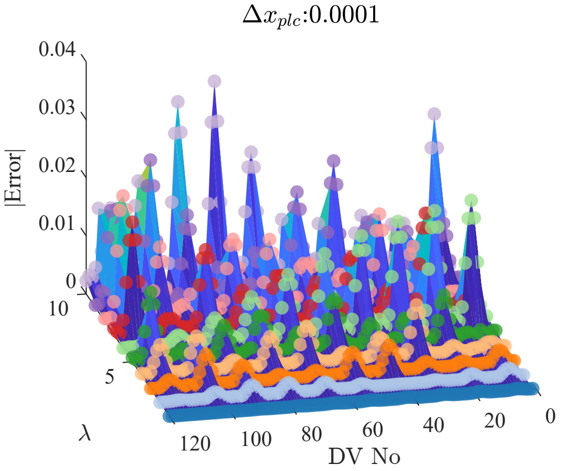

Figure C.7. Stabilised 4-node shell element

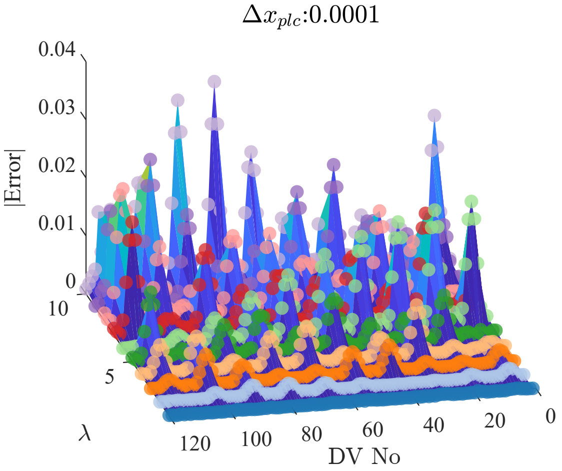

Figure C.8. EAS stabilised 8-node solid shell element

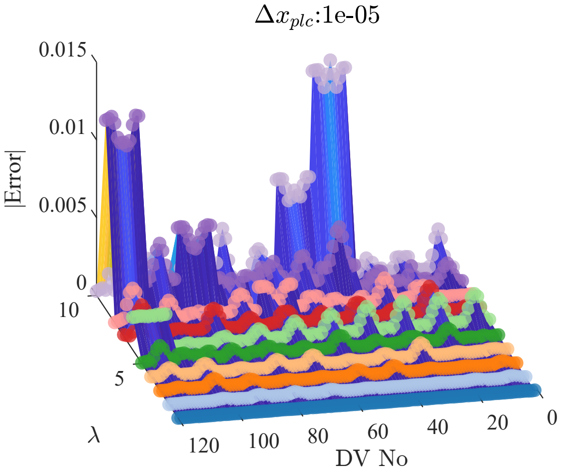

Figure C.9. Stabilised 4-node shell element

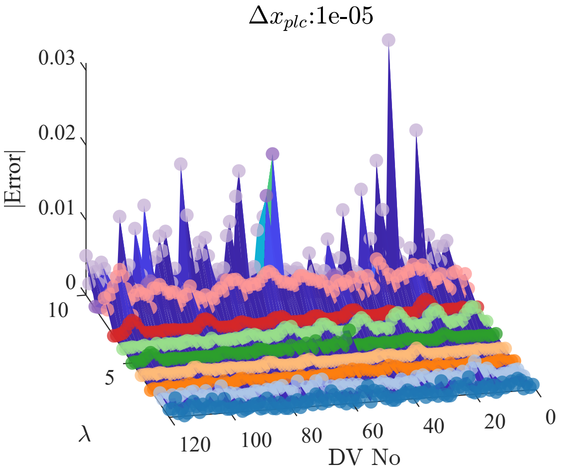

Figure C.10. EAS stabilised 8-node solid shell element

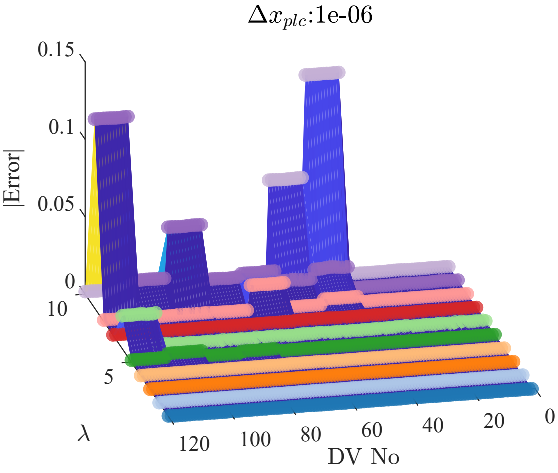

Figure C.11. Stabilised 4-node shell element

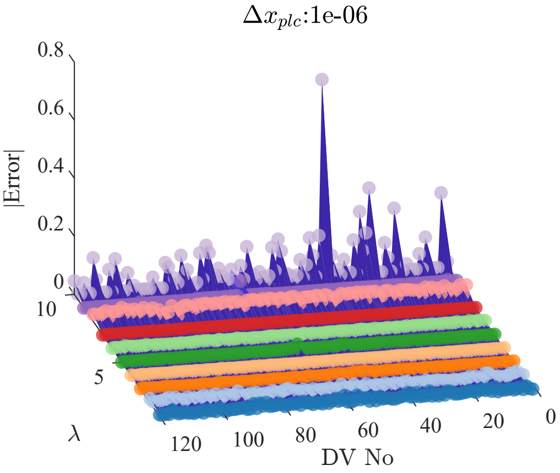

Figure C.12. EAS stabilised 8-node solid shell element

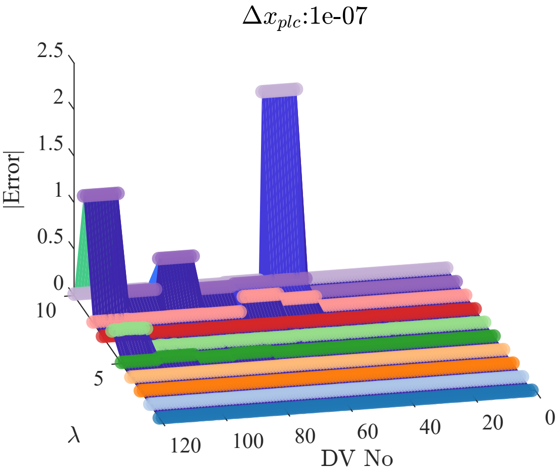

Figure C.13. Stabilised 4-node shell element

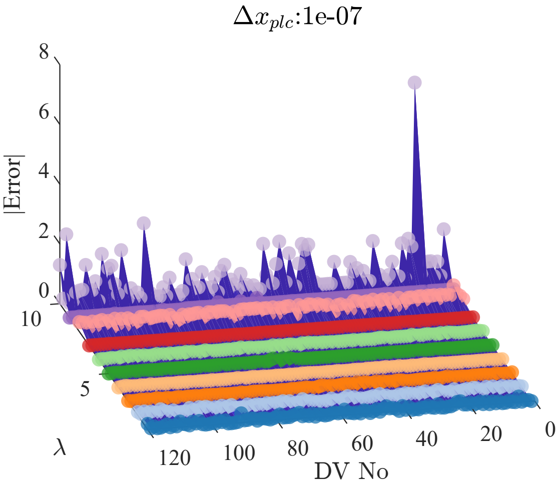

Figure C.14. EAS stabilised 8-node solid shell element

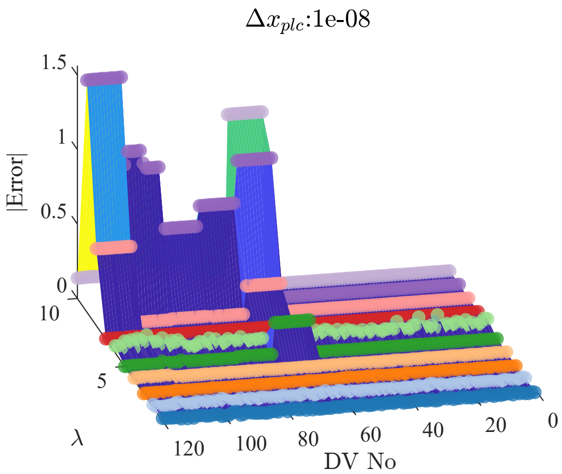

Figure C.15. Stabilised 4-node shell element

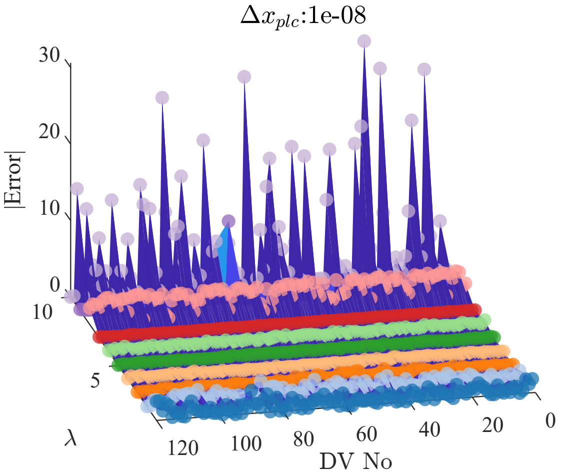

Figure C.16. EAS stabilised 8-node solid shell element

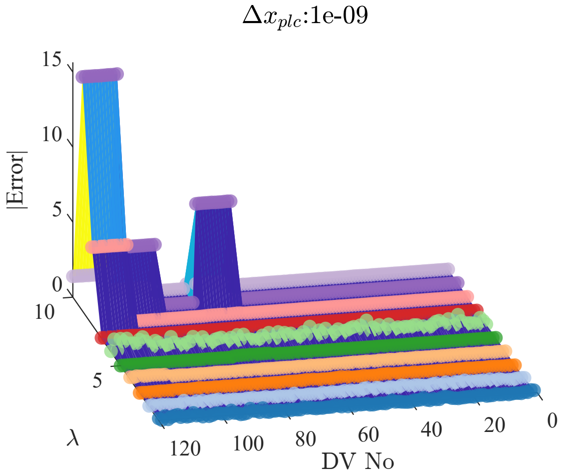

Figure C.17. Stabilised 4-node shell element

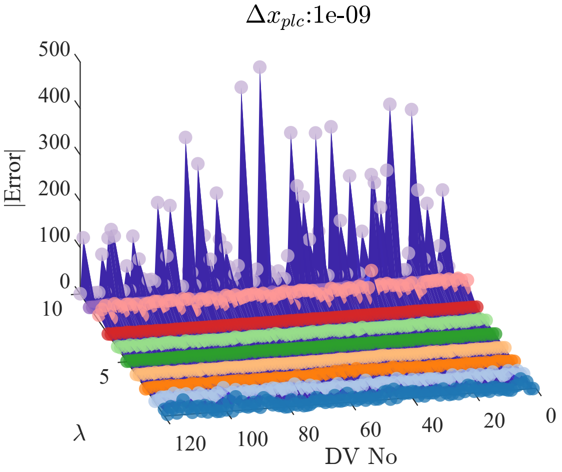

Figure C.18. EAS stabilised 8-node solid shell element

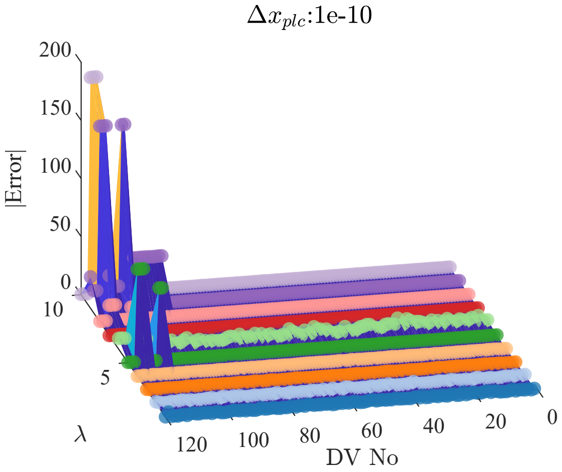

Figure C.19. Stabilised 4-node shell element

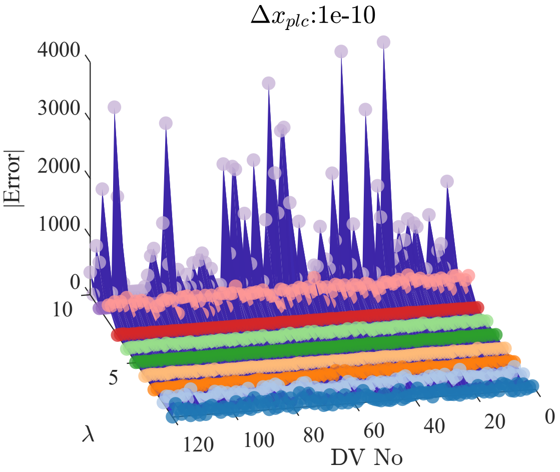

Figure C.20. EAS stabilised 8-node solid shell element

C.2 Non-rectangular element DSA comparison of stabilised 4-node shell element and EAS stabilised 8-node solid shell element

The non-rectangular element model is used to investigate the impact of the EAS contribution on the results.

Similar to the results for the model with rectangular elements, nearly the same behaviour when $10^{-1} \leq \Delta x_{plc} \leq 10^{-4}$. However, when the perturbation is 10^{-4}, the absolute error increases at higher eigenvalues for some of the first design variables when the stabilised 4-node shell element is used. In this region, the error remains large compared to the other sensitivities when $10^{-4} \leq \Delta x_{plc} \leq 10^{-7}$ followed by an increasing absolute error and clustering around certain $\frac{d\lambda_i}{dx_{plc}}$.

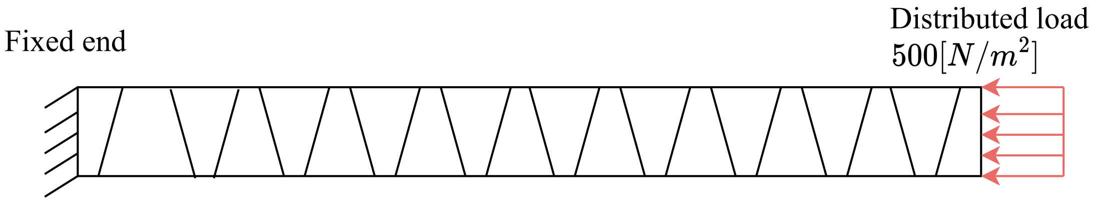

Figure C.21. Cantilever beam modelled with Non-rectangular. Dimensions are the same as the single-layered cantilever beam in Figure 4.1

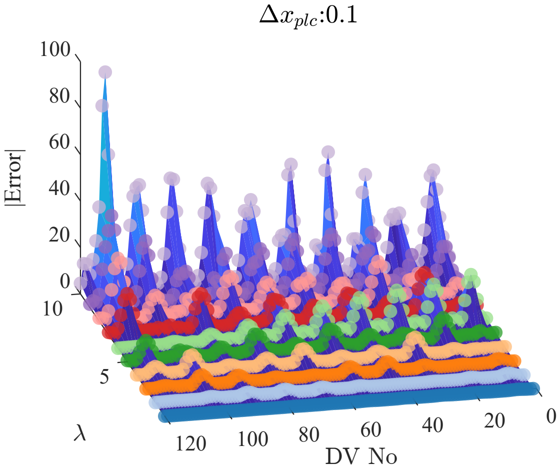

Figure C.22. Cantilever beam with non-rectangular stabilised 4-node shell element

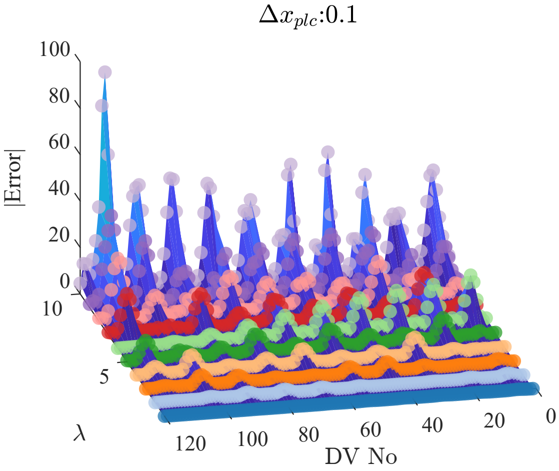

Figure C.23. Cantilever beam with non-rectangular EAS stabilised 8-node solid shell element

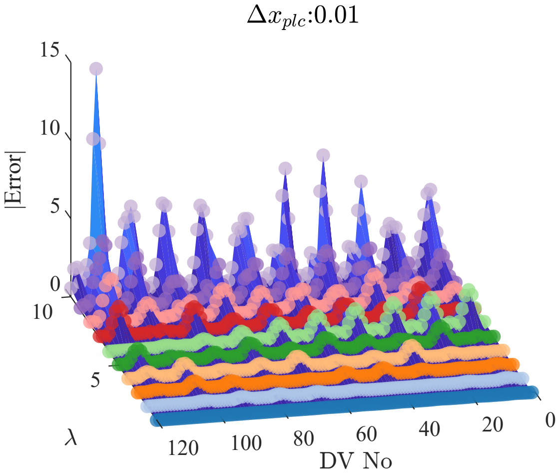

Figure C.24. Cantilever beam with non-rectangular stabilised 4-node shell element

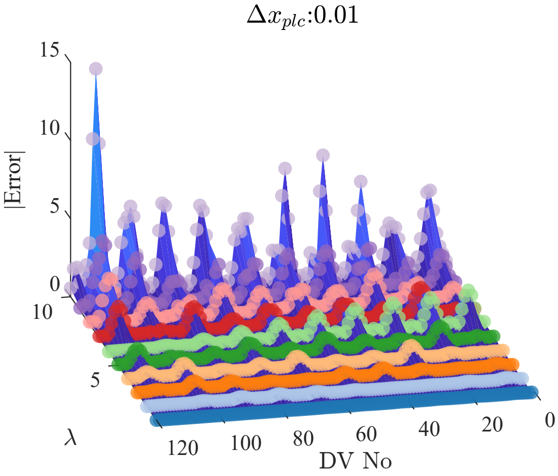

Figure C.25. Cantilever beam with non-rectangular EAS stabilised 8-node solid shell element

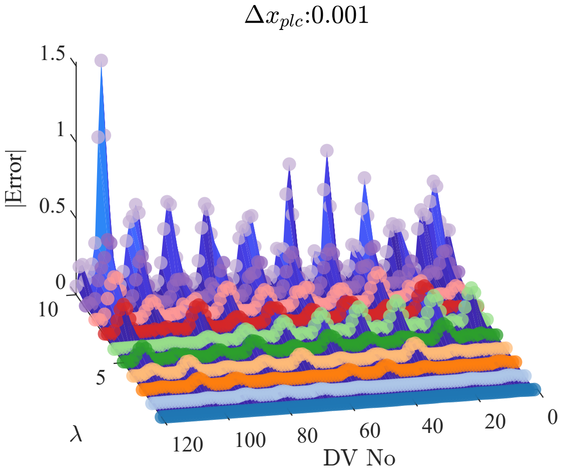

Figure C.26. Cantilever beam with non-rectangular stabilised 4-node shell element

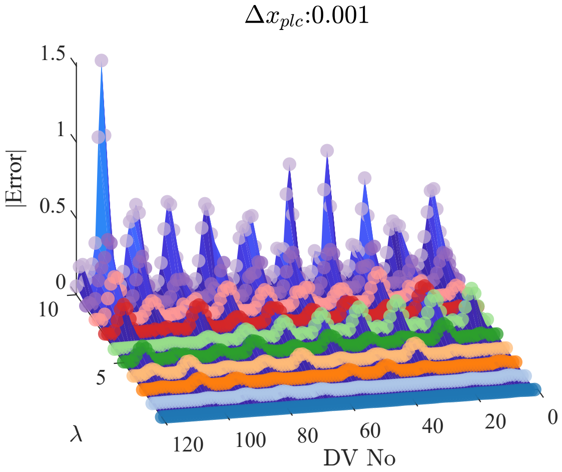

Figure C.27. Cantilever beam with non-rectangular EAS stabilised 8-node solid shell element

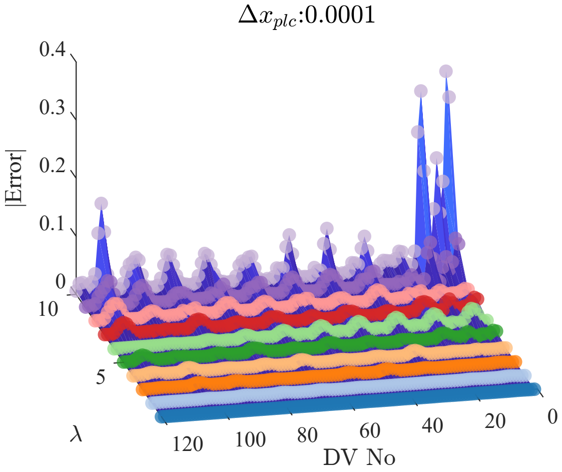

Figure C.28. Cantilever beam with non-rectangular stabilised 4-node shell element

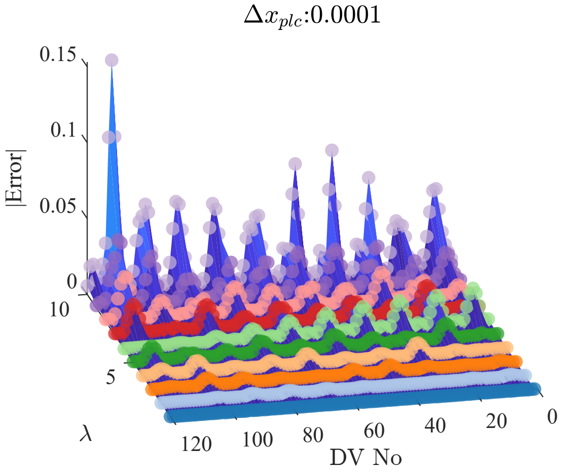

Figure C.29. Cantilever beam with non-rectangular EAS stabilised 8-node solid shell element

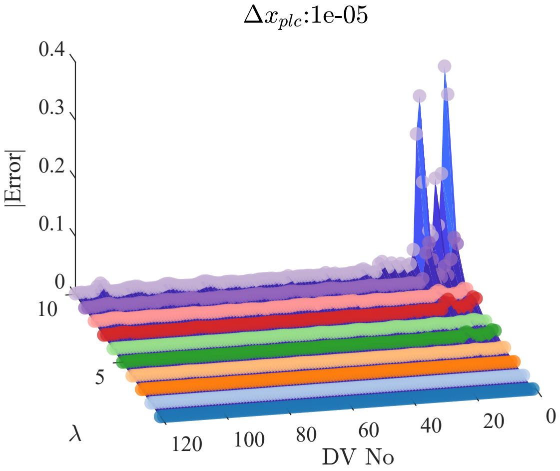

Figure C.30. Cantilever beam with non-rectangular stabilised 4-node shell element

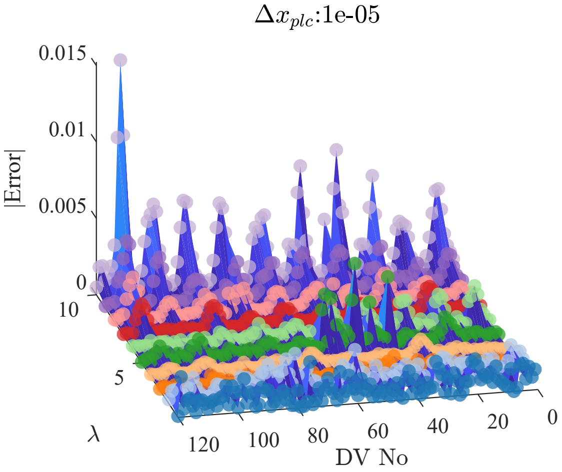

Figure C.31. Cantilever beam with non-rectangular EAS stabilised 8-node solid shell element

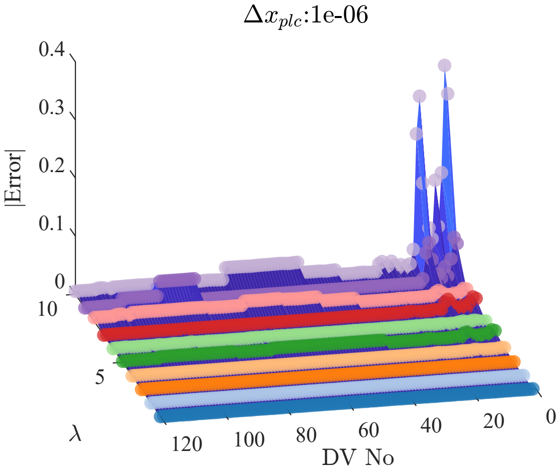

Figure C.32. Cantilever beam with non-rectangular stabilised 4-node shell element

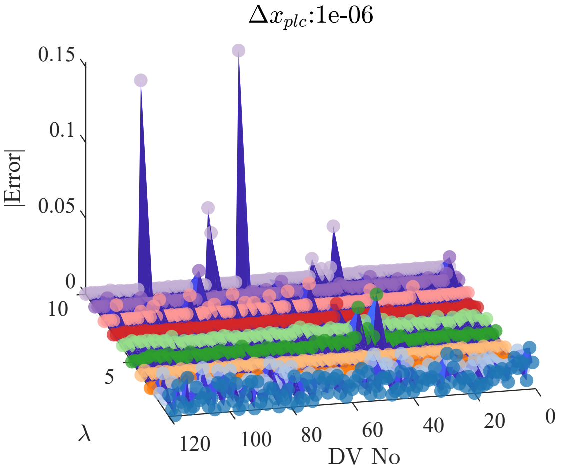

Figure C.33. Cantilever beam with non-rectangular EAS stabilised 8-node solid shell element

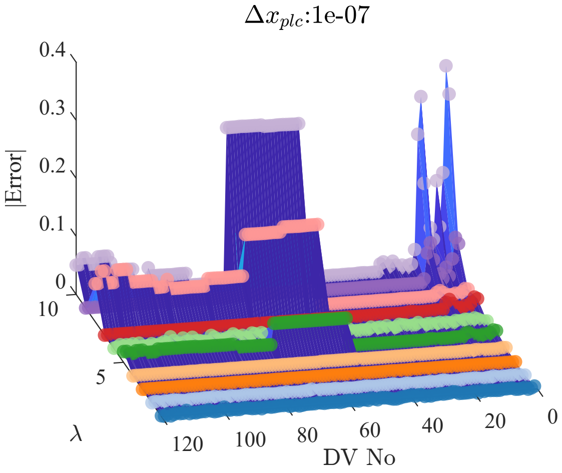

Figure C.34. Cantilever beam with non-rectangular stabilised 4-node shell element

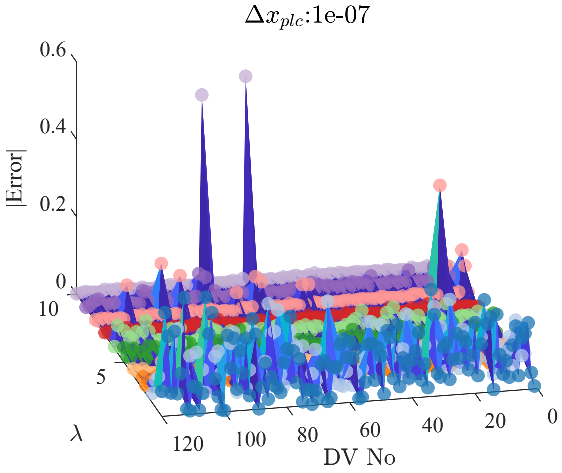

Figure C.35. Cantilever beam with non-rectangular EAS stabilised 8-node solid shell element

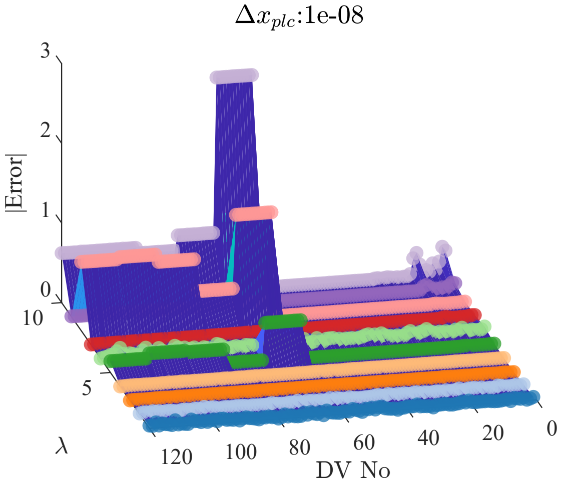

Figure C.36. Cantilever beam with non-rectangular stabilised 4-node shell element

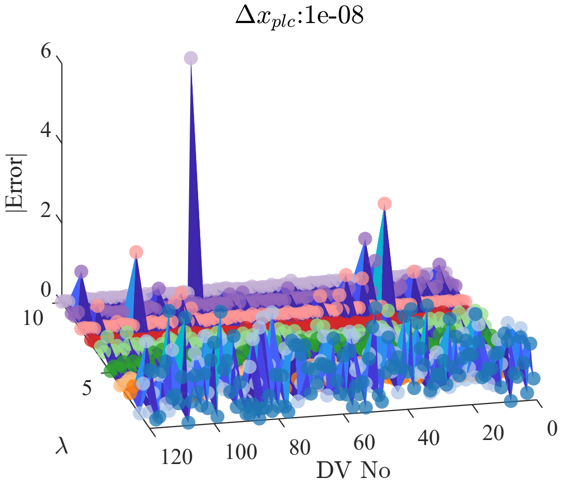

Figure C.37. Cantilever beam with non-rectangular EAS stabilised 8-node solid shell element

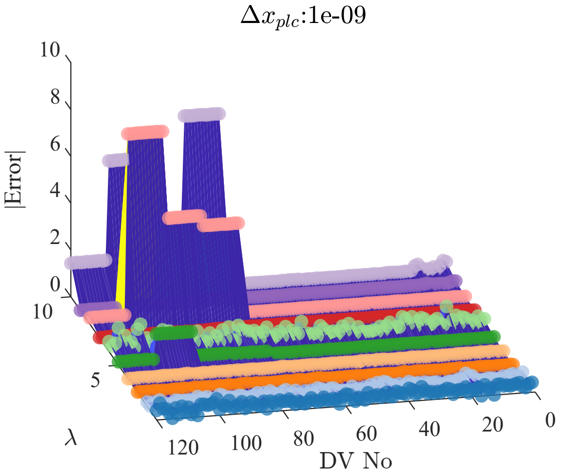

Figure C.38. Cantilever beam with non-rectangular stabilised 4-node shell element

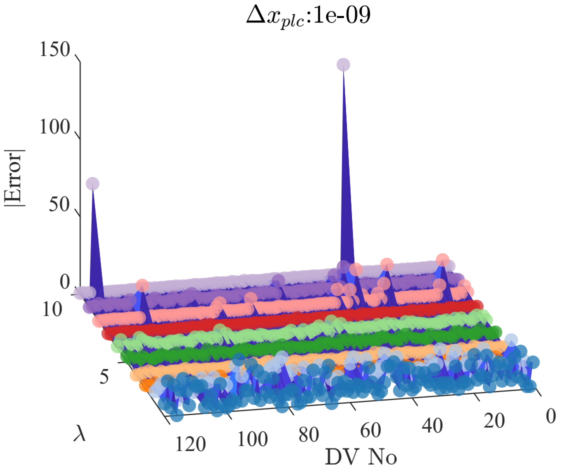

Figure C.39. Cantilever beam with non-rectangular EAS stabilised 8-node solid shell element

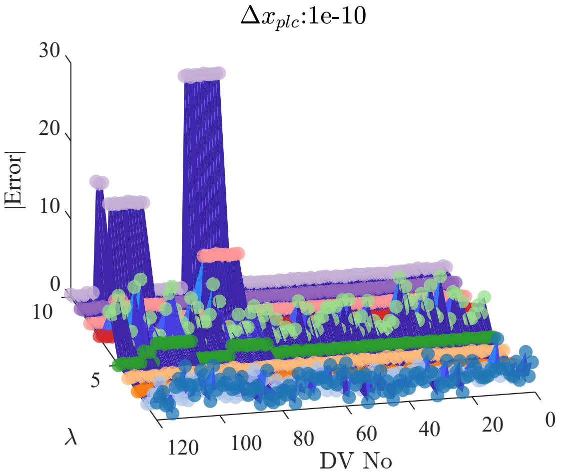

Figure C.40. Cantilever beam with non-rectangular stabilised 4-node shell element

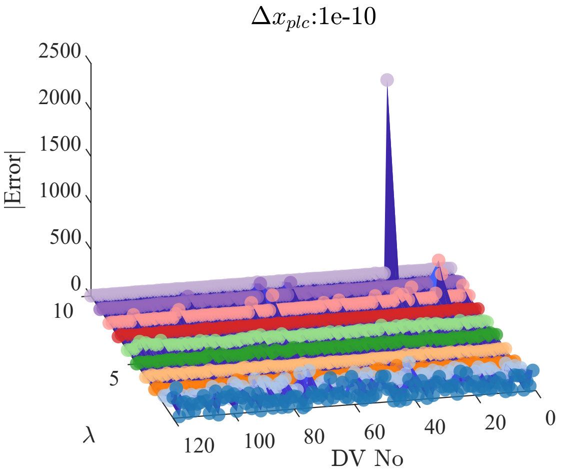

Figure C.41. Cantilever beam with non-rectangular EAS stabilised 8-node solid shell element

C.3 Non-rectangular element DSA decreased convergence subspace tolerance

The following numerical study investigates the influence of the convergence subspace tolerance on the results from section C.1 and C.2. The previous studies are performed using a convergence subspace tolerance on 10^{-8}, while it is set to 10^{-13} for this study.

From $10^{-1} \leq \Delta x_{plc} \leq 10^{-4}$, the results are nearly identical, but at lower perturbations, the absolute error is drastically reduced, and the previous clustering is eliminated. However, for the design variables corresponding to the patch with the fixed boundary, there is still a "plateau" where the error remains constant when the perturbation decreases.

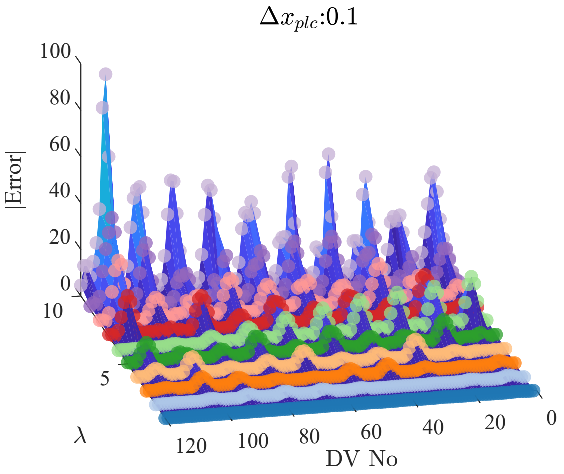

Figure C.42. Cantilever beam with non-rectangular stabilised 4-node shell element with decreased convergence tolerance

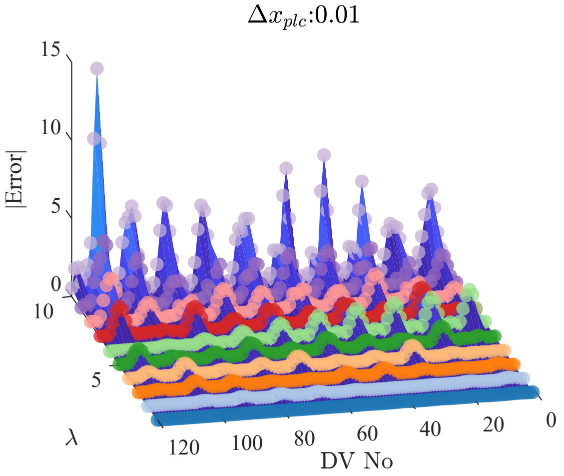

Figure C.43. Cantilever beam with non-rectangular stabilised 4-node shell element with decreased convergence tolerance

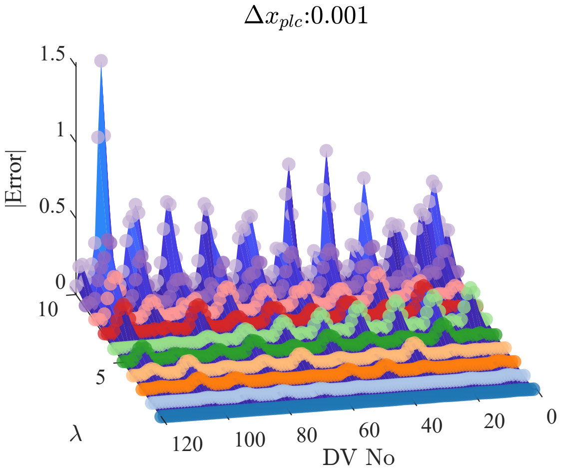

Figure C.44. Cantilever beam with non-rectangular stabilised 4-node shell element with decreased convergence tolerance

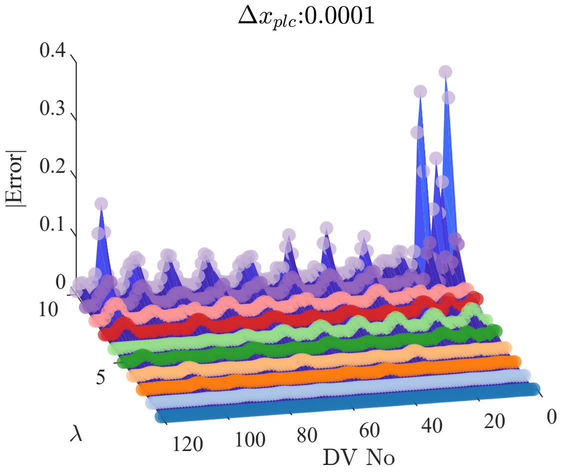

Figure C.45. Cantilever beam with non-rectangular stabilised 4-node shell element with decreased convergence tolerance

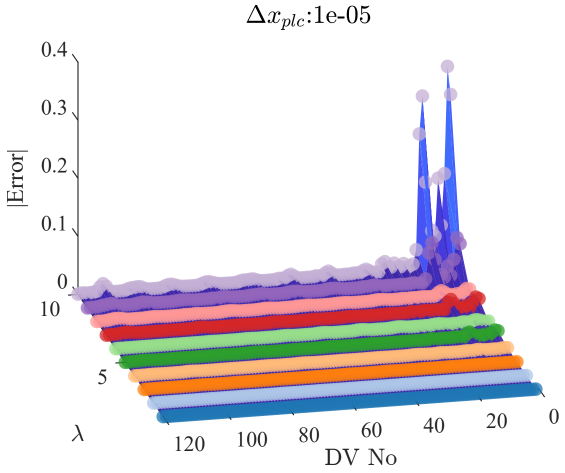

Figure C.46. Cantilever beam with non-rectangular stabilised 4-node shell element with decreased convergence tolerance

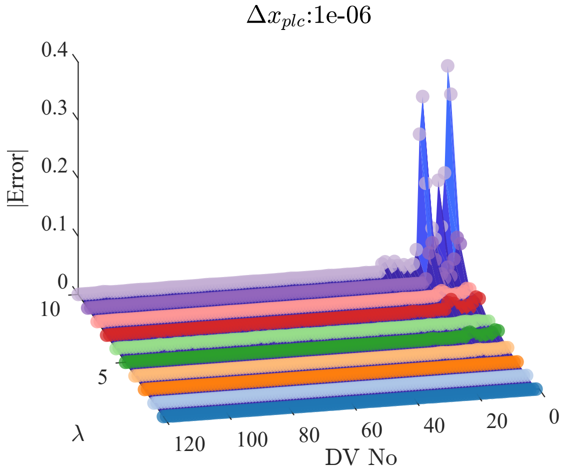

Figure C.47. Cantilever beam with non-rectangular stabilised 4-node shell element with decreased convergence tolerance

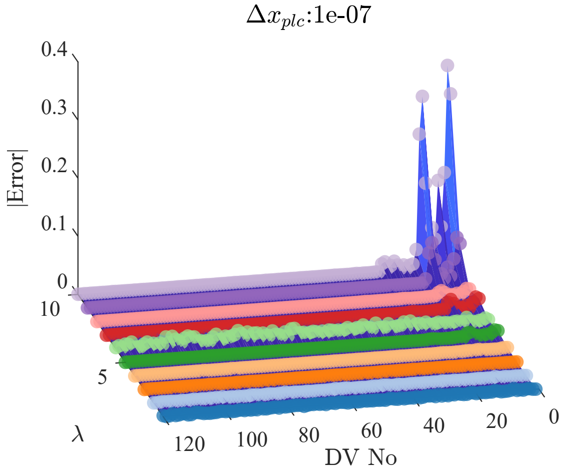

Figure C.48. Cantilever beam with non-rectangular stabilised 4-node shell element with decreased convergence tolerance

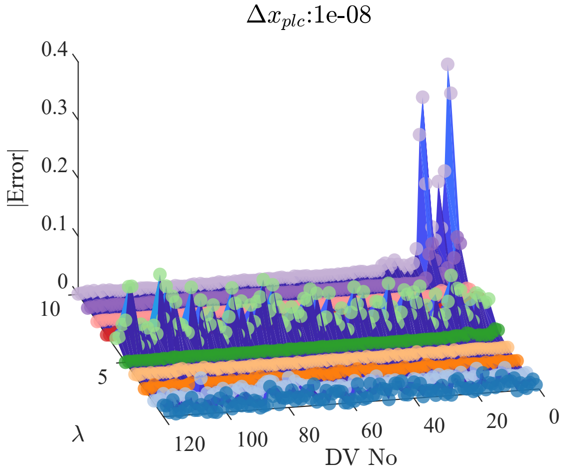

Figure C.49. Cantilever beam with non-rectangular stabilised 4-node shell element with decreased convergence tolerance

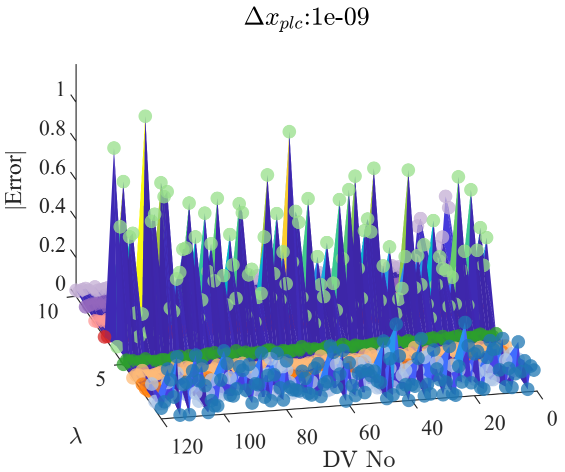

Figure C.50. Cantilever beam with non-rectangular stabilised 4-node shell element with decreased convergence tolerance

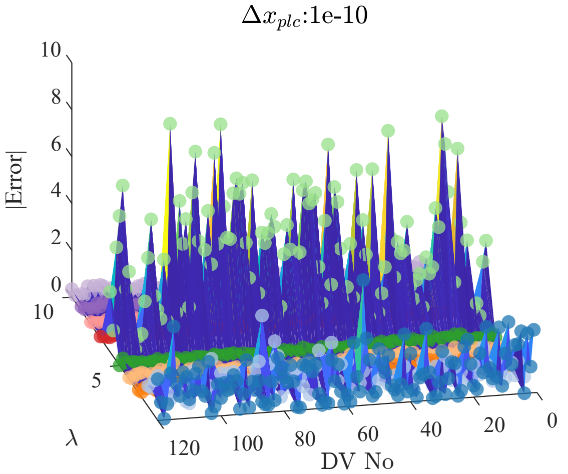

Figure C.51. Cantilever beam with non-rectangular stabilised 4-node shell element with decreased convergence tolerance

D Maximum Stress Criterion

The DSA of the maximum stress criterion contains some of the same main equations derived in section 5.2 for the maximum strain criterion. Thus, this chapter only highlights the main distinctions between the two criteria.

The candidate failure index is calculated by a transformation of the post-processed stress vector $\{\boldsymbol{\sigma}_{\mathbf{d}}\}_{elmc}$ which is calculated using the post-process strain vector and the constitutive properties in the element coordinate system as shown in Eq. (D.1).

$$\{\boldsymbol{\sigma}_{\mathbf{d}}\}_{elm} = [\mathbf{C}_{\mathbf{d}}]_{el}\,\{\boldsymbol{\varepsilon}_{\mathbf{d}}\}_{elm} = [\mathbf{T}_{\boldsymbol{\theta}}]_{elm}^{T}\,[\mathbf{C}_{\mathbf{12}}]_{elm}\,[\mathbf{T}_{\boldsymbol{\theta}}]_{elm}\,\{\boldsymbol{\varepsilon}_{\mathbf{d}}\}_{elm} \tag{D.1}$$

Here, the transformation of the stress vector to the material coordinate system is performed using Eq. (D.2).

$$[\mathbf{T}_{\boldsymbol{\theta}}]^{-T}\,\{\boldsymbol{\sigma}_{\mathbf{d}}\}_{elm} = \{\boldsymbol{\sigma}_{\mathbf{12}}\}_{elm} \tag{D.2}$$

The maximum stress criterion was derived for the stabilised 4-node shell element in Schøn (2023) using only a weight function on the failure index. This thesis extends the criterion to include an additional weight function on the stress field $w_\sigma(x_{plc})$, to obtain the same penalisation for RAMP as presented in Lund (2018). Therefore an effective stress vector $\{\boldsymbol{\sigma}_{\mathbf{12}}\}_{elm}^{(eff)}$ is introduced in Eq. (D.3).

$$w_\sigma(x_{plc})\{\boldsymbol{\sigma}_{\mathbf{12}}\}_{elm} = \{\boldsymbol{\sigma}_{\mathbf{12}}\}_{elm}^{(eff)} \tag{D.3}$$

This thesis uses RAMP without any penalisation for $w_\sigma(x_{plc})$, corresponding to the linear weighting shown in Figure 3.2. The failure index is calculated using the ultimate failure stress values and aggregated using the P-norm aggregate function.

The sensitivities are calculated using the adjoint method. Therefore, only $\left(\frac{\partial f_{pn}}{\partial\{\mathbf{D}\}}\right)^T$ and $\frac{\partial f_{pn}}{\partial x_{plc}}$ need to be calculated using slightly modified expressions.

$\left(\frac{\partial f_{pn}}{\partial\{\mathbf{D}\}}\right)^T$ is calculated using the chain rule in Eq. (D.4).

$$\begin{aligned}\left(\frac{\partial f_{pn}}{\partial\{\mathbf{D}\}}\right)^T =& \sum_{e=1}^{N_e}\sum_{l=1}^{N_{layer}}\sum_{m=1}^{2}[\mathbf{L}]_e\left([\mathbf{T}_{\mathbf{dG}}]_e\left(\frac{\partial f_{pn}}{\partial FI_{elm}^{(eff)}}\frac{\partial FI_{elm}^{(eff)}}{\partial FI_{elmc}}\frac{\partial FI_{elmc}}{\partial\{\boldsymbol{\sigma}_{\mathbf{12}}\}_{elmc}^{(eff)}}\frac{\partial\{\boldsymbol{\sigma}_{\mathbf{12}}\}_{elmc}^{(eff)}}{\partial\{\boldsymbol{\sigma}_{\mathbf{12}}\}_{elmc}}\right.\right.\\ &\left.\left.\frac{\partial\{\boldsymbol{\sigma}_{\mathbf{12}}\}_{elmc}}{\partial\{\boldsymbol{\sigma}_{\mathbf{d}}\}_{elmc}}\frac{\partial\{\boldsymbol{\sigma}_{\mathbf{d}}\}_{elmc}}{\partial\{\boldsymbol{\varepsilon}_{\mathbf{d}}\}_{elmc}}\frac{\partial\{\boldsymbol{\varepsilon}_{\mathbf{d}}\}_{elmc}}{\partial\{\mathbf{d}\}_e}\right)^T\right)\end{aligned} \tag{D.4}$$

The approach is analogous to the maximum strain criterion carried out under the assumption of a fixed failure mode. Consequently, the calculation of $\frac{\partial FI_{elmc}}{\partial\{\boldsymbol{\sigma_{12}}\}^{(eff)}_{elmc}}$ is performed using Eq. (D.5).

$$\frac{\partial FI_{elmc}}{\partial\{\boldsymbol{\sigma_{12}}\}^{(eff)}_{elmc}} = \left\lfloor \frac{1}{X_x}, \frac{1}{Y_x}, 0, \frac{1}{S_{12}}, \frac{1}{S_{13}}, \frac{1}{S_{23}} \right\rfloor \tag{D.5}$$

$\frac{\partial\{\boldsymbol{\sigma_{12}}\}^{(eff)}_{elmc}}{\partial\{\boldsymbol{\sigma_{12}}\}_{elmc}}$ is calculated by differentiation of Eq. (D.3) as shown in Eq. (D.6).

$$\frac{\partial\{\boldsymbol{\sigma_{12}}\}^{(eff)}_{elmc}}{\partial\{\boldsymbol{\sigma_{12}}\}_{elmc}} = w_{\sigma}(x_{plc}) \tag{D.6}$$

The partial derivative of Eq. (D.2) w.r.t $\{\boldsymbol{\sigma_d}\}_{elmc}$ is calculated using Eq. (D.7).

$$\frac{\partial\{\boldsymbol{\sigma_{12}}\}_{elmc}}{\partial\{\boldsymbol{\sigma_d}\}_{elmc}} = [\mathbf{T}_{\boldsymbol{\theta}}]^{-T}_{elmc} \tag{D.7}$$

Differentiation of Eq. (D.1) yields Eq. (D.8)

$$\frac{\partial\{\boldsymbol{\sigma_d}\}_{elmc}}{\partial\{\boldsymbol{\varepsilon_d}\}_{elmc}} = [\mathbf{T}_{\boldsymbol{\theta}}]^{T}_{elmc}\,[\mathbf{C_{12}}]_{elmc}\,[\mathbf{T}_{\boldsymbol{\theta}}]_{elmc} \tag{D.8}$$

These expressions solve the adjoint problem to obtain $\{\boldsymbol{\Lambda}\}$.

Since there are two interpolation functions, $\frac{\partial f_{pn}}{\partial x_{plc}}$ becomes slightly more complicated. $FI^{(eff)}_{elm}$ is a function of $w_{FI}(x_{plc})$ and $w_{\sigma}(x_{plc})$, thus the chain rule yields Eq. (D.10).

$$\frac{\partial f_{pn}}{\partial x_{plc}} = \sum_{e=1}^{N_e}\sum_{l=1}^{N_{layer}}\sum_{m=1}^{2} \frac{\partial f_{pn}}{\partial FI^{(eff)}_{elm}} \left(\frac{\partial FI^{(eff)}_{elm}}{\partial w_{FI}(x_{plc})} \frac{\partial w_{FI}(x_{plc})}{\partial x_{plc}} + \frac{\partial FI^{(eff)}_{elm}}{\partial FI_{elmc}} \right. \tag{D.9}$$

$$\left. \frac{\partial FI_{elmc}}{\partial\{\boldsymbol{\sigma_{12}}\}^{(eff)}_{elmc}} \frac{\partial\{\boldsymbol{\sigma_{12}}\}^{(eff)}_{elmc}}{\partial w_{\sigma}(x_{plc})} \frac{\partial w_{\sigma}(x_{plc})}{\partial x_{plc}} \right) \tag{D.10}$$

The only new term in Eq. (D.10) is $\frac{\partial\{\boldsymbol{\sigma_{12}}\}^{(eff)}_{elmc}}{\partial w_{\sigma}(x_{plc})}$, which is calculated by differentiation of Eq. (D.3) as shown in Eq. (D.11)

$$\frac{\partial\{\boldsymbol{\sigma_{12}}\}^{(eff)}_{elmc}}{\partial w_{\sigma}(x_{plc})} = \{\boldsymbol{\sigma_{12}}\}_{elmc} \tag{D.11}$$

The analytical sensitivities are validated using the single curved shell model and compared against finite difference approximations at various perturbation sizes, as shown in Figure D.1.

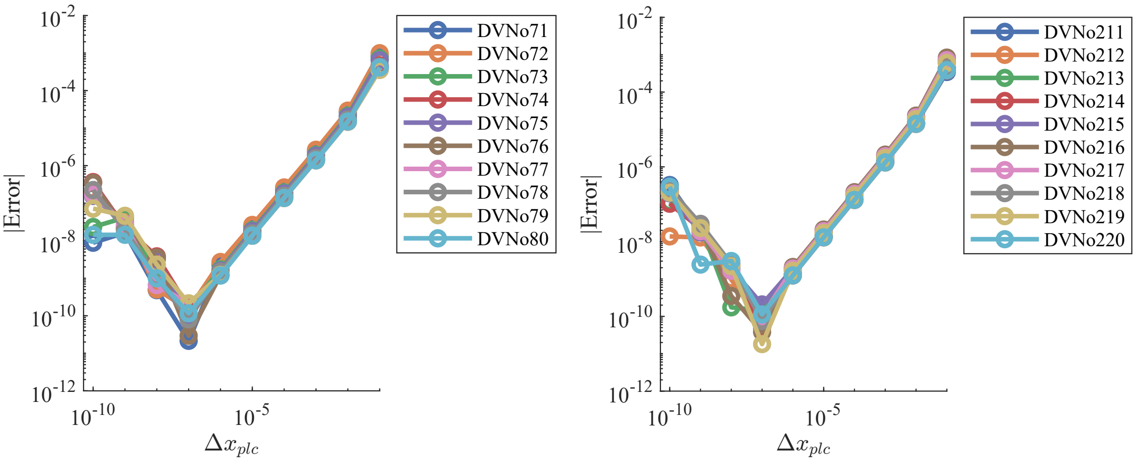

Figure D.1. Absolute error between the finite difference approximation and the analytical sensitivities in the single-curved shell benchmark example.

E Tsai-Wu Failure Criterion

The DSA of the Tsai-Wu failure criterion contains some of the same main equations derived in section 5.2 and D. Thus, this chapter only highlights the main distinctions between these criteria.

The Tsai-Wu failure criterion and the von Mises failure criterion are both quadratic criteria. Unlike the von Mises failure criterion, the Tsai-Wu failure criterion considers the coupled nature of distortion and dilatation. This makes it particularly suitable for predicting the failure of orthotropic materials.(Jones, 1998) The failure criterion is reformulated by (Groenwold and Haftka, 2006) to be proportional to the load for practical usage. A second-order polynomial equation in Eq. (E.1) is obtained from the reformulation of the Tsai Wu failure criterion.

$$\gamma^2(F_{11}\sigma_1^2 + F_{22}\sigma_2^2 + 2F_{12}\sigma_1\sigma_2 + F_{66}\sigma_6^2) + \gamma(F_1\sigma_1 + F_2\sigma_2) - 1 = 0 \tag{E.1}$$

Here the same notation as presented in Jones (1998) is used for representation of the stress vector $\{\boldsymbol{\sigma_{12}}\} = \lfloor \sigma_1, \sigma_2, 0, \sigma_{66}, 0, 0 \rfloor^T$. Similar to the maximum stress criterion in Appendix D a $w_\sigma(x_{plc})$ is utilised to penalise the stress field. The stress vector used to calculate Eq. (E.1) is therefore $\{\boldsymbol{\sigma_{12}}\}^{(eff)} = w_\sigma(x_{plc}) \lfloor \sigma_1, \sigma_2, 0, \sigma_{66}, 0, 0 \rfloor^T$. Further, the Tsai-Wu strength values are calculated using the ultimate failure stress in the principal material directions and the following equations:

$$\begin{aligned} F_1 =& \frac{1}{X_t} - \frac{1}{X_c}, \qquad F_2 = \frac{1}{Y_t} - \frac{1}{Y_c}, \qquad F_{11} = \frac{1}{X_t X_c} \\ F_{22} =& \frac{1}{Y_t Y_c}, \qquad F_{12} \approx -\frac{1}{2}\sqrt{F_{11}F_{22}}, \qquad F_{66} = \frac{1}{S^2} \end{aligned}$$

An analytic solution to a second-order polynomial equation can be obtained using Eqs. (E.2), (E.3), (E.4) and (E.5).

$$\gamma = \frac{-b \pm \sqrt{d}}{2a} \tag{E.2}$$

$$a = F_{11}\sigma_1^2 + F_{22}\sigma_2^2 + 2F_{12}\sigma_1\sigma_2 + F_{66}\sigma_6^2 \tag{E.3}$$

$$b = F_1\sigma_1 + F_2\sigma_2 \tag{E.4}$$

$$d = b^2 + 4a \tag{E.5}$$

The smallest positive root serves as a safety factor against failure, and the failure index is calculated as the reciprocal of this safety factor, as demonstrated in Eq. (E.6).

$$FI = \frac{1}{\gamma} \tag{E.6}$$

The failure index in Eq. (E.6) is interpolated using $w_{Fi}(x_{plc})$ and aggregated using the same methods presented in chapter 5.

E.1 Sensitivity Analysis

$\left(\frac{\partial f_{pn}}{\partial\{\mathbf{D}\}}\right)^T$ for the Tsai-Wu failure criterion is calculated using the chain rule as shown in Eq. (E.7).

$$\left(\frac{\partial f_{pn}}{\partial\{\mathbf{D}\}}\right)^T = \sum_{e=1}^{N_e}\sum_{l=1}^{N_{layer}}\sum_{m=1}^{2}[\mathbf{L}]_e\left([\mathbf{T_{dG}}]_e\left(\frac{\partial f_{pn}}{\partial FI_{elm}^{(eff)}}\frac{\partial FI_{elm}^{(eff)}}{\partial FI_{elmc}}\frac{\partial FI_{elmc}}{\partial\{\boldsymbol{\sigma}_{\mathbf{12}}\}_{elmc}^{(eff)}}\frac{\partial\{\boldsymbol{\sigma}_{\mathbf{12}}\}_{elmc}^{(eff)}}{\partial\{\boldsymbol{\sigma}_{\mathbf{12}}\}_{elmc}}\frac{\partial\{\boldsymbol{\sigma}_{\mathbf{12}}\}_{elmc}}{\partial\{\boldsymbol{\sigma}_{\mathbf{d}}\}_{elmc}}\frac{\partial\{\boldsymbol{\sigma}_{\mathbf{d}}\}_{elmc}}{\partial\{\boldsymbol{\varepsilon}_{\mathbf{d}}\}_{elmc}}\frac{\partial\{\boldsymbol{\varepsilon}_{\mathbf{d}}\}_{elmc}}{\partial\{\mathbf{d}\}_e}\right)^T\right) \tag{E.7}$$

Eqs. (5.18), (5.19), (D.7), (D.8), (5.23) and(5.24) are utilised to compute $\frac{\partial f_{pn}}{\partial FI_{elm}^{(eff)}}$, $\frac{\partial FI_{elm}^{(eff)}}{\partial FI_{elmc}}$ $\frac{\partial\{\boldsymbol{\sigma}_{\mathbf{12}}\}_{elmc}}{\partial\{\boldsymbol{\sigma}_{\mathbf{d}}\}_{elmc}}$, $\frac{\partial\{\boldsymbol{\sigma}_{\mathbf{d}}\}_{elmc}}{\partial\{\boldsymbol{\varepsilon}_{\mathbf{d}}\}_{elmc}}$ and $\frac{\partial\{\boldsymbol{\varepsilon}_{\mathbf{d}}\}_{elmc}}{\partial\{\mathbf{d}\}_e}$. The distinction between Eq. (E.7) and the equation for the maximum stress criterion in Eq. (D.4) lies in the terms related to the failure indices, which is calculated using the chain rule in Eq. (E.8).

$$\frac{\partial FI_{elmc}}{\partial\{\boldsymbol{\sigma}_{\mathbf{12}}\}_{elmc}^{(eff)}} = \frac{\partial FI_{elmc}}{\partial\gamma_{elmc}}\left(\frac{\partial\gamma_{elmc}}{\partial a_{elmc}}\frac{\partial a_{elmc}}{\partial\{\boldsymbol{\sigma}_{\mathbf{12}}\}_{elmc}^{(eff)}} + \frac{\partial\gamma_{elmc}}{\partial b_{elmc}}\frac{\partial b_{elmc}}{\partial\{\boldsymbol{\sigma}_{\mathbf{12}}\}_{elmc}^{(eff)}} + \frac{\partial\gamma_{elmc}}{\partial d_{elmc}}\left(\frac{\partial d_{elmc}}{\partial a_{elmc}}\frac{\partial a_{elmc}}{\partial\{\boldsymbol{\sigma}_{\mathbf{12}}\}_{elmc}^{(eff)}} + \frac{\partial d_{elmc}}{\partial b_{elmc}}\frac{\partial b_{elmc}}{\partial\{\boldsymbol{\sigma}_{\mathbf{12}}\}_{elmc}^{(eff)}}\right)\right) \tag{E.8}$$

In Eq. (E.8), the partial derivatives w.r.t the safety factor against failure are implemented using Eqs. (E.9) and (E.10).

$$\frac{\partial\gamma_{elmc}}{\partial d_{elmc}} = \pm\frac{1}{4a_{elmc}\sqrt{d_{elmc}}} \tag{E.9}$$

$$\frac{\partial\gamma_{elmc}}{\partial a_{elmc}} = \frac{b_{elmc}\pm\sqrt{d_{elmc}}}{2a_{elmc}^2} \tag{E.10}$$

The symbol ± in this context should correspond to the sign in Eq. (E.2) that yields the smallest positive root. (Gadegaard and Thuesen, 2022; Schøn, 2023; Troelsgaard et al., 2023)

$$\frac{\partial FI_{elmc}}{\partial \gamma_{elmc}} = = -\gamma_{elmc}^{-2} \tag{E.11}$$

$$\frac{\partial \gamma_{elmc}}{\partial b_{elmc}} = \frac{-1}{2a_{elmc}} \tag{E.12}$$

$$\frac{\partial d_{elmc}}{\partial b_{elmc}} = 2b_{elmc} \tag{E.13}$$

$$\frac{\partial d_{elmc}}{\partial a_{elmc}} = 4 \tag{E.14}$$

$$\frac{\partial b_{elmc}}{\partial \{\boldsymbol{\sigma_{12}}\}^{(eff)}} = \Big\lfloor F_{1,elmc},\ F_{2,elmc},\ 0,\ 0,\ 0,\ 0 \Big\rfloor \tag{E.15}$$

$$\frac{\partial a_{elmc}}{\partial \{\boldsymbol{\sigma_{12}}\}^{(eff)}_{elmc}} = \Big\lfloor 2F_{11,elmc}\sigma_{1,elmc} + 2F_{12,elmc}\sigma_{2,elmc},\ 2F_{22,elmc}\sigma_{2,elmc} + 2F_{12,elmc}\sigma_{1,elmc},\ 0,\ 2F_{66,elmc}\sigma_{6,elmc},\ 0,\ 0 \Big\rfloor \tag{E.16}$$

Eq. (D.10) is used to calculate $\frac{\partial f_{pn}}{\partial x_{plc}}$, where the failure index calculated from Tsai-Wu failure criterion is used. The analytical sensitivities are validated using the single curved shell model and compared against finite difference approximations at various perturbation sizes, as shown in Figure E.1.

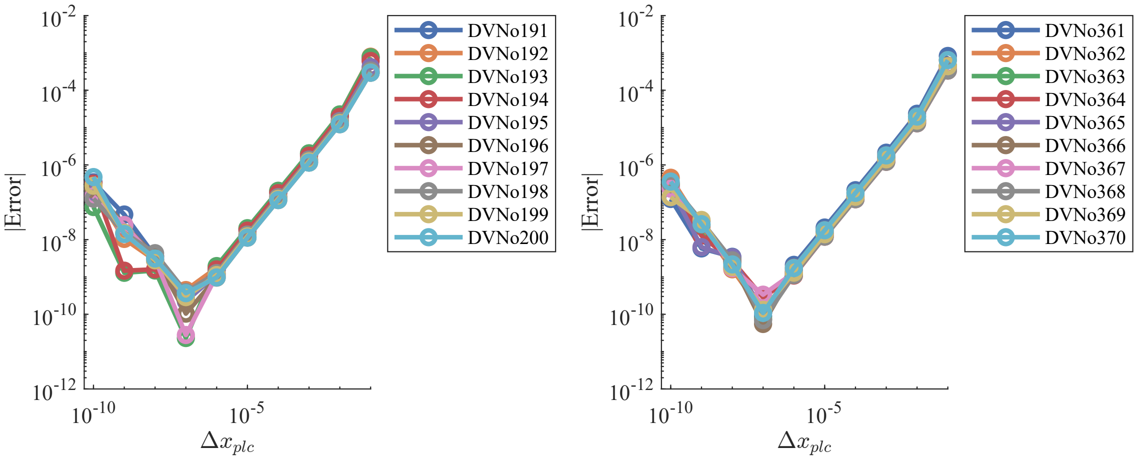

Figure E.1. Absolute error between the finite difference approximation and the analytical sensitivities in the single-curved shell benchmark example.